Lappeenranta
University of Technology

Feng Qiu

SURFACE TRANSFORMATION HARDENING OF CARBON STEEL WITH HIGH POWER FIBER LASER

Thesis for the degree of Doctor of Science (Technology) to be presented with due permission for public examination and criticism in Auditorium 1382 at Lappeenranta University of Technology, Lappeenranta, Finland on the 9th of January, 2013, at noon.

Acta Universitatis

Lappeenrantaensis 507

Supervisor	Docent Veli Kujanpää Lappeenranta University of Technology (Prof. of VTT Technical Research Centre) Finland
Reviewers	Prof. Jens Klaestrup Kristensen Department of Mechanical Engineering Technical University of Denmark Denmark
	Dr. Henrikki Pantsar Cencorp Oyj Finland
Opponent	Prof. Jens Klaestrup Kristensen Department of Mechanical Engineering Technical University of Denmark Denmark

ISBN 978-952-265-360-4
ISBN 978-952-265-361-1 (PDF)
ISSN 1456-4491
Lappeenrannan teknillinen yliopisto
Yliopistopaino 2012

ABSTRACT

Feng Qiu

Surface transformation hardening of carbon steel with high power fiber laser

Lappeenranta 2012

105 pages
Acta Universitatis Lappeenrantaensis 507
Diss. Lappeenranta University of Technology
ISBN 978-952-265-360-4, ISBN 978-952-265-361-1 (PDF), ISSN 1456-4491

This study investigated the surface hardening of steels via experimental tests using a multi-kilowatt fiber laser as the laser source. The influence of laser power and laser power density on the hardening effect was investigated. The microhardness analysis of various laser hardened steels was done. A thermodynamic model was developed to evaluate the thermal process of the surface treatment of a wide thin steel plate with a Gaussian laser beam. The effect of laser linear oscillation hardening (LLOS) of steel was examined.

An as-rolled ferritic-pearlitic steel and a tempered martensitic steel with 0.37 wt% C content were hardened under various laser power levels and laser power densities. The optimum power density that produced the maximum hardness was found to be dependent on the laser power. The effect of laser power density on the produced hardness was revealed. The surface hardness, hardened depth and required laser power density were compared between the samples. Fiber laser was briefly compared with high power diode laser in hardening medium-carbon steel.

Microhardness (HV0.01) test was done on seven different laser hardened steels, including rolled steel, quenched and tempered steel, soft annealed alloyed steel and conventionally through-hardened steel consisting of different carbon and alloy contents. The surface hardness and hardened depth were compared among the samples. The effect of grain size on surface hardness of ferritic-pearlitic steel and pearlitic-cementite steel was evaluated. In-grain indentation was done to measure the hardness of pearlitic and cementite structures. The macrohardness of the base material was found to be related to the microhardness of the softer phase structure. The measured microhardness values were compared with the conventional macrohardness (HV5) results.

A thermodynamic model was developed to calculate the temperature cycle, A_{c1} and A_{c3} boundaries, homogenization time and cooling rate. The equations were numerically solved with an error of less than 10^{-8}. The temperature distributions for various thicknesses were compared under different laser traverse speed. The lag of the

peak temperature behind the laser beam was found to have an upper limit. The model was verified by experiments done on six different steels. The calculated thermal cycle and hardened depth were compared with measured data. Correction coefficients were applied to the model for AISI 4340 steel.

AISI 4340 steel was hardened by laser linear oscillation hardening (LLOS). Equations were derived to calculate the overlapped width of adjacent tracks and the number of overlapped scans in the center of the scanned track. The effect of oscillation frequency on the hardened depth was investigated by microscopic evaluation and hardness measurement. The homogeneity of hardness and hardened depth with different processing parameters were investigated. The hardness profiles were compared with the results obtained with conventional single-track hardening. LLOS was proved to be well suitable for surface hardening in a relatively large rectangular area with considerable depth of hardening. Compared with conventional single-track scanning, LLOS produced notably smaller hardened depths while at 40 and 100 Hz LLOS resulted in higher hardness within a depth of about 0.6 mm.

Keywords: hardening, steel, fiber laser, laser power, power density, microhardness, in-grain indentation, thermodynamic model, temperature cycle, oscillation scanning

UDC 621.373.8:669.1:536.7

ACKNOWLEDGEMENTS

As this thesis is completed, my doctoral study finally approaches its end. At this moment, many faces are crossing my mind together with segments of memories of my life these years. I have benefited much from the support of many people. Without their help, this thesis would not have been completed.

Firstly, I am very grateful to my supervisor Professor Veli Kujanpää who has been guiding me throughout my whole doctoral study. I have benefited a lot from his instructions, from the basic concepts to creative ideas. He also helped me in many other aspects of my lab work.

I would like to express my gratitude to the pre-examiners of this dissertation, Professor Jens Kristensen of Technical University of Denmark and Dr. Henrikki Pantsar of Cencorp Oyj. Their comments are very valuable for improving the quality of this thesis.

I appreciate the help of my colleagues at the Laboratory of Laser Processing. I am thankful to Mr. Ilkka Poutiainen and Mr. Pertti Kokko who helped me with the experimental tests. I am thankful to Mr. Esa Lappalainen who spent much time writing a very detailed manual that helped me a lot in operating the Struers Durascan Hardness Tester. I am also thankful to Mr. Antti Heikkinen of who helped prepare the samples for hardness measurement and microscopic observation.

I am grateful to Mrs. Päivi Hovila of LUT Chemistry who instructed me to use the scanning electron microscope (SEM). I would thank Mr. Ari Anonen of Ovako Oy who kindly provided the tested materials of this study.

Besides, I am thankful to my adorable friends here in Finland. Though with different cultural and religious backgrounds, we have shared many interesting ideas on life, faith and culture. I am not religious, yet I do believe that life is a process of spiritual growth by learning from one’s experience. They have been an important part of my life these years and I feel very lucky to get to know and learn from them.

At last, I would express my most special appreciation and love to my dear parents, who always believe in and encourage me. They are not only my family but also my mentors in my life. I can always gain strength from their perseverance and optimism. It may not be possible to find proper words to express my affection for them, but it is never essential as they feel what I feel. This thesis is not merely finished for myself but also dedicated for them.

Feng Qiu

Lappeenranta, November 2012

TABLE OF CONTENTS

LIST OF PUBLICATIONS

This dissertation includes four research publications as follows.

1. Feng Qiu and Veli Kujanpää. 2011. Transformation hardening of medium-carbon steel with a fiber laser: the influence of laser power and laser power density. Mechanika, Vol. 17, No. 3, pp.318-323. DOI: 10.5755/j01.mech.17.3.510.

2. Feng Qiu, Juha Uusitalo and Veli Kujanpää. 2012. Laser transformation hardening of carbon steel: microhardness analysis on microstructural phases. Surface Engineering, InPress. DOI: 10.1179/1743294412Y.0000000049.

3. Feng Qiu and Veli Kujanpää. 2012. Thermodynamic modelling of the surface treatment of a wide thin steel plate with a Gaussian laser beam. International Journal of Computational Materials Science and Surface Engineering, InPress.

4. Feng Qiu and Veli Kujanpää. 2012. Surface hardening of AISI 4340 steel by laser linear oscillation scanning. Surface Engineering, Vol. 28, No. 8, pp.569-575. DOI: 10.1179/1743294412Y.0000000034.

CONTRIBUTION OF THE CANDIDATE IN THE PUBLICATIONS

The candidate was the main author of all the publications that comprise the second part of this thesis. The candidate conceived all the ideas and conclusions that were presented in the publications. Professor Veli Kujanpää, the main co-author and supervisor of the candidate, helped to guide the ideas into more comprehensible forms and revised the papers prior to submission to the conferences and journals for publications. The tasks undertaken by the candidate in preparing the papers are summarized for each publication as follows:

Publication 1
Literature study: Studied the relevant literature for the paper.
Experimental investigation: Designed the processing parameters, carried out the tests and analyzed the experimental results.
Writing the paper: responsible for writing the whole paper.

Publication 2
Literature study: Studied the relevant literature for the paper.
Experimental investigation: Designed the processing parameters, carried out the tests and analyzed the experimental results.
Writing the paper: responsible for writing the whole paper.

Publication 3
Literature study: Studied the relevant literature for the paper.
Theoretical Modelling: Established the equations of the model.
Experimental investigation: Designed the processing parameters, carried out the tests and analyzed the experimental results.
Writing the paper: responsible for writing the whole paper.

Publication 4
Literature study: Studied the relevant literature for the paper.
Theoretical Modelling: Established the equations of the model.
Experimental investigation: Designed the processing parameters, carried out the tests and analyzed the experimental results.
Writing the paper: responsible for writing the whole paper.

LIST OF ABBREVIATIONS AND SYMBOLS

Abbreviation	Explanation
AISI	American Iron and Steel Institute
ASTM	American Society for Testing and Materials
BCC	Body-centered cubic
BCT	Body-centered tetragonal
BPP	Beam parameter product
CW	Continuous wave
EDS	Energy Dispersive Spectroscopy
FCC	Face-centered cubic
HAZ	Heat affected zone
HV	Vickers hardness
ISO	International Organization for Standardization
LLOS	Laser linear oscillation scanning
LCVD	Laser chemical vapor deposition
MHT	Micro-hardness Tester
Nd:YAG	Neodymium: yttrium-aluminium-garnet
Nital	Nitric acid solution in alcohol
QCW	Quasi continuous wave
SEM	Scanning Electron Microscope
VHT	Vickers Hardness Tester

Symbol	Unit	Explanation
α	m^2/s	Thermal diffusivity
β		Absorptivity of laser energy by the material's surface
ε		A dimensionless variable
η		A coefficient of correction
ρ	kg/m^3	Mass density
μ	Hz	Oscillation frequency of LLOS
c		A constant determined by the absorbed laser power and the physical properties of the material
d	cm	Width of the workpiece
d_0	mm	Diameter of a oscillating laser spot in LLOS
d_g	μm	Grain diameter
d_s	mm	Laser spot diameter; Laser spot size
e_r		Relative error
j_u		A coefficient of correction
j_c		A coefficient of correction
j_T		A coefficient of correction
k	W/(m·K)	Thermal conductivity

l	cm	Length of the workpiece
r_b	mm	Radius of the laser beam
t_h	s	Homogenization time
u		Dimensionless temperature increase
v_x	mm/s	Moving speed of the laser head
v_y	mm/s	Oscillation speed of LLOS
w		Dimensionless cooling rate
A	mm	Oscillation amplitude of LLOS
A_{c1}	°C	Austenite start temperature
A_{c3}	°C	Austenite finish temperature of hypoeutectoid steel
A_{cm}	°C	Austenite finish temperature hypereutectoid steel
C_p	J/(kg·K)	Specific heat capacity
H		Dimensionless thickness of the workpiece
I_p	W/cm^2	Laser power density
K		A constant used in Petch-Hall equation
M_s	°C	Martensite start temperature
M_f	°C	Martensite finish temperature
N_c		The number of overlapped scanning tracks in the center of oscillation
P	W	Output laser power; Incident laser power
P_0	W	Absorbed laser power
R_a	μm	Surface roughness of the sample
R_c	K/s	Cooling rate
R_e	MPa	Yield point
R_i	MPa	Stress required to make the dislocations move in the grains
S_{cov}	mm	The overlapped width at the center of oscillation in LLOS
S_{e0}	mm	The distance between adjacent tracks at the edge of oscillation
S_{eov}	mm	The overlapped width at the edge of oscillation in LLOS
T	°C	Temperature of the workpiece
T_0	°C	Initial temperature of the workpiece
T_i	K	Temperature increase above the initial temperature
T_{imax}	K	The peak value of the temperature increase
T_m	°C	Melting point of the material
U	W/m^3	Heat generated per unit volume
V		Dimensionless traverse speed
X		Dimensionless x coordinate
Y		Dimensionless y coordinate
Z		Dimensionless z coordinate
Z_{AC}		Calculated dimensionless A_{c1} or A_{c3} depth

PART I: OVERVIEW OF THE DISSERTATION

1 INTRODUCTION

1.1 Background of the Study

Surface transformation hardening using laser energy as the heat source was one of the earliest applications of laser material processing. The first laser heat treatment of metals was reported in early 1960s.[1] In the following a few years, investigations were done on laser induced surface hardening of steel and its alloys.[2,3] In 1973, Saginaw Steering Division of General Motors used a CO_2 laser to harden the steering gear housing on a production basis. This is regarded as the first industrial application of laser hardening.[4] Compared with traditional hardening processes, laser surface hardening features some important benefits such as low distortion of the workpiece, high processing speed and self-quenching without the need of external quenchants.

Although the potential of this process was noticed early by the automobile industry, its industrial acceptance has been rather limited compared with other laser processes such as cutting, welding and marking. This situation was caused by a variety of facts. Manufacturers lacked the knowledge and experience about the laser hardening process. CO_2 laser used to be the only choice that was capable to produce sufficient power density for hardening.[6] In order to achieve efficient absorption of the far infrared radiation, a coating has been normally used on the workpiece, making this process uneconomical in many applications. Moreover, various conventional surface treatment processes were commercially available and familiar to the designers and manufacturers. The majority of industrial production procedures were therefore designed for these processes rather than laser processing. These all restrained the applicability of laser hardening process.[6,7]

Three different types of laser sources including CO_2, Nd:YAG and high power diode lasers used to be the alternatives used for laser surface treatment. Until the end of last century, CO_2 laser was almost the only laser type that was capable to provide the combination of power density and interaction time required for laser hardening. Since late 1990s, the development of multi-kilowatt Nd:YAG lasers with both flash lamp and diode pumping provide an alternative source with several advantages. One of the main benefits of Nd:YAG laser is that the wavelength of the laser light (typically 1.06 μm) allows the beam to be delivered via an optical fiber with relatively low energy loss. This enables flexible delivery of the laser beam at the processing head. Consequently, Nd:YAG lasers providing high levels of laser power can be manipulated with robot, making them ideal for three-dimensional processing. More recently, multi-kilowatt diode lasers were developed with the wavelength of approximately 8 μm, which are compact and can be mounted directly on a robot for hardening of components with complex geometries. Compared with the wavelength of a CO_2 laser (around 10.6 μm), the beam wavelengths of Nd:YAG and diode lasers increase the absorptivity on metal surface significantly and thus absorptive coatings are no longer needed, simplifying the operation and reducing the cost of production.[5]

High power Nd:YAG and diode lasers have been applied in various treatments of steel and its alloys.[6,7,8] Besides, various types of special shaping optics were developed as an advanced solution to produce desirable shapes and sizes of laser irradiated area with relatively homogeneous energy distribution.[9,10]

During the last decade or so, high power fiber lasers have been developed in a dramatic manner. From lab set-ups delivering milliwatt-scale output power in the early 1990s, fiber lasers have evolved to multi-kilowatt devices for use in industrial material processing. Two technical developments promoted the progress of fiber laser: the optical communication industry provided the preparation technologies for highly transmissive single-mode fibers and the optoelectronics industry made available the high-power laser diodes required for the pumping of fibers. The increased power level of fiber laser is to a large extent based on the availability of reliable and long-life diode pump systems.[11,12]

1.2 Motivation

The process of laser transformation hardening requires high energy, but does not have stringent demand for the laser beam quality, making it a feasible solution for manufacturers. Fiber laser has various important advantages over other types of lasers, such as simplicity, high electrical-to-optical efficiency, high reliability and low cost of operation.[12,13] Typically featuring similar wavelength of radiation to Nd:YAG laser, fiber laser is considered to be well suitable for processing of steel. As an alternative tool for material processing, the emergence of fiber lasers has brought a good opportunity to update the knowledge of laser technology of the industry. Investigations on surface treatment of steel with a fiber laser are essential to provide technical views of the hardening effect, influential parameters and optimization of this process. A comparison with other lasers can indicate the advantages and drawbacks of fiber lasers in hardening of steels. Such studies are expected to be of industrial interest and aid in future studies. However, despite some research work done in the past five years or so, this process has not yet been sufficiently investigated so far.[14,15]

Surface hardening of steel has been mostly studied with conventional hardness measurement which typically uses a load of several kilograms, yet metallographic analysis of specific phases and microstructures frequently demands local hardness measurement within a small region such as tens of micrometers. Unfortunately, such micro-scaled investigations on phase transformation and microstructural transition of laser surface hardened steel have not been much available. A microhardness test device uses a very small load (down to a few grams) and is capable to produce indentations within a few micrometers in diameter, making precise local and even in-grain hardness measurement possible. Microhardness measurement also provides a basis for quality control of thin metallic material and small parts of precision instruments.[16,17,18]

Heat transfer is a fundamental and crucial factor that has significant influence on the intermediate process of laser surface treatment.[19] To investigate the thermodynamic process, quantitative analysis using mathematical methods is required. A thermodynamic model can be developed based on heat flow theory to derive equations for the temperature distribution, the phase transformation boundary and the cooling rate.

Multi-track hardening has been previously investigated for the purpose of large-area treatment, but the decrease of hardness in the overlapping zone due to tempering remains to be a problem.[20,21] Laser linear oscillation scanning (LLOS) provides an alternative method for generating laser irradiated track with customizable width. This process is in nature a continuous multi-track surface irradiation in zigzag pattern, in which the treated region consists of a number of overlapped laser irradiated tracks. LLOS is thought to have good potential for practice, yet such studies have been rarely available so far. Investigation on this process is expected to review the influence of various frequencies and amplitudes of the oscillation on the produced hardness profile and to provide a solution in comparison with the surface treatment using shaping optics.

1.3 Research Objectives

The purpose of this study was to investigate the surface transformation hardening of steel with a fiber laser. Several topics were to be discussed in this thesis. An experiment was designed to reveal how laser power and laser power density influence the hardening effect of two medium-carbon steels, including an as-rolled high silicon steel and a pre-hardened mould steel. The experiment aimed to find the optimal laser power density for hardening. The influence of different initial microstructures of steel was to be investigated as well.

A microhardness test with an indentation load of 10 g was to be done in the hardened layer and in the base material of different types of steels. The microhardness in different microstructures was to be measured and compared. The effect of the grain size on the microhardness value was to be revealed as well. The measured microhardness values were to be compared with conventional macrohardness values.

A thermodynamic model was to be developed to describe the quasi-steady thermal process of a wide thin steel plate irradiated by a moving Gaussian laser beam. Equations were to be established for temperature distribution, transformation boundaries, homogenization time of austenite and cooling rate. The established model was to be verified with experimental results and correction coefficients are to be determined.

The effect of laser linear oscillation scanning (LLOS) was to be investigated. The test aimed to examine how the frequency and the amplitude of oscillation influence the

produced hardness profile of the surface. Equations were to be derived to calculate the overlapped width between adjacent scanning tracks and the number of overlapping tracks on laser irradiated area. Comparison was to be made between LLOS and single-track scanning with a simply defocused laser beam.

1.4 Structure of the Thesis

This thesis includes two parts. The first part gives an overview of the dissertation and consists of five chapters. Chapter 1 presents the background, motivation and research objectives of this study and contribution of the thesis. Chapter 2 provides the theoretical knowledge of laser transformation hardening of steel. Chapter 3 includes developed models and equations used in this study. Chapter 4 introduces the equipment and tested materials used in the experiments. Experimental procedures, processing parameters and measurement of the samples are described as well. Chapter 5 gives a review and summary of the research papers, which are fully included in the second part of the thesis. Chapter 6 presents the conclusions of this study and recommendations for further research work. The second part of the thesis consists of four research publications covering different topics about surface hardening of steel with a fiber laser.

1.5 Contribution of the Thesis

The thesis contains several novel aspects of the study on the surface hardening of steel with a fiber laser. The optimum power density that produced maximum hardness under different laser powers was determined for the tested materials. The effect of laser spot size on the hardened depth was evaluated while retaining the laser power unchanged. Tempered martensite was compared with ferritic-pearlitic steel in surface hardness, hardened depth and requirement for laser power density.

The microhardness analysis was done on various test samples. The influence of the grain size of rolled steel on the homogeneity of martensite and the microhardness was investigated. In-grain indentation was done to acquire the microhardness of ferrite, pearlite and cementite. The macrohardness of the base material of ferritic-pearlitic and pearlitic-cementite steels was compared with the microhardness of each phase structure. Rolled steel was compared with quenched and tempered steel and soft annealed alloyed steel on the surface hardness of martensite and hardened depth. The measured microhardness values were compared with macrohardness results.

A thermodynamic model was established for quasi-steady thermal process of a wide solid plate with limited depth irradiated by a moving Gaussian heat source. Equations were derived to calculate the temperature distribution, hardened depth, homogenization time and cooling rate. An experiment was done to verify the temperature cycle and hardened depth calculated with this model. Correction coefficients are applied to the equations for the tested materials.

LLOS process was tested with different laser powers, frequencies and amplitudes of oscillation at a constant feeding speed. Equations were developed to calculate the overlapped width between adjacent tracks and the number of overlapping tracks. The effects of the test parameters, especially the oscillation frequency on the homogeneity of surface hardness were investigated. The results were compared with single-track hardening process and the benefits and drawbacks of LLOS were concluded.

2 THEORETICAL BACKGROUND

2.1 General Process of Laser Surface Hardening

The mechanism of laser hardening is in principle very much similar to the conventional hardening processes. As illustrated in Figure 1, a defocused laser beam moves across the surface of the workpiece, quickly heating up the irradiated area to above the critical temperature of solid-state transformation but below the melting temperature, where the phase transformation of notably ferrite to austenite occurs. The contiguous material acts as a heat sink that rapidly cools the surface by thermal conduction. Such self-quenching effect allows the transformations from austenite to martensite. This process typically produces hard, wear-resistant regions on the surface of the workpiece while retaining the mechanical properties (e.g. toughness and ductility) of the bulk material unaffected.[22,23] Figure 2 illustrates the phase transformation and thermal cycle of 0.35 wt% C steel hardened by a laser.

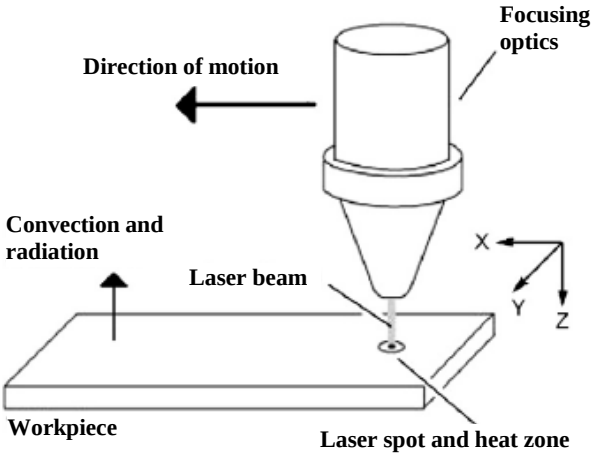

Figure 1. Basic setup of laser hardening of a flat plate workpiece.[24]

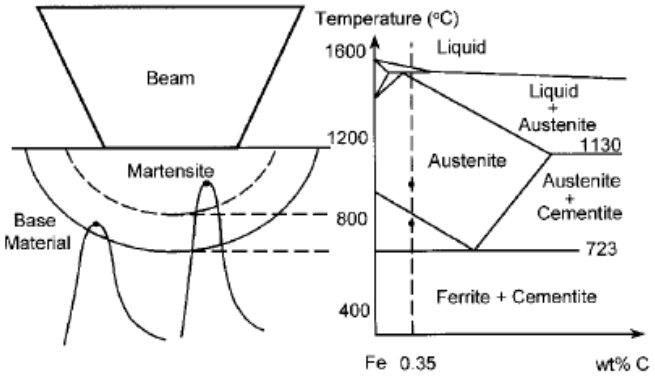

Figure 2. Principle of laser induced phase transformation. Thermal cycles at two positions in 0.35 wt% C steel are shown.[6]

2.2 Mechanism of Transformation Hardening

The production of martensite structure requires temperature-dependent transformation of the crystal structure of iron and redistribution of carbon content within the thermal cycle. As martensite is exclusively acquired by rapidly cooling of austenite, the austenitization temperature must be reached in the heating phase. In laser surface hardening, as the thermal cycle is much shorter than that of bulk hardening, the heating to austenitization temperature occurs in seconds or even a fraction of a second. Therefore, the heated area should be retained above the austenitization temperature for a sufficiently long period to allow carbon diffusion and homogenization of austenite. The heated surface should be maintained below the melting point of the material.[22,25]

2.2.1 Formation of austenite

Austenite is formed from pearlite-ferrite (hypoeutectoid steel) or pearlite-cementite (hypereutectoid steel) aggregate structure. In the heating phase, the body-centered cubic (BCC) α-iron solution transforms to face-centered cubic (FCC) γ-iron solution. In equilibrium transformation, austenite starts to form at A_{c1} temperature (723°C) in carbon steel and completes at A_{c3} (A_{cm}) line. This is indicated in Figure 3. Since the heating rate is quite high in laser hardening, the curve may shift much from the equilibrium condition and the A_{c3} line tends to move upwards to a higher temperature. Therefore, in order to achieve sufficient homogenization of austenite above the A_{c3} (A_{cm}) temperature, the process parameters are normally set to produce high peak temperatures. Yet since the short thermal cycle may cause insufficient carbon diffusion, the degree of homogenization of carbon in the base material has a significant influence on the carbon distribution of formed martensite and the produced hardness profile.[22,26]

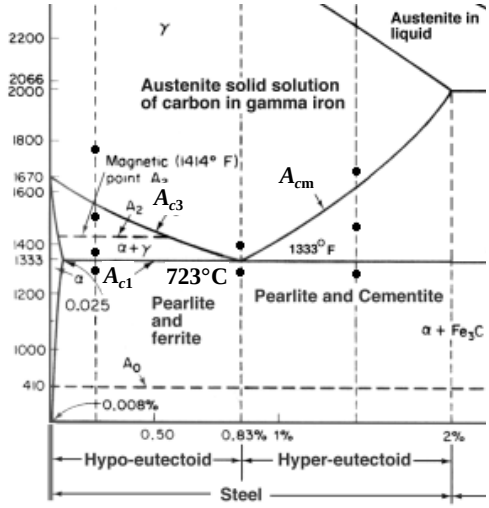

Figure 3. The Fe-C phase diagram.[27]

2.2.2 Formation of martensite

Formation of martensite is the transformation of γ-solid to α-solid, in which γ-lattice is rearranged into the α-lattice. Full martensitic transformation occurs with relatively high cooling rate, typically tens of Celsius degrees per second or above. In this case, carbon atoms solved in the γ-austenite do not have adequate time to precipitate and thus remain in the transforming lattice.[28,29] Therefore, martensite is a supersaturated solution of carbon in α-iron. The trapped carbon atoms in the lattice result in slight shift of the iron atoms and thus a body-centered tetragonal (BCT) lattice is formed. Figure 4 shows the BCT lattice structure of martensite. The BCT lattice is like a vertically elongated BCC crystal lattice, which has greater deformation in the direction of one of the axes than in the other two, and thus features high internal stresses that make martensite hard but also brittle.[29,30]

In the cooling phase, transformation of austenite to martensite starts from the martensite start temperature (M_s) and ends at the martensite finish temperature (M_f). Martensite is formed over a certain temperature range, which depends on the carbon content of steel, as indicated in Figure 5. The M_s temperature depends little on the cooling rate. Increased carbon content decreases the M_s and M_f temperatures and consequently lowers the required critical cooling rate. Besides, the alloying elements such as Mn and Ni lower the M_s temperature as well.[31,32] As the temperature reaches the martensite start temperature in the cooling phase, the cooling rate is required to exceed the critical cooling rate in order to produce 100% martensite. Figure 6 shows the continuous cooling transformation (CCT) diagram for eutectoid carbon steel. Dashed line A which is tangent to the austenite-pearlite transformation start line represents the cooling curve with exactly the critical cooling rate. Leftward is the

region with higher cooling rate which produces pure martensite as well. Dashed line B indicates the highest cooling rate that produces 100% pearlite. Rightward is lower cooling rate that results in pure pearlite. The region between dashed line A and B represents production of a mixture of martensite and pearlite as the final microstructure. Since martensite is exclusively transformed from austenite, the produced austenite in the heating phase of the thermal cycle determines the maximum amount of martensite that can be formed in the cooling phase. Adding alloying elements tends to shift the C curve to the right and thus reduces the critical cooling rate.[25,30] In laser hardening, the cooling rate by heat conduction into the substrate is normally high enough for martensitic transformation even in low carbon steel.[6]

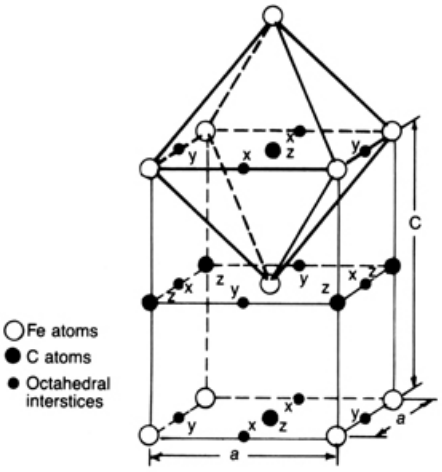

Figure 4. The body-centered tetragonal (BCT) lattice structure of martensite.[25]

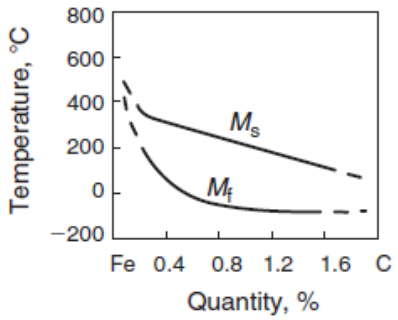

Figure 5. Martensite start (M_s) and finish (M_f) temperatures versus carbon content.[31]

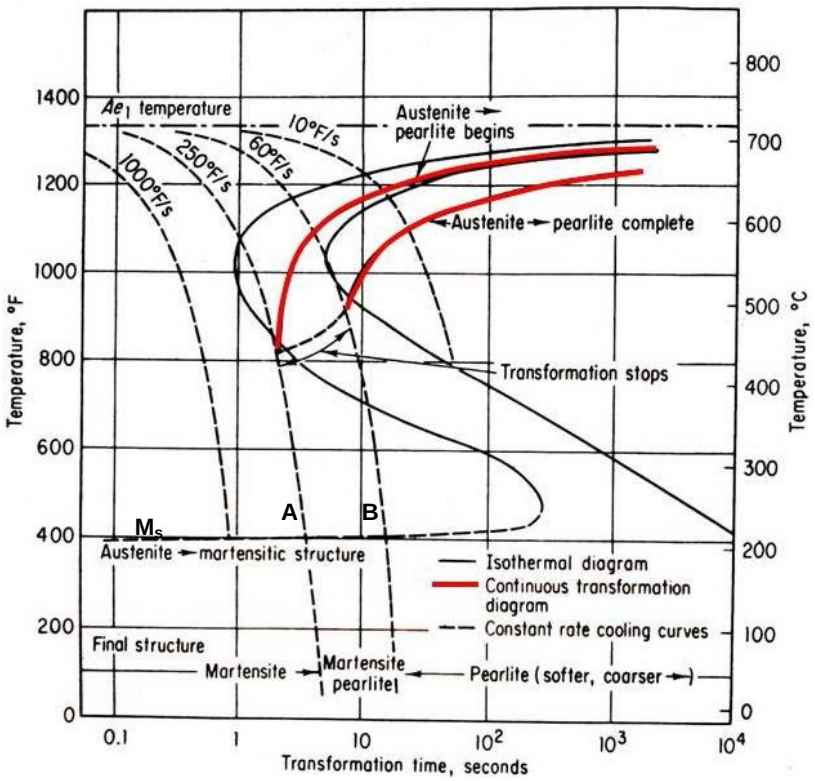

Figure 6. Continuous cooling transformation (CCT) diagram for eutectoid carbon steel.[30]

2.2.3 Retained austenite

Some of the austenite can be retained during the quenching to room temperature, reducing the hardness of the steel. There are multiple factors that may cause this, such as local carbon concentration due to the inhomogeneity of material and existence of the austenite-stabilizing elements. As the concentration of carbon increases, both the M_s and M_f temperatures are lowered (M_f may be even lower than the room temperature). When the room temperature is reached during cooling, though most of the austenite may have transformed to martensite, some amount of austenite can still remain in the structure. Some substituting alloying elements such as Mn and Ni reduce the M_s and M_f temperatures as well and thus can increase the amount of retained austenite. As a common practice, the retained austenite can be transformed to martensite by subzero treatment (i.e. cooling to below -70°C) or by tempering.[25]

2.3 Steels Suitable for Transformation Hardening

Low alloy carbon steels, featuring combined properties of strength, toughness and wear-resistance, are of the most often used material for transformation hardening.

Medium carbon steels (0.25-0.5 wt% C) are well responsive to heat treatment. Yet since the increase of carbon content reduces the fracture toughness remarkably, these steels are normally treated with hardening and tempering process. Plain carbon steels (0.16-0.25 wt% C) can only be heat treated in small sections with rapid quenching. Low carbon steels (less than 0.1 wt% C) are rarely used for transformation hardening. High carbon steels (0.5-2.0 wt% C), also known as tool steels, are brittle and therefore normally alloyed with elements such as Cr and V to improve toughness.[6,33]

Medium alloy steels, alloying additions between 2% and 10%, may be hardened by laser heat treatment, although retained austenite is often observed in the as-hardened microstructure. Quenching in liquid nitrogen is an effective method to improve the transformation of austenite to martensite and produce hardness of up to 1000 HV. High alloy steels, containing more than 10% of deliberate alloying additions, generally respond more poorly to transformation hardening in comparison to other types of steels due to the large amount of retained austenite at the room temperature.[6,33]

Only martensitic grades of stainless steels contain sufficient carbon to allow laser hardening. The effect of hardening is dependent on the initial condition of the steel as well as the Cr content. Laser treatment of martensitic stainless steels delivered in the annealed condition, consisting of ferrite and carbide microstructures, results in significant amount of carbide dissolution and thus benefits the formation to martensite on cooling.[6,33]

2.4 Influential Parameters

The laser hardening process can be influenced by many factors. The effect of hardening basically depends on the material, laser and processing parameters.

2.4.1 Material properties

- Composition and microstructure

The surface hardness depends on the hardness of the martensite formed. To form martensite, the material for laser hardening should typically contain at least around 0.05 wt% carbon. The surface hardness generally increases linearly with the carbon content. However, carbon content higher than about 0.6 wt% may result in a much higher amount of retained austenite present at room temperature and may thus reduce the hardness.[6,25] High content of alloying elements such as Mn, Cr, Ni and Mo increases the volume of retained austenite as well, therefore the hardening effect of alloy steel is distinctly more affected by the alloying additions in conjunction with the carbon content.[34] Alloying elements also influence the thermal properties of the substrate. When the thermal conductivity is increased, the peak temperature on the surface is decreased and the thermal penetration rate is higher.[35] In hypoeutectoid

steel consisting of ferritic-pearlitic structures, the grain size of the starting microstructures has significant influence on carbon diffusion and thus affects the hardening result. For eutectoid steel, the carbon diffusion is mostly affected by the interlamellar spacing in pearlite. In hardening of tempered martensitic steel, carbon content is the most crucial factor.[6,25] Carbon distribution in finer initial grains can be homogenized more readily in the treatment, resulting in martensitic formation with little retained austenite.[25]

- Geometry

The geometry of the workpiece affects the heat flow distribution. As an empirical rule, the thickness of the workpiece should be at least ten times of the desired hardened depth so that the self-quenching can occur without significant bulk heating. A discrete distance should be preserved between the laser irradiated tracks and the edges to prevent overheating or melting. External corners have a large surface-to-volume ratio and thus are susceptible to overheating. Internal corners are to the opposite.[36]

- Surface roughness

Multiple reflections on a rough surface may improve the absorption of laser irradiation over a flat, smooth surface. As reported in earlier studies, increasing the surface roughness of metal to a scale much larger than the laser wavelength may increase the absorptivity of laser energy up to several times, depending on the material and the type of laser.[37,38]

2.4.2 Laser parameters

- Wavelength

Figure 7 compares the absorption of laser radiation at different wavelengths for diverse metals. As different kinds of steels absorb CO_2 laser beam radiation with quite a low efficiency (around 2-5%), traditional CO_2 laser hardening of steel requires surface coating before the treatment to increase the absorption of laser energy. Later developed high power Nd:YAG, diode and diode pumped fiber lasers feature much shorter wavelength (around 1000 nm and lower). These wavelengths can be absorbed by steels in a proportion of about 35% or even higher and thus surface coating or other pre-treatments are not needed.[10,39]

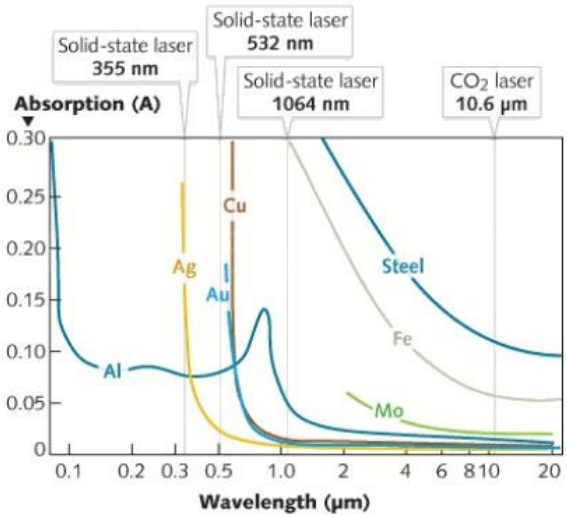

Figure 7. The absorption of laser radiation at different wavelengths for various metals.[7]

- Laser power and laser power density

Figure 8 compares various laser processes in terms of laser power density against beam interaction time. The laser power density used in laser hardening is usually around 10^3-10^5 W/cm^2, which is relatively low among laser processes.[6]

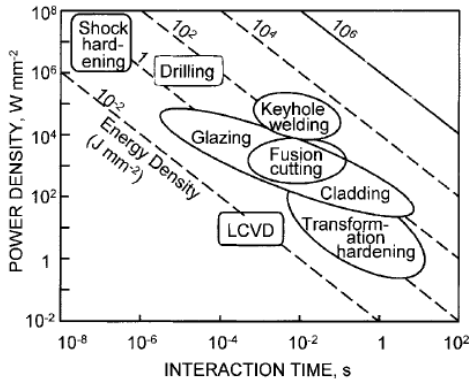

Figure 8. Beam interaction time vs. power density illustrating the empirical window for various laser processes.[6]

In practice, hundreds of watts to several kilowatts are often used for surface hardening, depending on the traverse speed and the material hardenability. Generally, steels of high hardenability may be treated with low laser power density and a long interaction

time in order to produce a homogeneous hardened region with significant depth. For steels of low hardenability, high laser power density and short interaction time may be used to achieve the high cooling rate demanded for martensite formation, at the expense of a shallow hardened layer.[27,32]

- Geometry and power distribution of laser irradiation

The heating pattern normally resembles the mirror image of the raw beam power distribution, although with decreased amplitude and rounded edges. For example, a Gaussian power distribution typically generates a hemispherical hardened zone, and a uniform power distribution generates a rectangular hardened section with rounded edges. For specific power density and traverse rate, there is an optimal range of beam width that is capable to produce a large hardened width without surface melting.[40] Lots of engineering processes employ rotationally symmetric laser beams which are created via defocusing optics. Shaping optics is as well used to provide various shapes of hardened sections with desirably high coverage rates. The aspect ratio (width-to-length ratio) can be varied to produce desired thermal cycle and section geometry. A high aspect ratio causes a rapid thermal cycle and a wide hardened track. To satisfy more customized requirements, a variety of optics can be used, as given in Table 1.[41]

Uniform-distribution, ring and Gaussian profiles are common power distribution patterns. Uniform power distribution in the beam profile features maximized hardening depth, uniformity of depth and coverage rate. Ring and Gaussian beam profiles minimize distortion, but the latter can cause melting in the center. The optimal power distribution in the heating pattern should include a leading edge of a high power density with the power tailing off towards the trailing edge. This benefits the hardening process by inducing a thermal cycle with sufficient time for microstructural homogenization while ensuring a high-enough cooling rate for martensite formation. This pattern also minimizes the energy required per unit volume of hardened section. The optics needed to produce such a heating pattern, however, can be expensive.[42,43]

Table 1. Optics applied in laser hardening and corresponding features.[41,45]

Optics	Features
Kaleidoscope	produces uniform profile of constant hardened depth cheaply
Scanning mirror	provides linear beam profile using a parabolic reflective mirror
Diffractive optics	transforms the raw beam into suitable heating pattern, yet is expensive
Beam rastering system	allows complex or variable geometries, but is normally used with low power levels and expensive
Toric mirror or annular beam	hardens both the inner and outer surfaces of rotationally symmetric components, e.g. cylinders and shafts
Beam splitting lenses	splits the beam into several ones to produce spot hardened patterns

2.4.3 Process parameters

- Process gas

The process gas basically has two functions in laser transformation hardening. It can shield the irradiated region on the surface against oxidation, which may increase the absorptivity and cause overheating or melting. The process gas also protects the optics from being contaminated during the process. Argon and nitrogen are commonly used due to their effective coverage of the interaction zone. The gas flow is usually ejected to the material at a rate of about 20 L/min from a coaxial or external nozzle.[6,32] Pantsar compared diode laser hardening of steel in argon and in air and indicated that surface oxidation may result in markedly higher absorptivity of laser energy.[10]

- Traverse speed

The traverse speed strongly affects the time of laser irradiation received by the material. Laser power density in an order of 10^3-10^5 W/cm^2 with a typical interaction time of 0.1-0.3 seconds can produce martensite structure in steel. As the beam length in the traverse direction is determined by required laser power density and the track width, the traverse speed can be calculated by dividing the beam length with the interaction time. The traverse speed is normally the parameter that is fine-tuned to optimize the process in order to obtain the required hardened depth and degree of homogenization.[46]

2.5 Industrial Applications of Laser Hardening

Since laser hardening was introduced on an industrial scale in 1973, the automotive and machine tool industries have been responsible for much of the laser heat treatment process development. Some of the applications are given in Table 2.[4,47]

Table 2. Optics applied in laser hardening and corresponding features.

Industry sector	Component	Material
Automotive	Torsion springs	DIN 58CrV4 steel [48]
Automotive	Blanking die	Tool steel [49]
Automotive	Engine valve	Alloy steel [50]
Automotive	Hand brake ratchet	Low carbon steel [51]
Domestic goods	Typewriter interposer	AISI 1065 steel [52]
Machine tools	Cutting edge	Steel [51]
Machinery	Gear teeth	AISI 1060/ low alloy steel [53]
Machinery	Capstan	AISI 1045 Steel [54]
Machinery	Mandrel	Martensitic stainless steel [55]
Power generation	Turbine blade edge	Martensitic stainless steel [56]

2.6 Comparison of Laser Hardening with Competing Hardening Methods

Some alternative hardening methods with different characteristics have been used for decades in industrial processes, such as induction hardening, carburizing, flame hardening, arc hardening and electron beam hardening.[57] Laser hardening is compared with these competing methods in Table 3. Laser hardening benefits from high scanning speed, self-quenching with no need of external quenchants, low distortion of the workpiece, selectable area of treatment, less or no post-treatment required, ease for computer control and low environmental impact.

The use of laser heat treatment has generally several issues for concern. Many applications demand homogeneous laser energy distribution. The coverage area is restricted and multiple passes cause local tempering. The temperature field ensuring the targeted microstructural change is normally very narrow. It is difficult to adjust the kinematic conditions of the workpiece or the laser beam for complicated surface shapes. The absorptivity of laser irradiation by metallic material surface is relatively low. The equipment cost is relatively high compared with traditional hardening processes.[37]

Table 3. Comparison of laser hardening with other available methods.[6,57]

Treatment	Laser	Electron beam	Induction hardening	Carburizing	Flame	Arc
Max. treatment depth, mm	1.5	1	5	3	10	10
Distortion	very low	very low	medium	medium	high	medium
Flexibility	high	medium	low	medium	high	high
Precision	high	high	medium	medium	low	low
Operator skill	medium	medium	medium	medium	high	high
Environmental impact	low	low	low	high	medium	medium
Quenchant required	no	no	sometimes	no	yes	no
Material flexibility	high	high	medium	low	medium	medium

3 MODELLING AND CALCULATIONS

In this chapter, a thermodynamic model was developed to investigate the quasi-steady thermal process of a wide thin steel workpiece irradiated with a moving Gaussian laser beam. For more detailed calculations, see paper 3. For LLOS, equations were also derived to calculate the overlapped width between adjacent scanning tracks and the number of overlapped scans in the center of oscillation. For more detailed calculations, see paper 4.

3.1 Surface Heating of a Wide Thin Solid Plate with a Moving Gaussian Laser Beam

Heat transfer is a fundamental and crucial factor that has significant influence on the intermediate process and the result of laser surface treatment.[19,58,59] To investigate the thermodynamic process, qualitative and quantitative analysis using mathematical methods are thus required. In practice, a simply defocused Gaussian laser beam is often used as the heat source for surface treatment, although special optics can be installed for desired shape and energy distribution of laser irradiation. The defocused beam profile inherits the Gaussian energy distribution of the raw laser beam.[60,61,62] Some previous studies were attempted to solve the temperature field induced by a moving heat source. One of the earliest works was done in 1950's by Rykalin who developed an analytical solution for the temperature distribution in a semi-infinite solid with a point heat source moving on the surface.[63] Cline and Anthony used the heat-source superimposition method to give a numerical solution for heating a semi-infinite domain with a Gaussian heat source.[64] Manca, Morrone and Vaso solved the temperature distribution induced by a moving Gaussian heat source in a finite domain.[65] Despite the previous studies, further modelized study is needed to develop equations for the important parameters of laser surface treatment of steel (e.g. phase transformation boundary and cooling rate) and provide solutions for them. Influence of laser power, laser traverse speed and depth of the workpiece are also studied. To solve the temperature distribution in a finite-depth solid with a moving Gaussian heat source, an analytical solution can be very complicated but the calculation can be done numerically with very high precision via computational tools.[66]

Figure 9 shows the dimensions of the workpiece and the coordinate system. A defocused circular laser beam with Gaussian energy distribution is used as the laser source. A fixed coordinate system is established, with the origin set in the center of the laser spot on the surface of the workpiece. The laser beam is parallel to the *z*-axis and the laser spot moves at a speed v_x along *x*-axis. The laser irradiated track is generally kept remote to the edges and the corners to avoid overheating. Earlier studies indicated that the temperature profile for $l/2>10r_b$ is very close to that produced by an infinite-width solid.[67] Thus the temperature on the four perpendicular edge planes parallel to the *z*-axis can be assumed to remain at the initial temperature.

To simplify the establishment of the model, some assumptions are applied:

- Radiative heat loss from the surface is negligible compared to the heat conducted into the bulk material;
- Absorptivity (β) of laser energy is treated as a constant that equals to the average value over the temperature range of laser irradiation. The absorptivity can be calculated by measuring the absorbed laser energy via a liquid calorimeter.[10]
- The latent heat of the α- to γ-transformation is negligible.
- The length (l) and the width (d) of the workpiece along y-axis and x-axis are large enough so that the material at the corresponding surfaces other than the irradiated surface and its opposite surface remain at the initial temperature;
- The material is homogeneous with constant physical properties during the whole process. Thus, the thermal conductivity and the specific heat are assumed to remain unchanged. The parameters are obtained at a temperature within the range of the temperature cycle.
- Heat flow occurs under a quasi-stable state, meaning that the heated material of a constant volume moves together with the heat source at the same velocity;
- Radius of the Gaussian beam is the distance from the beam center to the position where the power density is $1/e^2$ times of the peak value;
- Melting does not occur, demanding that the surface temperature is sufficiently below the melting point of the material.

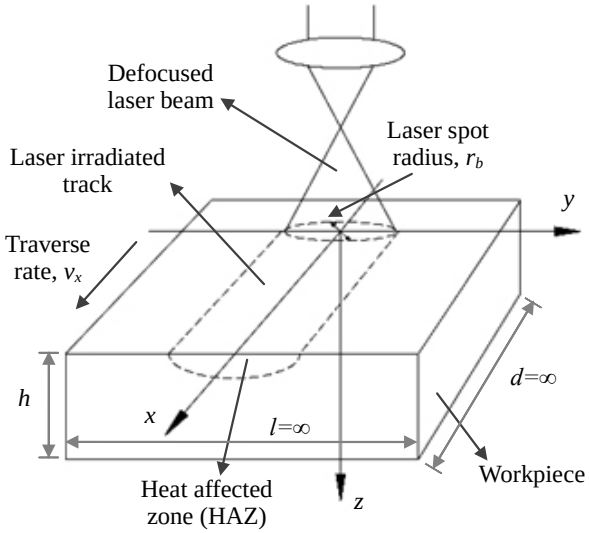

Figure 9. Dimensions of the solid workpiece and the coordinates.

According to the heat flow theory, the heat transfer without convection in a three-dimensional isotropic and homogenous solid workpiece can be expressed as:[68]

$$\frac{1}{\alpha}\frac{\partial T}{\partial t} - \nabla^2 T_i = \frac{U}{k} \tag{1}$$

where T is the temperature of the workpiece,
T_i is the temperature increase above the initial temperature of the workpiece,
t is time,

$\alpha = \frac{k}{\rho C_p}$ is the thermal diffusivity. k is the thermal conductivity, ρ is the mass density and C_p is the specific heat capacity,
U is the heat generated per unit volume.

Equation (1) can be converted to:

$$\frac{U}{\rho C_p} = \frac{\partial T}{\partial t} - \alpha \nabla^2 T_i \tag{2}$$

The whole thermal dynamic effect can be regarded as the superposition of multiple heat sources located at earlier coordinates (x', y', z', t'), which can be treated as unit point sources influencing the temperature at a later position (x, y, z, t).

Define $f(x, y, z, t) = \frac{U}{\rho C_p}$, the temperature distribution can thus be expressed as:

$$T_i(x, y, z) = \int_0^t \int_{-\infty}^{+\infty} \int_{-\infty}^{+\infty} \int_0^{+\infty} f(x', y', z', t') \cdot G(x', y', z', t' | x, y, z, t) dz' dy' dx' dt' \tag{3}$$

where G is the Green's function for the diffusion equation.

The Green's function for the heat equation in a domain with infinite length (x-axis) and width (y-axis) and with a finite depth (z-axis) can be written as below:[69,70]

$$G(x, y, z, t | x', y', z', t') = \exp\left[-\frac{r^2}{4\alpha(t-t')}\right] \cdot \frac{1}{4\pi\alpha(t-t')h}$$
$$\times \left\{1 + 2\sum_{n=1}^{\infty} \exp\left[-\frac{n^2\pi^2\alpha(t-t')}{h^2}\right] \cos\frac{n\pi z}{h} \cos\frac{n\pi z'}{h}\right\} \tag{4}$$

where $r^2 = (x-x')^2 + (y-y')^2 + (z-z')^2$. On the surface, $z' = 0$.

$$\int_0^{+\infty} f(x',y',z',t')\cdot G(x',y',z',t'|x,y,z,t)dz' = I(x',y',t')\cdot G(x',y',t'|x,y,t) \quad (5)$$

Substituting Equation (5) into Equation (3) gives:

$$T_i(x,y,z) = \int_0^t \int_{-\infty}^{+\infty}\int_{-\infty}^{+\infty} \frac{I(x',y',t')}{\rho C_p}\cdot G(x',y',t'|x,y,t)dx'dy'dt' \quad (6)$$

The power density of an ideal Gaussian laser beam traversing on the surface of a workpiece can be written as:[71]

$$I(x,y,t) = \frac{2P_0}{\pi r_b^{\,2}}\exp\left[-\frac{2\left[(x-v_x t)^2+y^2\right]}{r_b^{\,2}}\right] \quad (7)$$

where P_0 is the absorbed laser power,
r_b is the radius of the laser beam,
v_x is the traverse speed of the laser beam along x-axis.

The temperature increase T_i can thus be calculated by substituting Equation (4) and Equation (7) into Equation (6):

$$T_i(x,y,z) = \frac{P_0}{\rho C_p \pi h}\int_{-\infty}^{t} \frac{1}{8\alpha(t-t')+r_b^{\,2}}\cdot\exp\left(-\frac{2\left[(x-v_x t')^2+y^2\right]}{8\alpha(t-t')+r_b^{\,2}}\right)$$

$$\times\left\{1+2\sum_{n=1}^{\infty}\exp\left[-\frac{n^2\pi^2\alpha(t-t')}{h^2}\right]\cos\frac{n\pi z}{h}\right\}dt' \quad (8)$$

At $t=0$, Equation (8) represents the temperature distribution produced by a Gaussian laser beam when it was at a position (x',y') at an earlier time t'. Thus Equation (8) is converted to:

$$T_i(x,y,z) = \frac{P_0}{\rho C_p \pi h}\int_{0}^{+\infty} \frac{1}{8\alpha t'+r_b^{\,2}}\cdot\exp\left(-\frac{2\left[(x+v_x t')^2+y^2\right]}{8\alpha t'+r_b^{\,2}}\right)$$

$$\times\left\{1+2\sum_{n=1}^{\infty}\exp\left(-\frac{n^2\pi^2\alpha t'}{h^2}\right)\cos\frac{n\pi z}{h}\right\}dt' \quad (9)$$

Equation (9) is the basic equation used to solve the distribution of T_i and also provides

an approach for analyzing the transformed boundary, the homogenization time and the cooling rate.

3.2 Surface Scanning with a Linear Oscillating Laser Beam

3.2.1 The overlapped width between adjacent tracks

Figure 10 schematically describes the overlapping tracks of LLOS. The laser spot travels from position O_1 to O_2 in one period of oscillation following the sine wave form. At the edge of oscillation, the laser spot moves along the feeding direction for a distance S_{e0}, which can be calculated by:

$$S_{e0} = \frac{v_x}{\mu} \tag{10}$$

where μ is the frequency of oscillation

Thus the overlapped width at the edge of oscillation S_{eov} can be expressed as:

$$S_{eov} = d_0 - S_{e0} \tag{11}$$

where d_0 is the diameter of the laser spot.

Substituting Equation (10) in to Equation (11) gives:

$$S_{eov} = d_0 - \frac{v_x}{\mu} \tag{12}$$

At the center of the oscillation, the overlapped width S_{cov} can be calculated as:

$$S_{\mathrm{cov}} = d_0 - \frac{v_x}{2\mu} \tag{13}$$

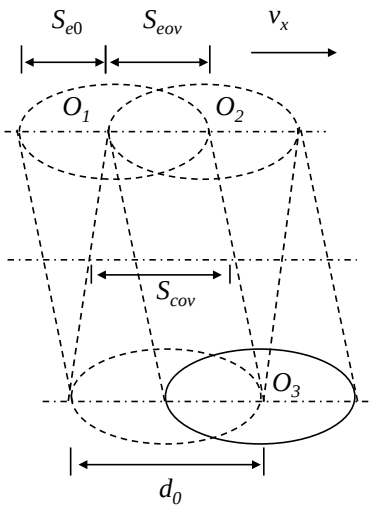

Figure 10. Schematic diagram of overlapping tracks in LLOS.

3.2.2 The number of overlapped tracks in the center of oscillation

During the oscillation scanning process, a position in the middle of the oscillation width may experience multiple times of laser irradiation. According to Figure 10, the number of scans, N_c is the integral part of the ratio of d_0 to S_{e0} expressed by:

$$N_c = 2\left[\frac{2d_0}{S_{e0}}\right] \tag{14}$$

Substituting Equation (10) into (14) gives:

$$N_c = 2\left[\frac{2d_0\mu}{v_x}\right] \tag{15}$$

4 EXPERIMENTAL INVESTIGATION

To achieve the objectives of this study, experimental investigations were done using the high power fiber laser system. Hardening tests were designed and performed to investigate four research problems on surface transformation hardening of carbon steel with a fiber laser. The research problems include:

(i) The influence of laser power and laser power density on the hardening effect of medium-carbon steel and the optimal laser power density for the highest hardness under different laser power.

(ii) Microhardness analysis of laser hardened steels with different carbon and alloy content and initial microstructures.

(iii) A thermodynamic model that can be used to calculate the temperature cycle, transformation boundary, homogenization time and cooling rate of wide thin steel plate surface treated with a Gaussian laser beam.

(iv) The effect of laser linear oscillation hardening (LLOS) of steel and its comparison with conventional single-track scanning.

The results of the experimental investigations are summarized in Chapter 5 and are reported extensively in the research papers in the second part of this thesis.

4.1 Experimental Equipments

4.1.1 The fiber laser system

This study used an ytterbium multi-mode fiber laser (model YLR-5000-S) produced by IPG Photonics (shown in Figure 11), which was installed in a CNC XY work table. The laser system produced a maximum nominal output power of 5 kW. A fiber cable with the length of 30 m and the bending radius of 100 mm (unstressed) or 200 mm (stressed) were included in the device. The fiber laser worked in CW/QCW mode and produced a randomly polarized circular laser beam with a wavelength of 1070-1080 nm and a beam parameter product (BPP) of 4-4.5 mm·mrad. The emission linewidth was 3-6 nm. The switching on/off time of the equipment was 80-100 μs.[72] An output fiber with a core of 200 μm in diameter was used to transfer the laser beam to the Precitec YW50 laser head, as indicated in Figure 12. In this study, a collimator and a focusing lens both with a focal length of 150 mm were used in the optical system.

Figure 11. The YLR-5000-S multi-mode fiber laser.

Figure 12. Precitec YW50 laser head.[73]

4.1.2 The DC-Scanner

In the laser linear oscillation scanning (LLOS) test of this study, the ILV DC-Scanner was used to replace the beam bender inside the laser head. The DC-Scanner, which was primarily designed for laser welding applications, contained a parabolic scanner mirror with the focal length of 250 mm and a digital controller unit connected to it. Figure 13 shows the mirror unit and the controller unit of the DC-Scanner. The amplitude that can be chosen was restricted by the oscillation frequency.[74] This study used oscillation frequencies of 10, 20, 40 and 100 Hz, under which the oscillation amplitude of up to 11 mm can be achieved. The controller unit provides external adjustment of the laser power profile. It supports programming of different laser power levels at up to 32 individual positions across the width of scanning.

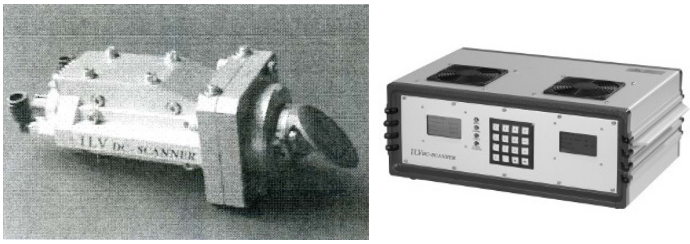

(a) (b)

Figure 13. Components of the ILV DC-Scanner. (a) the mirror unit; (b) the controller unit.[74]

4.2 Tested Materials

The hardening tests were done on low-, medium- and high-carbon steel samples with various alloy contents and microstructures caused by different pretreatment conditions. Table 4 gives the compositions of the materials. The thermal properties of Material 1, 2, 4, 5, 6 and 7 are shown in Table 5.

Table 4. Samples used in the tests. The compositions were provided by the steel manufacturer.

Mat. no.	Grade	Delivered condition	Composition (wt%)						
			C	Si	V	Cr	Mn	Ni	Mo
1	AISI 4820	hot rolled	0.20	0.19	0.01	1.14	1.20	0.21	0.06
2	AISI 4340	Q&T	0.35	0.33	0.01	1.40	0.70	1.36	0.17
3	Imamic	as rolled	0.36	1.26	0.12	0.20	1.08	0.14	0.03
4	AISI 5210	through hardened	0.95	0.25	0.01	1.43	0.39	0.14	0.02
5	AISI P20 mod.	Q&T	0.37	0.37	0.01	1.86	1.47	1.17	0.20
6	AISI H13	soft annealed	0.39	0.97	0.92	4.95	0.34	0.24	1.26
7	AISI H10 mod.	soft annealed	0.40	0.38	0.83	2.80	0.73	0.10	2.17

Material 1 was an alloyed case hardening steel used for heavy and high strained parts with high demands on toughness. Material 2 was a low-alloy steel containing Ni, Cr and Mo, featuring toughness and high strength after heat treatment while retaining good fatigue strength. Material 3 was an as-rolled high-silicon steel with higher fatigue strength than conventional micro-alloy steels. Material 4 was a high-carbon, Cr low-alloy steel that was through-hardened and noted in particular for use as bearings. Material 5 was a vacuum degassed Cr-Ni-Mo-alloyed mould steel featuring

hardness, toughness and polishability. Material 6 was a hot work Cr type tool steel that maintains high hardness and strength at elevated temperatures. Material 7 was a hot work, Cr-Mo type tool steel with very high resistance to softening and thermal fatigue cracking at elevated temperatures.[75,76,77]

Material 1 and 3 contained ferrite and pearlite with distinct grain boundary. Quenched and tempered Material 2 and 5 were composed of tempered martensite structures. Material 4 consisted of pearlite and cementite grains. Soft annealed Material 6 and 7 contained ferrite and fine granular pearlite.

Table 5. Thermal properties of Material 1, 2, 4, 5, 6 and 7.[75,76]

Mat. no.	Thermal conductivity, k, W/(m·K)*	Thermal diffusivity, α, mm^2/s	A_{c1}, °C	A_{c3}/A_{cm}, °C
1	42.0	9.11	740	835
2	33.7	8.15	715	770
4	20.0	4.33	755	850
5	29.0	6.30	722	760
6	26.5	6.53	820	915
7	33.0	6.58	790	890

*k values are acquired at 600°C.

4.3 Processing Parameters

The experiment for this study included four tests designed and done on various materials with different processing parameters. Raw materials were machined into round plates with a diameter of 6.5-8.7 mm and a thickness of 10 mm. The irradiated surface was clean and the roughness, R_a, was about 2.5 µm. The initial temperature of the tested samples was around 20°C (room temperature). The angle between the optical axis and the surface was 90 degrees. The laser scanning tracks were kept with sufficient distance away from the edge of the workpiece to avoid overheating and surface melting. No shielding gas was used. The tested samples were air-cooled after the process. Specific processing parameters were used in each test for different topics of this study.

4.3.1 Test 1

Test 1 used Material 3 and 5 to investigate the effect of laser power and laser power density on the hardening result. The processing parameters are shown in Table 6. The radius of the laser spot was measured as the distance from the center to the position where the laser power density (I_p) is $1/e^2$ times of its peak value. I_p was altered via changing the laser spot diameter (d_s), which was done by adjusting the distance off the focus from 45 to 180 mm. Test 1 was done with a constant traverse speed of 8.0 mm/s.

Table 6. Laser power density and laser spot diameter used in Test 1.

Mat.	Laser	Laser power density, I_p, kW·cm^{-2}/Laser spot diameter, d_s, mm			
no.	power, P, W	A	B	C	D
3	955	7.22/4.1	8.28/3.8	9.59/3.6	11.23/3.3
3	1423	7.50/4.9	8.40/4.6	9.47/4.4	10.77/4.1
3	1900	6.15/6.3	6.71/6.0	7.37/5.7	8.12/5.5
3	2840	5.07/8.4	5.79/7.9	6.67/7.4	7.78/6.8
3	3788	5.01/9.8	5.62/9.3	6.34/8.7	7.21/8.2
5	944	10.96/3.3	12.98/3.0	15.61/2.8	19.11/2.5
5	1409	12.09/3.9	13.98/3.6	16.35/3.3	19.37/3.0
5	1883	12.43/4.4	14.11/4.1	16.16/3.9	18.69/3.6
5	2816	11.95/5.5	13.23/5.2	14.72/4.9	16.49/4.7
5	3750	11.08/6.6	12.06/6.3	13.17/6.0	14.45/5.7

4.3.2 Test 2

Test 2 used Material 1-7 to examine the microhardness results of various laser hardened steels. The test was done with a constant laser power of 1875 W and a distance off the focus of 80 mm to produce a laser power density of 12.74 kW/cm^2. Test 2 used a constant traverse speed of 8.0 mm/s.

4.3.3 Test 3

Test 3 was designed to verify the temperature cycle and the hardened depth predicted by the thermodynamic model. Material 1, 2, 4, 5, 6 and 7 were used. All the samples were tested with the laser power of 1875 W, the traverse speed of 8.0 mm/s and the distance off the focus of 80 mm. Material 2 was also tested with a 2988 W laser beam with various traverse speeds. The processing parameters are shown in Table 7. The absorptivity of laser energy by the samples were estimated based on a previous study by Pantsar and Kujanpää, who investigated the absorption of laser irradiation by low alloy carbon steel with a high power diode laser that produces radiation at wavelengths of 800±10 nm and 940±10 nm.[78] For carbon steel, the absorptivity of these wavelengths is close to that of the 1070-1080 nm radiation produced by the fiber laser used in this study.[7] Therefore, the absorptivity values obtained by Pantsar and Kujanpää was used in this test.

Table 7. Processing parameters used in Test 3.[78]

Mat. no.	Laser power, P, W	Radius of laser beam, r_b, mm	Absorptivity, A	Traverse speed, v_x, mm/s
1	1875	2.19	64%	8.0
2	1875	2.19	64%	8.0
4	1875	2.19	64%	8.0
5	1875	2.19	64%	8.0
6	1875	2.19	64%	8.0
7	1875	2.19	64%	8.0
2	2988	1.80	62%	32.0
2	2988	1.80	61%	34.0
2	2988	1.80	60%	36.0
2	2988	1.80	59%	38.0
2	2988	1.80	58%	40.0
2	2988	1.80	57%	42.0

4.3.4 Test 4

Test 4 was a laser linear oscillation scanning (LLOS) test done on Material 2. The distance off the focus was 60 mm, producing a laser spot of 2.1 mm in diameter. The oscillation speed, determined by the amplitude and the oscillation frequency, followed the sine wave form. The parameters are given as process A1 to A6 in Table 8. To avoid melting at the edge of oscillation, the laser power output was programmed via the controller unit to generate an approximately sine wave power profile (see Section 4.4 for details). For comparison, a conventional single-track scanning test was done, shown as process B1 and B2 in Table 8. 2020 and 3020 W laser powers with an off-focus distance of 75 mm were used to produce laser power density of 15.14 and 22.63 kW/cm^2, respectively. The feeding speed was constantly 15 mm/s in Test 4.

Table 8 Processing parameters of Test 4.[74]

Test	Laser power, P, W	Oscillation frequency, μ, Hz	Amplitude, A, mm
A1	2020	10	11.0
A2	2020	20	8.5
A3	2020	40	4.5
A4	3020	20	10.0
A5	3020	40	7.4
A6	3020	100	5.9
B1	2020	NA	NA
B2	3020	NA	NA

4.4 Laser Beam Profile

Test 1, 2 and 3 used a focusing lens with the focal length of 150 mm to defocus the raw fiber laser beam. To achieve the suitable laser power density for the hardening purpose, the distance off the focus was adjusted to acquire the desired laser spot diameter with appropriate laser power. The laser power distributions at various distances off the focus were measured, as illustrated in Figure 14. The laser beam at the focal position (Figure 14(a)) produced a focused spot of 0.51 mm in diameter. In this study, the distance off the focal position ranged between 45 and 180 mm with a defocused spot size of 2.5-9.8 mm. As the position of measurement moved toward around 80 mm below the focus, the power distribution of the laser beam gradually transformed to a Gaussian-like profile. The beam profile with 80 mm off-distance (Figure 14(d)) is compared with an ideal Gaussian distribution in Figure 15. As it can be seen, the laser beam profile measured at 80 mm off-distance under 1875 W laser power was well close to an ideal Gaussian power distribution that produces equal peak laser power density, therefore it was used as a Gaussian laser source in Test 3.

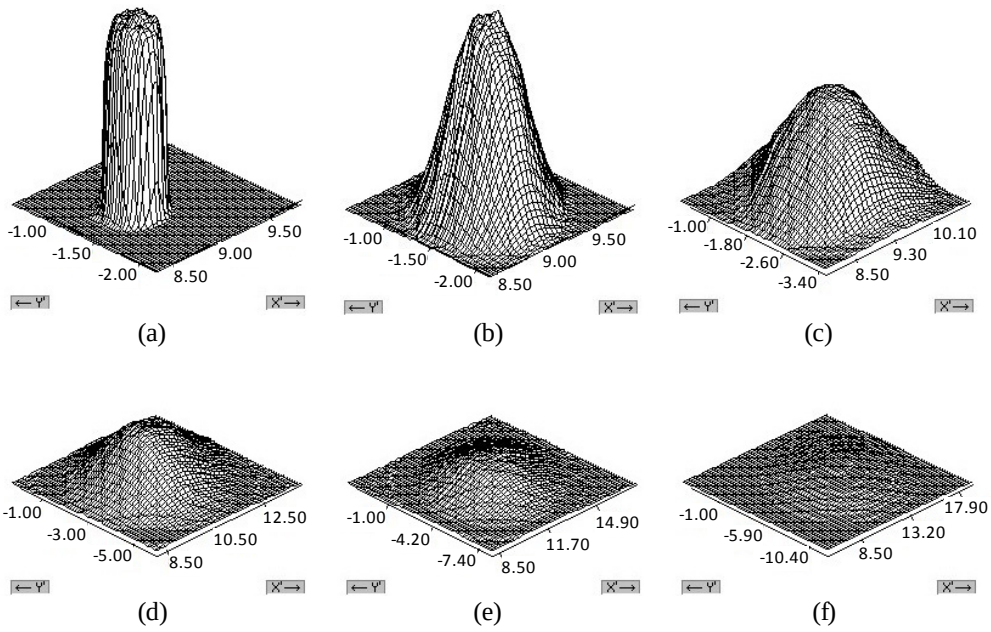

Figure 14. Energy distribution of the laser spot at different distance below the focal position, measured under 2 kW laser power. (a) 0 mm (focus); (b) 20 mm; (c) 45 mm; (d) 80 mm; (e) 120 mm; (f) 180 mm.

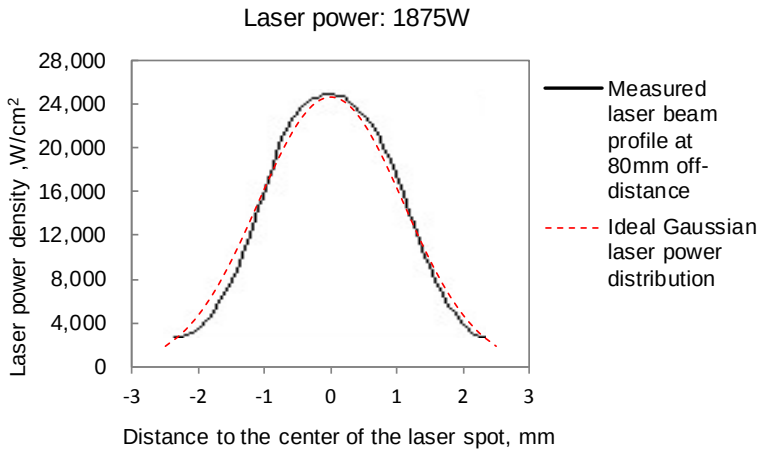

Figure 15. Comparison of the measured laser beam profile at 80 mm off-distance under 1875 W laser power with a calculated ideal Gaussian laser power distribution with equal peak power density.

In Test 4, the laser beam was defocused by a parabolic scanning mirror of 250 mm in the focal length installed in the DC-Scanner connecting to a controller unit. Figure 16(a) shows the laser energy distribution with oscillation frequency of 100 Hz and amplitude of 5.9 mm produced by the DC-scanner. As the oscillation speed was reduced to 0 at the edge of oscillation, in order to avoid surface melting, the output laser power was modulated by programming in the controller unit. As indicated in Figure 17, the output laser power was programmed at 19 positions with equal space across the width of oscillation, producing an approximated sine-wave laser power profile. The peak laser power was 2020 and 3020 W, respectively, and the laser power at both edges of oscillation was 300 W. Since the oscillation speed followed sine wave form as well, the ratio of oscillation speed to output laser power could be regarded as a constant. Figure 16(b) shows a controlled laser beam profile featuring reduced laser power density near the edge of oscillation.

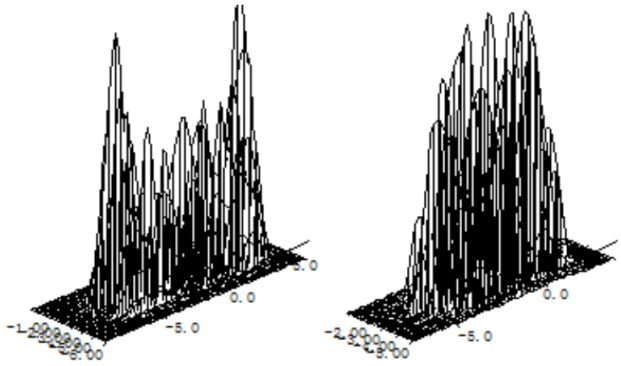

Figure 16. Laser energy distribution produced by DC scanner with oscillation frequency of 100 Hz and amplitude of 5.9 mm, at a distance of 60 mm off the focus. (a) without power control; (b) with power control via the controller unit.

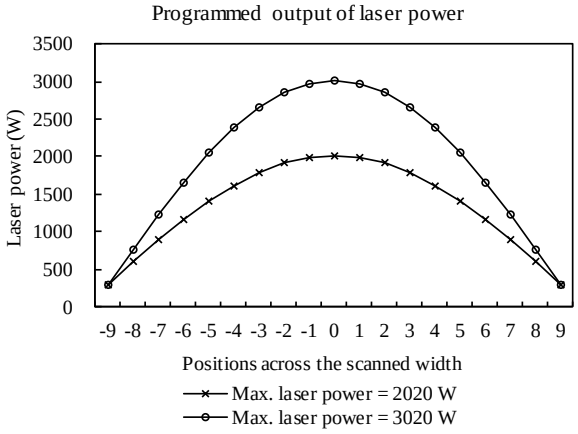

Figure 17. Programmed laser power output via the controller unit of the DC scanner.

4.5 Measurement

The tested samples were cut, ground and polished for microscopic observation and hardness measurement. Material 1-5 were etched with 5% Nital (nitric acid solution in alcohol). Due to the high alloy content of Material 6 and 7, these samples were etched with 10% Nital for longer time in order to obtain distinct images of the microstructures.

The hardness measurements were done at three series of positions on the prepared samples, as indicated in Figure 18. Series 1 was across the whole width of laser irradiated track on the cross-section. Series 2 was along the depth below the center of track. Series 3 was along the center of the irradiated area toward the feeding direction. The starting point was randomly selected. In order to avoid the interference on the indent, sufficient space was kept between the indentation marker and the edge of the workpiece.[79,80] For Test 1, HV5 measurement at positions Series 1 and 2 were done at a depth of about 0.3 mm. For Test 2, HV5 and HV0.01 measurements were done on Series 2 in which the top indentation marker was about 0.3 mm beneath the surface. For Test 4, HV0.1 hardness was measured at Series 1-3 with a depth of 0.1 mm. Measured values of Series 1 and 3 were used to represent the surface hardness.

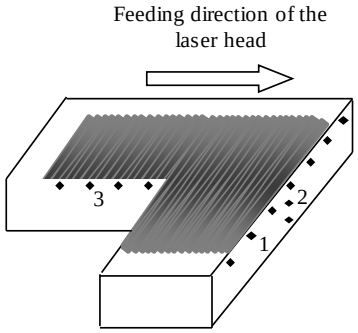

Figure 18. Positions of hardness measurement.

Test 1 used a traditional Vickers Hardness Tester (VHT) with a 5 kg load for conventional hardness (HV5) measurement. Test 2 used a CSM Micro-hardness Tester (MHT) with a 10 g load for microhardness (HV0.01) measurement. HV5 hardness profiles were also measured for comparison. Besides, carbon and alloy content were measured at various local areas of Material 2 and 5 with Energy Dispersive Spectroscopy (EDS) method combined with a scanning electron microscope (SEM). In Test 2, the grain size was determined using the mean grain diameter method.[25] In Test 3, a pyrometer was used to measure the temperature cycles of laser irradiated tracks during the process. The effective work range of the pyrometer was between 488.4°C and around 2000°C. The A_{c1} and A_{c3} depths were determined visually via the microscopic view. Test 4 used a 100 g load for hardness measurement (HV0.1). The hardened depth in Test 1 and Test 2 was defined as the depth where measured macrohardness is reduced to 500 HV below the center of the laser irradiated track. In Test 4, the hardened depth was defined as the depth where measured hardness decreases to 400 HV.

5 A REVIEW OF THE PUBLICATIONS

This chapter summarized the four research papers that constitute the second part of this thesis.

Table 9 The research papers and related research problems.

Research paper	Research problem
Publication 1	The influence of laser power and laser power density on hardening effect of medium-carbon steel and the optimal laser power density affected by different laser power
Publication 2	Microhardness analysis of laser hardened steels with different carbon and alloy content and initial microstructures.
Publication 3	A thermodynamic model that can be used to calculate the temperature cycle, transformation boundary, homogenization time and cooling rate of a wide thin steel plate surface treated with a Gaussian laser beam.
Publication 4	The effect of laser linear oscillation hardening (LLOS) of steel and its comparison with conventional single-track scanning.

5.1 Publication 1

Transformation hardening of medium-carbon steel with a fiber laser: the influence of laser power and laser power density

Publication 1 investigated the effect of laser power density of a fiber laser on surface transformation hardening of two types of medium-carbon steels. An out-of-focus fiber laser beam was used. The test used two medium-carbon steels with similar carbon content and different initial microstructures, including an as-rolled steel consisting of ferrite and pearlite and a quenched and tempered steel composed of tempered martensite. The samples were laser hardened with diverse laser power and laser power density. The optimum power density that produces the maximum hardness was found to be dependent on the laser power. The effect of laser power density on the produced hardness was revealed. The surface hardness, the hardened depth and the required laser power density were compared between the samples. Fiber laser was briefly compared with high power diode laser in hardening medium-carbon steel.

5.2 Publication 2

Laser transformation hardening of carbon steel: the microhardness analysis on microstructural phases

Surface hardening of steel has been mostly studied with conventional hardness measurement which typically uses a load of several kilograms. Yet metallographic analysis of specific phases and microstructures frequently demands local hardness measurement within a small scale such as tens of micrometers. Publication 2 investigated the microhardness and microstructure of different laser hardened steels using a microhardness tester with a 10 g load. The tested samples included rolled steel, quenched and tempered steel, soft annealed alloyed steel and conventionally through-hardened steel. Microhardness measurement (HV0.01) was done in martensite, pearlite, ferrite and cementite structures at different depths below the laser irradiated surface. The microhardness test results were compared with the conventional macrohardness (HV5) values. The effect of grain size of on surface hardness of ferritic-pearlitic steel and pearlitic-cementite steel was examined. In-grain indentation was done to measure the hardness of pearlite and cementite structures. The macrohardness of the base material was found to be close to the microhardness of the softer phase structure. The measured microhardness was about 100-250 HV higher than macrohardness.

5.3 Publication 3

Thermodynamic modelling of the surface treatment of a wide thin steel plate with a Gaussian laser beam

A thermodynamic model was developed in Publication 3 in order to investigate the quasi-steady thermal process of a wide thin steel workpiece irradiated with a moving Gaussian laser beam. Equations were established to calculate the temperature cycle, A_{c1} and A_{c3} boundaries, homogenization time and cooling rate. The equations were numerically solved with an error of less than 10^{-8}. The temperature distributions for diverse thicknesses were compared with that for infinite thickness at various laser traverse speed. The lag of the peak temperature relative to the center of laser beam was found to have an upper limit. The model was verified by experimental results. For AISI 4340 steel, correction coefficients were applied to the model to produce an empirical equation for temperature cycles above 488.4°C.

5.4 Publication 4

Surface hardening of AISI 4340 steel by laser linear oscillation scanning

Publication 4 investigated the surface hardening of AISI 4340 steel by laser linear oscillation hardening (LLOS) using a DC-Scanner. Various frequencies and

amplitudes of oscillation were used with programmed laser power profiles. Equations were derived to calculate the overlapped width of adjacent tracks and the number of scans a local spot in the center of oscillation received during the process. The effect of oscillation frequency on the hardened depth was investigated via microscopic evaluation and hardness measurement. Hardness profiles were measured along the center of the irradiated track toward the feeding direction of laser, across the irradiated width and into the depth below the irradiated surface. The homogeneity of hardness and the hardened depth with different processing parameters were investigated. The hardness profiles were compared with the results obtained from conventional single-track hardening that used a simply defocused laser beam. LLOS was proved to be well suitable for surface hardening featuring a relatively large rectangular area and a considerable hardened depth. In comparison to conventional single-track scanning, LLOS at 40 and 100 Hz produced higher hardness, but the maximum achieved hardened depths were notably limited.

6 CONCLUSIONS AND RECOMMENDATIONS

This study investigated several topics related to the surface hardening of steel using a high power fiber laser. The influences of laser power and laser power density on the surface hardness and hardened depth were investigated. The optimal laser power and laser power density were revealed. The microhardness profiles of laser hardened steels were analyzed and compared with conventional macrohardness measurement. A thermodynamic model was developed to evaluate the thermal process of the surface treatment of a wide thin steel plate using a moving Gaussian laser beam. The model was verified and corrected by experimental results. The effect of laser linear oscillation hardening (LLOS) of steel was investigated and compared with conventional single-track scanning.

The main conclusions obtained from this study are shown as follows.

1. Under each laser power there was an optimum power density which produced the maximum hardness. Increase or decrease from this power density resulted in reduced hardness. With higher laser power, lower power density was required to produce the highest hardness, and meanwhile a larger treated area with high hardness was obtained. This can be explained with the homogenization time. A larger laser spot size may enable longer homogenization time in case the surface was heated above the austenitization temperature, and thus carbon diffusion was improved. This effect was much more remarkable on rolled ferritic-pearlitic steel than on quenched and tempered steel, probably because longer homogenization time benefits more the ferritic-pearlitic steel for carbon diffusion from the carbides to ferrite. Increase of hardened depth could be achieved either by using higher laser power or by reducing the laser spot size. For quenched and tempered steel, surface melting generally reduced much the surface hardness, while slight surface melting in some exceptional cases increased the hardness. Quenched and tempered steel required higher laser power density to achieve the same hardness as rolled steel.

2. For rolled ferritic-pearlitic steels, the grain size significantly affected the homogeneity of martensite and the microhardness. The microhardness of cementite (around 560 HV) and pearlite (around 410 HV) was obtained by in-grain indentation. In the base material of the ferritic-pearlitic and pearlitic-cementite steels, the macrohardness was close to the microhardness of the softer phase structure. This phenomenon could not be concluded in the hardened and partially hardened region, as the grain size of the mixed microstructures was so small that in-grain indentation with 10 g load was nearly impossible. The homogeneity of Cr and Mn contents might significantly affect the macrohardness of tempered martensitic steel. Compared with quenched and tempered steel and soft annealed alloyed steel

with the same carbon content, the rolled steel achieved higher microhardness of martensite on the surface. Compared with the rolled steel, quenched and tempered steel showed similar hardened depth but lower macrohardness on the surface. A possible explanation is that quenched and tempered steels used in the test contained distinctly higher amount of Ni. As an austenite stabilizing element, Ni might have caused larger proportion of retained austenite in the hardened area. The micro- and macrohardness of soft annealed alloyed steel were relatively high on the surface but markedly decreased along the depth, producing a relatively small hardened depth. The base material of soft annealed steel had a similar microhardness to ferrite, indicating that dispersed granular pearlite had little effect on the microhardness. The measured microhardness values were about 100-250 HV higher than the macrohardness. This phenomenon was explained by a model of indentation size effects as well as the dislocation theory.

3. A quasi-steady thermodynamic model was derived to calculate the temperature cycle, the transformation boundary, the homogenization time and the cooling rate of a wide solid plate irradiated by a Gaussian laser beam. The temperature distribution for different thickness was compared with infinite thickness at different laser traverse speed. With increased traverse speed, the influence of thickness on the surface temperature was reduced. The lag of the peak temperature behind the center of the laser beam was increased with the traverse speed, but has a constant upper limit. Higher cooling rate could be achieved on thicker samples, but the difference was reduced at higher laser traverse speed. The model was verified by comparing the calculated A_{c1} and A_{c3} depths and temperature cycles with the experimental data. The calculated A_{c1} and A_{c3} depths were 2.5 to 5 times higher than the measured values. The calculated peak temperature was around 3.5 times of the measured values. The used thermal conductivity (k), which was obtained at 600°C, could have caused this discrepancy. Correcting coefficients were determined by curve fitting using the smoothing method, in which a "smooth" function was constructed to approximate fit the data. A corrected model was obtained for AISI 4340 steel in this study. With these coefficients, compared with the measured data, corrected A_{c1} and A_{c3} depths and peak temperature were within an error of 3% and 4.7% of the measured values, respectively.

4. In laser linear oscillation scanning (LLOS) process, a local position in the center of oscillation might receive up to tens of scans, depending on the laser spot size, oscillation frequency and feeding speed of the laser head. The hardened depth was increased under higher oscillation frequency and correspondingly smaller amplitude of scanning, because higher laser power density was achieved in the reduced irradiated area. Under the feeding speed of 15 mm/s, the individual scans with 10 and 20 Hz could be distinguished in the microscopic view. Along the center of the irradiated track, the hardness

profile with the oscillation frequency of 100 Hz was more homogeneous than with 10, 20 and 40 Hz and was close to single-track scanning. This was probably due to the overlap width of adjacent tracks and the number of scans a spot in center of oscillation experienced, which was linearly dependent on the frequency. With 100 Hz, the calculation indicated that 56 adjacent scans overlapped and the overlap width was 96.7% of the laser spot diameter, meaning that massive tempering might have covered nearly the whole irradiated area and thus resulted in more homogeneous hardness profile than with lower oscillation frequencies. With LLOS, the maximum hardness might be acquired at a few millimeters away from the center of the track, probably because the high oscillation speed in the center resulted in insufficient heating. LLOS produced higher overall hardness on the laser irradiated surface than single-track hardening. LLOS with the oscillation frequency of 40 and 100 Hz produced higher hardness in the hardened layer. LLOS was proved to be suitable for surface hardening in a relatively large rectangular area with considerable hardened depth. Within the hardened depth of 0.6 mm, LLOS at 40 and 100 Hz produced higher hardness than single-track hardening, probably due to higher cooling rate in LLOS. The length of the rectangular area of laser irradiation in LLOS, which was constantly 2.1 mm, was smaller than the diameter of the laser spot in single track hardening, which was 4.1 mm. According to the model for calculating the cooling rate in paper 3, a smaller length of the laser spot along the moving direction can cause higher cooling rate. Yet the maximum achievable hardened depth produced by LLOS was notably limited in comparison with conventional single-track scanning.

5. The future study may extend the present investigation in two main aspects. The thermodynamic model developed in this study can be verified by more steels with more combinations of processing parameters. The study of LLOS can be extended using a scanning head that supports more oscillation frequencies and amplitudes. Empirical formulas can be concluded to estimate the hardened depth with LLOS. The LLOS process may be applied to more steels with different compositions and microstructures of the base material to evaluate its applicability. A model can be developed to study the temperature distribution in the LLOS process with various feeding speed, amplitude and frequency of oscillation. This may assist the investigation on the cooling rate and the evaluation of the tempering effect. Optimized combinations of these parameters may be obtained. The model may also be used to compare LLOS with pulsed and CW rectangular laser beam scanning.

REFERENCES

1. DeMichelis, C. (1970). Laser interaction with solids-a bibliographical review. *J. Quantum Electronics*, QE-6 (10), 630-641.

2. Namba, S., Kim, P. H., Nakayama, S. and Ida, I. (1965). The surface temperature of metals heated with laser. *Japanese Journal of Applied Physics*, 4 (2), 153-154.

3. Speich, G. R. and Szirmae, A. (1969). Formation of austenite from ferrite and ferrite-carbide aggregates. *Trans. AIME*, 245 (5), 1063-1074.

4. Miller, J. E. and Wineman, J. A. (1977). Laser hardening at Saginaw steering gear. *Metal Progress*, 111 (5), 38–43.

5. Goia, F. A. and de Lima, M. S. F. (2011). Surface Hardening of an AISI D6 Cold Work Steel Using a Fiber Laser. *Journal of ASTM International*, 8 (2), Paper ID: JAI103210.

6. Ion, J. C. (2002). Laser transformation hardening. *Surf. Eng.*, 18 (1), 14-31.

7. Ready, J. F. (1997). *Industrial Application of Lasers, 2nd Edition*. Academic Press, London. 599p.

8. Kennedy, E., Byrne G. and Collins, D. N. (2004). A review of the use of high power diode lasers in surface hardening. *Journal of Materials Processing Technology*, 155-156, 1855-1860.

9. Bonss, S., Hannweber, J., Karsunke, U., Kuehn, S., Seifert, M. and Beyer, E. (2012). Laser heat treatment with latest system components. *Proc. of SPIE on 'High Power Laser Materials Processing: Lasers, Beam Delivery, Diagnostics, and Applications'*, (January 21-26), San Francisco, USA, Paper 82390I.

10. Pantsar H. (2005). Models for Diode Laser Transformation Hardening of Steels: [D]. Lappeenranta: Lappeenranta University of Technology.

11. Müller, H-R., Kirchhof, J., Reichel V. and Unger, S. (2006). Fibers for high-power lasers and amplifiers. *Comptes Rendus Physique*, 7 (2), 154-162.

12. Canning, J. (2006). Fiber lasers and related technologies. *Optics and Lasers in Engineering*, 44 (1), 647-676.

13. Limpert, J., Rösera, F., Schreibera, T., Manek-Hönningerb, I., Salinb, F. and Tünnermann A. (2006). Ultrafast high power fiber laser systems. *Comptes Ren-dus Physique*, 7 (2), 187-197.

14. de Lima, M. S. F., Goia, F. A., Riva, R. and Santo, A. M. E. (2007). Laser surface remelting and hardening of an automotive shaft using a high-power fiber laser. *Materials Research*, 10 (4), 461-467.

15. Goia, F. A. and de Lima, M. S. F. (2011). Surface hardening of an AISI D6 cold work steel using a fiber laser. *Journal of ASTM International*, 8 (9), 488-496.

16. Tabor, D. (1986). Indentation Hardness and Its Measurement: Some Cautionary Comments. *Microindentation Techniques in Materials Science and Engineering (ASTM STP 889)*, Blau, P. J. and Lawn, B. R., eds. American Society for Testing and Materials, Philadelphia, 129-159.

17. Yan, M. F. and Liu, Z. R. (2001). Study on microstructure and microhardness in surface layer of 20CrMnTi steel carburised at 880°C with and without RE. *Materials Chemistry and Physics*, 72 (1), 97-100.

18. Mo, D., Hu, Z., Chen, S., Wang, C. and He, G. (2009). Microstructure and Hardness of T250 Maraging Steel in Heat Affected Zone. *Journal of Iron and Steel Research (International)*, 16 (1), 87-91.

19. Tanasawa, I. and Lior, N. eds. (1992). *Heat and Mass Transfer in Materials Processing*. Hemisphere, Washington, DC.

20. Yao, C. W., Huang, J., Zhang, P. L., Wu, Y. X. and Xu, B. S. (2009). Tempering softening of overlapping zones during multi-track laser quenching for carbon steel and alloy steel. *Transactions of Materials and Heat Treatment*, 30 (5), 131-135.

21. Campana, G., Ascari, A. and Tani G. (2009). A Method for Laser Heat Treatment Efficiency Evaluation in Multi-Track Surface Hardening. *Proc. ASME 2009 Int. Conf. on 'Manufacturing Science and Engineering'*, (October 4-7), West Lafayette, USA, Paper 95.

22. Steen, W. M. (2003). *Laser Material Processing, 3rd Edition*. Springer-Verlag, London. 408p.

23. Davis, J. R. (2002). *Surface Hardening of Steels: Understanding the Basics*, ASM International, Materials Park (OH). 364 p.

24. Lakhkar, R. S., Shin, Y. C. and Krane, M. J. (2007). Predictive modelling of multi-track laser hardening of AISI 4140 steel, *Materials Science and Engineering A*, 480 (1-2), 209-217.

25. Thelning, K-E. (1984). *Steel and Its Heat Treatment, 2nd Edition*.

Butterworth-Heinemann, London. 704p.

26. Brooks, C. R. (1992). *Principles of the Austenitization of Steels*. Springer, London. 232p.

27. Dossett, J. L. and Boyer, H. E. (2006). *Practical Heat Treating, 2nd Edition*. ASM International, Metals Park (OH). 296p.

28. Bhadeshia, H. and Honeycombe, R. (2006). *Steels: Microstructure and Properties, 3rd Edition*. Butterworth-Heinemann, Oxford. 360p.

29. Kou, S. (2002). *Welding Metallurgy, 2nd Edition*. Wiley-Interscience, Hoboken. 480p.

30. Porter, D. A., Easterling, K. E. (1992). *Phase Transformations in Metals and Alloys, 2nd Edition*. CRC Press, London. 528p.

31. Sverdlin, A. V. and Ness, A. R. *Steel Heat Treatment Handbook (edited by Totten, G. E.), 2nd Edition*. Ch. 3, 143-144. (2006). CRC Press, New York.

32. Grum, J. *Steel Heat Treatment: Equipment and Process Design (edited by Totten, G. E.), 2nd Edition*. Ch. 6, 443-447. (2006). CRC Press, New York.

33. Ion, J. C., Vihinen, J., Salminen, A. And Kujanpää, V. (2000). Task 1 Report: Laser transformation hardening, baseline data. *Intelligent Laser Surface Engineering (Project 49808), Academy of Finland*. 87p.

34. Sverdlin, A. V. and Ness, A. R. *Steel Heat Treatment Handbook (edited by Totten, G. E.), 2nd Edition*. Ch. 4, 166-211. (2006). CRC Press, New York.

35. Llewellyn, D. (1998). *Steels: Metallurgy and Applications, 3rd Edition*. Butterworth-Heinemann, Oxford. 400p.

36. Shiue, R. K. and Chen, C. (1991). Microstructural observations of the laser-hardened 1045 steel. *Scr. Metall. Mater.*, 25 (8), 1889-1894.

37. Bergström, D. (2008). The Absorption of Laser Light by Rough Metal Surfaces: [D]. Luleå: Luleå University of Technology.

38. Ang, L. K., Lau, Y. Y., Gilgenbach, R. M. and Spindler, H. L. (1997). Analysis of laser absorption on a rough metal surface. *Applied Physics Letters*, 70 (6), 696-698.

39. Grum, J. (2007). Comparison of different techniques of laser surface hardening.

Journal of Achievements in Materials and Manufacturing Engineering, 24 (1), 17-25.

40. Na, S. J. and Yang, Y. S. (1987). Prediction of laser surface hardening zone by using the finite difference method. *Proc. of the Int. Conf. on 'Laser Advanced Materials Processing-Science and Applications (LAMP '87)'*, (May 21-23), Osaka, Japan, Paper 5A02.

41. Bloehs, W., Grünenwald, B., Dausinger, F. and Hügel H. (1996). Recent progress in laser surface treatment: II. Adopted processing for high efficiency and quality. *Journal of Laser Applications*, 8 (2), 65-77.

42. Baumann, M., Krause, V., Bergweiler, G., Flaischerowitz, M. and Banik, J. (2012). Local heat treatment of high strength steels with zoom-optics and 10kW-diode laser. *Proc. of SPIE on 'High Power Laser Materials Processing: Lasers, Beam Delivery, Diagnostics, and Applications'*, (January 21-26), San Francisco, USA, Paper 82390J.

43. Laskin, A. and Laskin, V. (2012). Applying of refractive beam shapers of circular symmetry to generate non-circular shapes of homogenized laser beams. *Proc. of SPIE on 'Laser Resonators and Beam Control XIII'*, (January 22-25), San Francisco, USA, Paper 79130J.

44. Parker, K. (2012). Smart optics improve surface treatment. *Industrial Laser Solutions*, 27 (4), 9-10.

45. Laser system technology brochure and List of optics. [In NUTECH GmbH www-pages]. [retrieved 26 November 2012]. From: http://www.nutech.de/cms/files/laserstrahlwerkzeuge_2008__1_.pdf

46. Bradley, J. R. (1988). A simplified correlation between laser processing parameters and hardened depth in steels. *Journal of Physics D: Applied Physics*, 21 (5), 834-837.

47. Kach, A. (2011). Efficient laser hardening at an auto manufacturer. *Industrial Laser Solutions*, 26 (2), 2-4.

48. Hardening of torsion springs. [In Rofin-Sinar Laser GmbH www-pages]. [retrieved 26 November 2012]. From: http://www.rofin.com/en/applications/surface_treatment/laser_hardening/

49. Shibata, K. (1987). Laser applications at Nissan. *Proc. Conf. Applications of Laser Processing in Automobile Fabrication and Related Industries*, (December 3-4), The Welding Institute, Abington,

50. McKeown, N., Steen, W. M. and McCartney, D. G. (1990). Laser transformation hardening of engine valve steels. *In: Proceedings of the Laser Materials Processing Conference (ICALEO '90)*, Ream, S. L., Dausinger, F. and Fujioka, T. eds. Laser Institute of America, Orlando.

51. Bellis, J. (1980). Transformation hardening metals. *In: Lasers - Operation, Equipment, Application and Design*, Saunders, R., Bellis, J. and Coherent, inc. eds. 124-135. McGraw-Hill, New York.

52. Seaman, F. D. (1986). Laser heat-treating. *In: The Industrial Laser Annual Handbook*, Belforte, D. and Levitt, M. eds. 147-157. PennWell Books, Tulsa.

53. Gutu, I., Mihailescu, I. N., Comaniciu, N., Draganescu, V., Denghel, N. and Mehlmann, A. (1983). Heat Treatment of Gears in Oil Pumping Units Reductor. Proc. Conf. Industrial Applications of Laser Technology, Faga, W. F. eds. 393-397. SPIE, Bellingham.

54. Gregory, R. D. (1995). 'Toughening up' capstan surfaces. *Wire Technology International*, 23 (6) 67-68.

55. Gregory, R. D. (1996). Job shop laser heat treating. *Industrial Laser Review*, 11 (8), 13-15.

56. Brenner, B. and Reitzenstein, W. (1996). Laser hardening of turbine blades. *Industrial Laser Review*, 11 (4). 17-20.

57. Krauss, G. (1990). *Steels: heat treatment and processing principles*. ASM International, Metals Park (OH). 497p.

58. Rozniakowska, M. and Yevtushenko, A. A. (2005). Influence of laser pulse shape both on temperature profile and hardened layer depth. *Heat and Mass Transfer/Waerme- und Stoffuebertragung*, 42 (1), 64-70.

59. Ma, X. H. (2004). A new mechanism for condensation heat transfer enhancement: effect of the surface free energy difference of condensate and solid surface. *Journal of Enhanced Heat Transfer*, 11 (4), 257-265.

60. Soskind, Y. G. (2009). Diode laser beam shaping and propagation characteristics. *Proceedings of The International Society for Optical Engineering (SPIE)*, (January 26-28),. San Jose, USA.

61. Kim, J., Lee, M., Lee, S. and Kang, W. (2009). Laser transformation hardening on rod-shaped carbon steel by Gaussian beam. *Transactions of Nonferrous Metals Society of China (English Edition)*, 19 (4), 941-945.

62. Cherezova, T. Y., Chesnokov, S. S., Kaptsov, L. N. and Kudryashov, A. V. (1998). Super-Gaussian laser intensity output formation by means of adaptive optics. *Optics Communications*, 155 (1-3), 99-106.

63. Rykalin, N. N. (1957). *Berechnung der Wärmevorgänge beim Schweißen*. VEB Verlag Technik, Berlin. 326p.

64. Cline, H. E. and Anthony, T. R. (1977). Heat treating and melting material with a scanning laser or electron beam. *J. Appl. Phys.*, 48 (9), 3895-3900.

65. Manca, O., Morrone, B. and Naso, V. (1995). Quasi-steady-state three-dimensional temperature distribution induced by a moving circular Gaussian heat source in a finite depth solid. *International Journal of Heat and Mass Transfer*, 38 (7), 1305-1315.

66. Carslaw, H. S. and Jaeger, J. C. (1986). *Conduction of heat in Solids, 2nd Edition*. Oxford University Press, Oxford. 520p.

67. Eagar, T. W. and Tsai, N. S. (1983). Temperature fields produced by traveling distributed heat sources. *Welding Research Supplement*, 62 (12), 346-355.

68. Borgnakke, C. and Sonnta, R. E. (2008). *Fundamentals of Thermodynamics, 7th Edition*. Wiley, Danvers. 912p.

69. Haberman, R. (2003). *Applied Partial Differential Equations, 4th Edition*. Prentice Hall, Upper Saddle River. 769p.

70. Beck, J. V., Cole, K. D., Haji-Sheikh, A. and Litkouhi, B. (1992). *Heat Conduction Using Green's Functions*. CRC Press, London. 552p.

71. Kogelnik, H. and Li, T. (1966). Laser beams and resonators, *Applied Optics*, 5 (10), 1550-1567.

72. IPG Laser GmbH. (2006). *YLR-5000-S customized specification, rev1.1*. 14p.

73. Precitec Group: YW50 Welding Head. [In Precitec Group www-pages], [retrieved June 25, 2012]. From http://www.precitec.com/laser-welding/laser-welding-head-yw50.html

74. Arlt, A. G. (2009). *User's Manual: ILV DC-Scanner*. ILV GmbH, Schwalbach. 29p.

75. Wegst, C. W. (2007). *The Key to Steel (Stahschlussel), 21st Edition*. French & European Pubns Inc, New York. 720p.

76. Nayar, A. (2001). *The Steel Handbook*. Tata McGraw-Hill Education, New Delhi. 800p.

77. Bryson, W. E. (2005). *Heat Treatment, Selection, and Application of Tool Steels, 2nd Edition*. Hanser Gardner Publications, Cincinnati. 239p.

78. Pantsar, H. and Kujanpää, V. (2004). Diode laser beam absorption in laser transformation hardening of low alloy steel. *Journal of Laser Applications*, 16 (3), 147-153.

79. International Organization for Standardization. Metallic materials - Vickers hardness test - Part 1: Test method. *ISO 6507-1:2005*.

80. ASTM International. Standard Test Method for Knoop and Vickers Hardness of Materials. *ASTM E384-11e1: 2011*.

PART II: THE PUBLICATIONS

PUBLICATION 1

Qiu, F. and Kujanpää, V. (2011)

TRANSFORMATION HARDENING OF MEDIUM-CARBON STEEL WITH A FIBER LASER: THE INFLUENCE OF LASER POWER AND LASER POWER DENSITY

The paper has been published in
Mechanika, **17** (3), 318-323
DOI: 10.5755/j01.mech.17.3.510

ISSN 1392 - 1207. MECHANIKA. 2011. 17(3): 318-323

Transformation hardening of medium-carbon steel with a fiber laser: the influence of laser power and laser power density

F. Qiu*, V. Kujanpää**
**Laser Processing Laboratory, LUT Metals, Lappeenranta University of Technology, Tuotantokatu 2, 53850 Lappeenranta, Finland, E-mail: feng.qiu@lut.fi*
***Laser Processing Laboratory, LUT Metals, Lappeenranta University of Technology, Tuotantokatu 2, 53850 Lappeenranta, Finland, E-mail: veli.kujanpaa@lut.fi*

1. Introduction

Laser surface treatment is a process of altering the metallurgical and mechanical properties of the material surface with laser irradiation. It is mostly used to produce hard, wear-resistant regions on the workpiece while retaining the bulk material unaffected [1-3]. A defocused laser beam is usually used to heat up the material surface above its austenitization temperature, allowing formation of austenite.

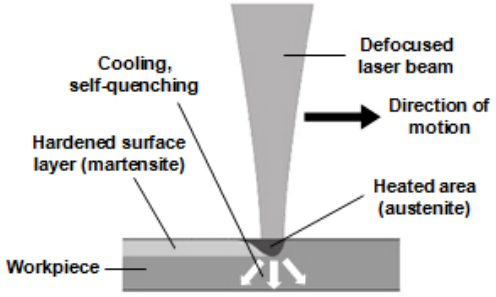

Fig. 1 Basic principle of laser transformation hardening

The base material surrounding the laser irradiated area acts as a heat sink, causing quick self-quenching and phase transformation to martensite [1, 2]. This process is illustrated in Fig. 1.

In recent years, fiber laser systems have been quickly developed for advanced processes [4-7]. Compared with Nd:YAG lasers which are used for industrial purposes, fiber lasers feature simplicity, high electrical-to-optical efficiency, high reliability and relatively low cost of operation [8, 9]. Fiber laser is expected to be suitable for surface hardening of carbon steels, because the wavelength of radiation produced by laser diodes can be efficiently absorbed by iron-based materials [10]. Although laser transformation hardening is a well-known process, information about laser hardening with fiber laser is basically unavailable.

This study focuses on how the laser power and power density of a fiber laser affect laser hardening of medium-carbon steel samples in the hardness profile across the irradiated track, along the depth below the treated surface and in microstructures. Experimental results are also compared with a previous study by high power diode laser hardening.

2. Experimental procedures

This study uses a work cell containing a CNC XY table and a YLR-5000-S fiber laser equipment which produces a laser beam with a wavelength of 1070-1080 nm and a maximum nominal output power of 5 kW. No shielding gas is used.

The hardening tests are done on two types of medium carbon steels with the same carbon content and different initial microstructures and alloying contents shown in Table 1. Imamic (X15) steel is an as-rolled high-silicon steel featuring higher fatigue strength than conventional microalloy steels. The initial microstructure contains ferrite and pearlite. Uddeholm Impax Supreme (AC16) is a pre-hardened mould steel with high contents of chromium, nickel and molybdenum, in which tempered martensite is the basic initial composite due to quenching and tempering treatment. Comparison of X15 and AC16 samples redounds to reveal how laser power density affects the hardening of medium-carbon steels with various initial microstructures and alloying contents. The surface roughness of all samples, R_a, is about 2.5 µm.

Table 1

Sample used in the hardening test (compositions in weight percentage)

Code	Trademark	Delivered Condition	Initial HV5	Compositions (wt. %)							
				C	Si	Mn	Cr	Ni	Mo	V	Cu
X15	Imamic	As rolled	289	0.375	1.319	0.983	0.163	0.111	0.020	0.110	0.243
AC16	Uddeholm Impax Supreme	Q&T	336	0.373	0.366	1.470	1.860	1.172	0.201	0.006	0.181

The laser power P and the laser power density I_p used in this study are indicated in Table 2. The laser spot size R_s is changed by altering the distance off the focus z and thus I_p is changed. The experiment uses a focusing lens with the focal length of 150 mm. An output fiber core diameter of 150 µm in the fiber laser is used for the tests on X15 samples. For AC16 samples, an output fiber core diameter of 200 µm is used. The angle between the optical

axis and the surface is 90 degrees. All the tests are done with a constant traverse rate of 8.0 mm/s. The samples are air-cooled after the process.

For X15 steel, the hardened depth is defined as the distance below the sample's surface where martensite content drops to 50 wt.% of the local microstructures. For AC 16 samples, the hardened depth is defined as the depth where the hardness value reduces to 500 HV.

Table 2

Laser power and laser power density used in the experiments

Test no.	Laser power P, W	Laser power density, I_p, W/cm^2/R_s, Laser spot diameter, mm			
		A	B	C	D
X15_1	955	7224/4.1	8282/3.8	9590/3.6	11231/3.3
X15_2	1423	7496/4.9	8397/4.6	9471/4.4	10765/4.1
X15_3	1900	6145/6.3	6714/6.0	7365/5.7	8117/5.5
X15_4	2840	5065/8.4	5786/7.9	6672/7.4	7779/6.8
X15_5	3788	5012/9.8	5618/9.3	6341/8.7	7212/8.2
AC16_1	944	10955/3.3	12977/3.0	15607/2.8	19112/2.5
AC16_2	1409	12092/3.9	13983/3.6	16351/3.3	*19369/3.0
AC16_3	1883	12425/4.4	14110/4.1	*16159/3.9	*18687/3.6
AC16_4	2816	11952/5.5	13230/5.2	*14724/4.9	*16485/4.7
AC16_5	3750	11083/6.6	12061/6.3	*13174/6.0	*14448/5.7

* Melting is observed on the surface of the irradiated track

3. Results and discussion

3.1. Ferritic-pearlitic steel X15

Fig. 2 shows the surface hardness of X15 workpiece produced by different laser power levels and laser power densities. Under each laser power there is an optimal laser power density which produces the peak hardness. Increase or decrease of laser power density from this optimal point reduces the surface hardness. The peak of the curve shifts to the left as the laser power increases and thus indicates that lower power density is required to produce high hardness with more laser power input. Fig. 3 indicates under each laser power level the optimal laser spot size and the corresponding area that produce the maximum hardness. The optimal spot size is approximately of linear dependence on the laser power, meaning that increase of laser power can significantly increase the hardenable area on the workpiece. The largest measured HV5 value (781) is achieved with the laser power density of 8397 W/cm^2 under 1423 W laser power.

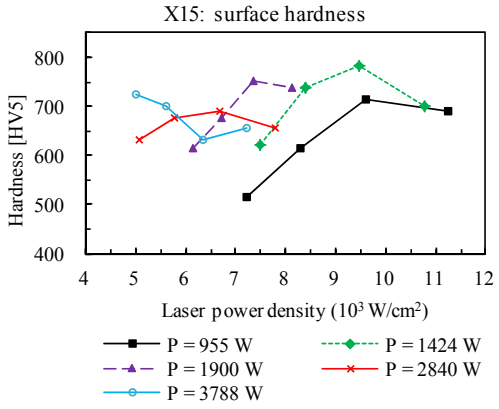

Fig. 2 Surface hardness of X15 samples under various laser power and laser power density

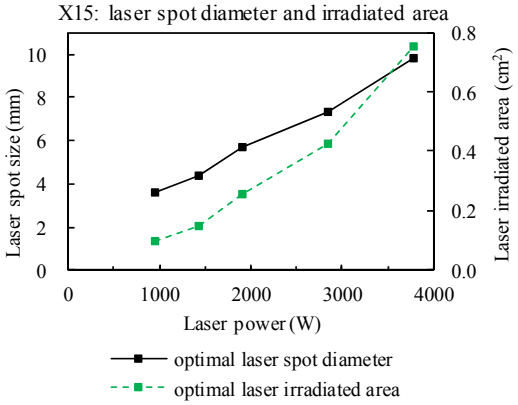

Fig. 3 Optimal laser spot size and laser irradiated area of X15 workpiece under each laser power

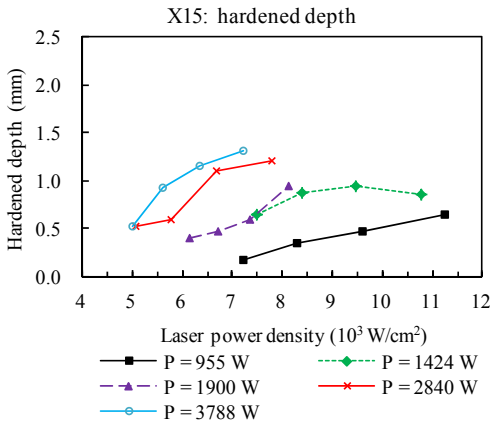

Fig. 4 Hardened depth of X15 samples under various laser power and laser power density

As shown in Fig. 4, increasing the laser power is the basic method of obtaining a deeper hardened layer. However, Fig. 4 also indicates that larger hardened depth can as well be acquired with higher laser power density while retaining the same laser power. This can be done by using a smaller laser spot. The maximum hardened depth of approximately 1.32 mm is produced with 7212 W/cm^2 laser power density under 3788 W laser power.

These can be explained with the thermal cycle during the laser irradiation. As higher laser power is used, the laser spot size is enlarged by increasing the distance off the focus. As the traverse rate remains constant, the magnified laser irradiated area causes a longer thermal cycle in case that appropriate laser power density is applied. The laser power density required to achieve optimal hardening results is thus reduced. Moreover, as Fig. 2 shows, excessive laser power density lowers the cooling rate and thus decreases the produced surface hardness.

Fig. 5 shows an example which compares the effects of 7496 W/cm^2 and 8397 W/cm^2 power density under 1423 W laser power. It indicates that increase of power density from 7496 W/cm^2 to 8397 W/cm^2 facilitates the homogenization of the irradiated area and produces a more homogenous layer of martensite. When the surface of the sample is heated up above its austenitization temperature A_{c1}, the initial crystal structures containing ferrite and pearlite starts to transform to austenite. Carbon diffuses from carbides to ferrite and homogenizes the austenitized area. The hardening effect is determined by the extent of homogenization which relies on the duration the temperature is above A_{c1} and the cooling rate. As all the tests in this study are done with a constant traverse rate, the laser power density is the primary parameter that affect the thermal cycle.

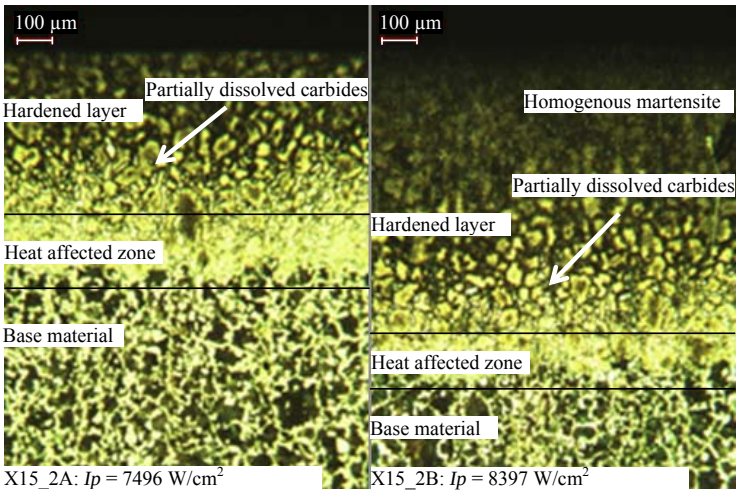

Fig. 5 Microscopic view of cross sections of X15 samples hardened with (a) 7496 W/cm^2 and (b) 8397 W/cm^2 laser power density under 1423 W laser power

3.2. Quenched and tempered steel AC16

Fig. 6 shows the surface hardness obtained on AC16 samples with various laser power and laser power density. Similar to Fig. 2, with each laser power there is a laser power density producing the maximum hardness. Except for 944 W results, increase of laser power causes the optimal power density to shift leftward and accordingly reduces the laser power density required to produce high

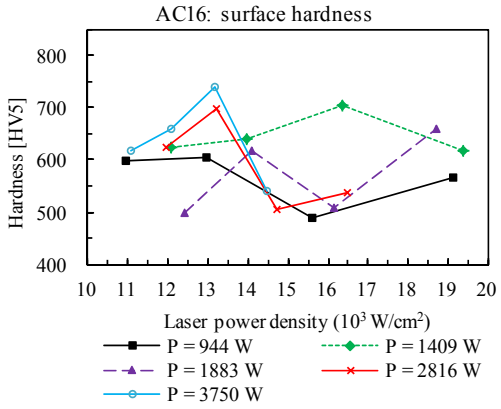

Fig. 6 Surface hardness of AC16 samples under various laser power and laser power density

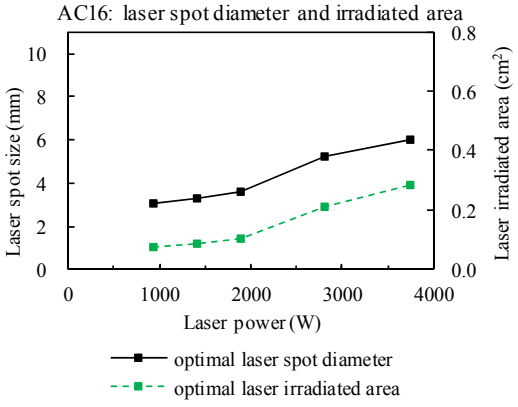

Fig. 7 Optimal laser spot size and laser irradiated area of AC16 workpiece under each laser power

hardness. Fig. 7 shows the dependence of the optimal laser spot size and the irradiated area on laser power. In contrastto Fig. 3, the increase of laser power does not markedly magnify the optimal hardening area on the AC16 workpiece. The hardened depths of AC16 samples are presented in Fig. 8. Increase of laser power results in deeper har dened layer. Increase of laser power density via reducing the laser spot size can produce larger hardened depth as well. The maximum hardness (781) and the maximum hardened depth (2.15 mm) are produced with 3750 W laser power and 13174 W/cm^2 laser power density.

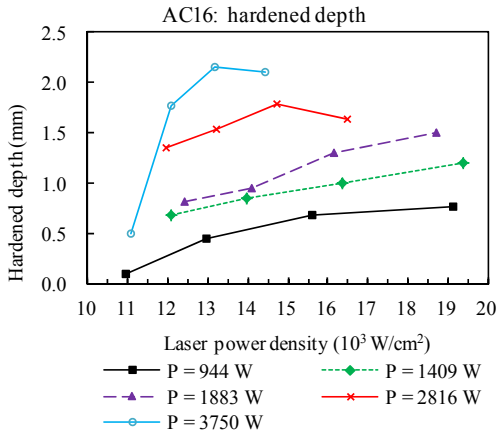

Fig. 8 Hardened depth of X15 samples under various laser power and laser power density

3.2.1. Surface melting

Surface melting occurs on some of the tests denoted in Table 2. Fig. 6 and Fig. 8 exhibit that surface melting mostly causes dramatic decrease in the surface hardness. However, the results denote that surface melting in some cases may benefit the hardening process. Fig. 9 compares the micrographs of melted and unmelted AC16 samples hardened with 3750 W laser power. Melting occurs on sample 5C and 5D. As indicated in Fig. 6, compared with sample 5B, 5C produces higher surface hardness while 5D shows the opposite. Melting that occurs on 5C does not reduce the surface hardness and may even benefit the hardening result. The thin melted layer shown in Fig. 9 may avail the homogenization of carbon and other elements and is supposed to experience a sufficiently high cooling rate to form homogenous martensite on the sample's surface. In contrast, a much thicker melted layer is produced on sample 5D, which can markedly lower the cooling rate, anneal the sample's surface and hence dramatically reduce the surface hardness.

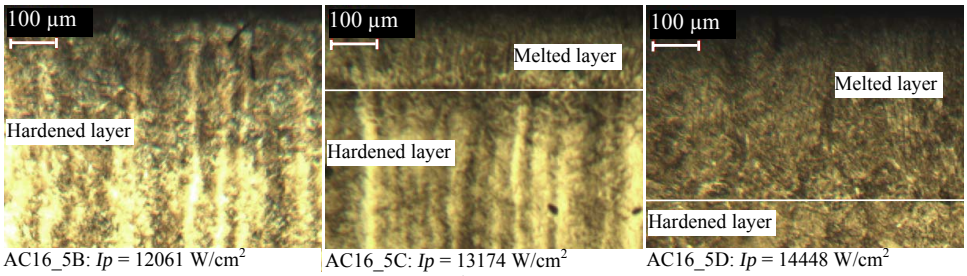

AC16_5B: *Ip* = 12061 W/cm^2 a | AC16_5C: *Ip* = 13174 W/cm^2 b | AC16_5D: *Ip* = 14448 W/cm^2 c

Fig. 9 A microscopic view of the cross sections of AC16 samples hardened with (a) 12061 W/cm^2, (b) 13174 W/cm^2 and (c) 14448 W/cm^2 laser power density under 3750 W laser power

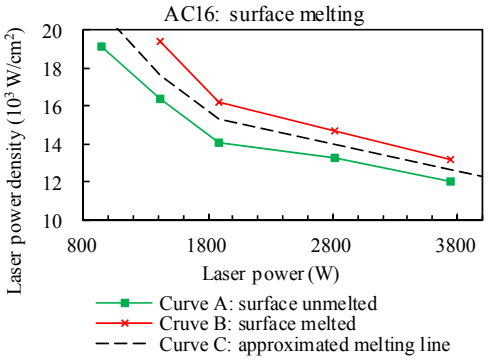

Fig. 10 Surface melting in AC16 tests under various laser power and laser power density

As shown in Fig. 10, curve A and curve B respectively represent non-surface-melting and surface-melting results. A curve C is approximated from experimental data to exhibit the melting condition. Combinations of laser power and laser power density below curve C result in normal surface hardening and above curve C the risk of surface melting should be taken into consideration.

3.3. Comparison of ferritic-pearlitic steel with quenched and tempered steel

The highest surface hardness values produced on X15 and AC16 samples in the test are both about 780 (HV5). This is basically due to the equal carbon content as shown in Table 1. The carbon content determines the hardness of martensite that can be produced on the material surface and thus the maximum surface hardness obtained on X15 and AC16 samples are close.

Comparing Fig. 4 and Fig. 8, AC16 samples require higher laser power density to achieve the same hardness level as X15. The hardened depth acquired in AC16 samples is relatively high due to the alloy content of Mn, Cr and Ni. Alloy elements decrease the transformation rate of austenite to ferrite and ferrite carbides and make it possible to form martensite with lower cooling rates [11]. This is beneficial to produce a deeper hardened layer.

3.4. Comparison of fiber laser hardening with diode laser hardening

The same samples of the ferritic-pearlitic steel X15 and quenched and tempered steel AC16 were tested in a previous study by Pantsar using a high power diode laser which delivered radiation at wavelengths of 800±10 nm and 940±10 nm [12]. Due to efficient energy absorption by iron-based materials, high power diode laser is considered to be more suitable for hardening steels than other laser types [2]. The tests results are compared with fiber laser hardening in this study as shown in Table 3.

The comparison shows some advantages over high power diode laser. The high power diode laser can produce approximately the same surface hardness in a larger irradiated area with lower laser power. The hardened depth, on the other hand, cannot be compared since the test data with high power diode laser is not available.

Fiber laser is capable to produce equivalent or even higher surface hardness in hardening of medium-carbon steels. It can be used as an effective tool to achieve both high surface hardness and considerable hardened depth for surface hardening but requires relatively high laser power density which also means smaller irradiated area.

The comparison is however incomplete and inconclusive, since different optics are used and create different laser beam profiles which probably have significant influence on the hardening results. Besides, previous study suggested that change of traverse rate has large effect on the hardening effects [13]. Therefore the optimization of the traverse rate in combination with laser power, laser power density and irradiate area is well worth further investigation.

Table 3

Comparison of fiber laser hardening of steels X15 and AC16 with diode laser hardening in a previous study [12]

Material	Surf. roughness, R_a, μm	Laser	Traverse rate, mm/s	Laser power, W	Irradiated area, cm^2	Laser power density, W/cm^2	HV5	Hardened depth, mm
X15	0.2-0.4	diode laser	10.5	1170	0.65 (rectangle)	1800	743	NA
X15	2.5	fiber laser	8.0	1423	0.17 (circular)	8397	781	1.5
AC16	0.2-0.4	diode laser	10.5	1170	0.65 (rectangle)	1800	772	NA
AC16	2.5	fiber laser	8.0	3750	0.28 (circular)	13174	781	2.25

4. Conclusions

This study investigates how the laser power density of a fiber laser affects the surface transformation hardening of medium-carbon steels. The tests use two materials with different initial microstructures, including X15 which is composed of ferrite and pearlite and AC16 that contains tempered martensite.

The tests on X15 and AC16 samples indicate that under each laser power there is an optimum power density what can produce the maximum hardness. With higher laser power, lower power density is required to produce high hardness. This also means that increase of laser power can markedly enlarge the area that can be hardened. This shows much higher effect on X15 than on AC16. Increase of hardened depth can be either achieved by using higher laser power or by reducing the laser spot size while retaining the laser power unchanged.

Surface melting generally reduces much the surface hardness. But slight surface melting in some exceptional cases may improve the hardening effect.

AC16 requires higher laser power density to achieve the same hardness as X15. Due to the equivalent carbon contents of X15 and AC16, the maximum surface hardness (HV5) obtained on the two materials are both around 781. The hardened depth acquired in AC16 samples is relatively high due to the alloy contents of Mn, Cr and Ni.

For hardening of medium carbon steels, fiber laser may be capable to produce equivalent surface hardness in a smaller circular area, requiring markedly higher laser power density in comparison with high power diode laser. Fiber laser is a potential tool to produce high surface hardness and high hardened depth for medium-carbon steels. Further study is required in optimization with appropriate optics and/or scanning parameters, e.g. the traverse rate.

References

1. **Steen, W.M.** 2003. Laser Material Processing, 3rd ed. London: Springer-Verlag. 408p.
2. **Ion, J.C.** 2002. Laser transformation hardening, Surface Engineering 1: 14-31.
3. **Jonušas, R.**; **Kalpokas, J.**; **Petrikas, R.**, **Žunda, A.** 2004. Investigation of laser surface treatment effect on coating adhesion, Mechanika 5(49): 65-71.
4. **Limpert, J.**; **Rösera, F.**; **Schreibera, T.**; **Manek-Hönningerb, I.**; **Salinb, F.**; **Tünnermann ,A.** 2006. Ultrafast high power fiber laser systems, Comptes Rendus Physique 7(2): 187-197.
5. **Baumeister, M.**; **Dickmann, K.**; **Hoult, T.** 2006. Fiber laser micro-cutting of stainless steel sheets, Applied Physics A: Materials Science & Processing 85: 121-124.
6. **Kawahito, Y.**; **Terajima, T.**; **Kimura, H.**; **Kuroda, T.**; **Nakata, K.**; **Katayama, S.**; **Inoue, A.** 2008. High-power fiber laser welding and its application to metallic glass $Zr_{55}Al_{10}Ni_5Cu_{30}$, Materials Science and Engineering: B 148(1-3): 105-109.
7. **Kah, P.**; **Salminen, A.**; **Martikainen, J.** 2010. The effect of the relative location of laser beam with arc in different hybrid welding processes, Mechanika 3(83): 68-74.
8. **Canning, J.** 2006. Fiber lasers and related technologies, Optics and Lasers in Engineering 44: 647-676.
9. **Aouici, H.**; **Yallese, M.A.**; **Fnides, B.**; **Mabrouki, T.**

2010. Machinability investigation in hard turning of AISI H11 hot work steel with CBN tool, Mechanika 6(86): 71-77.
10. **Ready, J.F.** 1997. Industrial Application of Lasers, 2nd ed. London: Academic Press. 599p.
11. Edited by **Ready, J.F.**; **Farson, D.F.**; **Feeleyed, T.** 2001. LIA Handbook of Laser Materials Processing. Pineville: Magnolia Publishing Inc. 715p.
12. **Pantsar, H.** 2005. Models for diode laser transformation hardening of steels: [D]. Lappeenranta: Lappeenranta University of Technology. 134p.
13. **Arata, Y.**, **Inoue, K.**, **Maruo, H.**, **Miyamoto, I.** 1986. Application of laser for material processing - Heat flow in laser hardening. Plasma, Electron & Laser Beam Technology, Development and Use in Materials Processing. American Society for Metals: 550-567.

F. Qiu, V. Kujanpaa

VIDUTINIO ANGLINGUMO PLIENŲ KIETUMO KEITIMAS PLUOŠTINIAIS LAZERIAIS: LAZERIO GALIOS TANKIO ĮTAKA

R e z i u m ė

Straipsnyje tiriama pluoštinio lazerio galios tankio įtaka dviejų vidutinio anglingumo plienų paviršiaus kietumo kitimui. Išfokusuotas lazerio spindulys, gautas naudojant pluoštinių lazerių sistemą, panaudotas bandinio paviršiui apšvitinti. Bandymams panaudoti du vidutinio anglingumo skirtingos pradinės mikrostruktūros plienai: X15 turintis ferito ir perlito, ir AC16, sudarytas iš atleisto martensito. Plieno X15 bandymai parodė, kad bet kokios galios lazeriui būtinas tam tikras optimalus galios tankis, leidžiantis pasiekti maksimalų plieno kietumą. Didėjant lazerio galiai, tiek reikiamam paviršiaus kietumui, tiek sukietinimo gyliui pasiekti optimalus galios tankis mažėja. Nustatyta, kad plieno AC16 maksimalus kietumas nepriklauso nuo lazerio galios tankio. Legiruojantieji elementai gali padidinti sukietinimo gylį. Nedidelis paviršiaus aplydymas gali palengvinti sukietinimo procesą ir padidinti paviršiaus kietumą. Sukietinimo gylis dažniausiai padidėja padidėjus lazerio galiai ir/arba lazerio galios tankiui. Kaip ir kitų tipų lazeriai, pluoštinis lazeris tinka vidutinio anglingumo plienams sukietinti.

F. Qiu, V. Kujanpää

TRANSFORMATION HARDENING OF MEDIUM-CARBON STEEL WITH A FIBER LASER: THE INFLUENCE OF LASER POWER DENSITY

S u m m a r y

This paper investigates the effects of laser power density of a fiber laser on surface transformation hardening of two types of medium-carbon steels. An out-of-focus laser beam produced by a fiber laser system is used to produce an irradiated track on the surface of the samples. The tests use two types of medium-carbon steels with different initial microstructures, including X15 containing ferrite and pearlite and AC16 composed of tempered martensite. The tests on X15 show that for each laser power there is an optimum power density that produces the maximum hardness. With increased laser power, the optimal power density for both surface hardness and hardened depth is lowered. For AC16 tests, the maximum hardness value is not found to be dependent on laser power density. Alloying elements may increase the hardened depth. Slight surface melting may facilitate the hardening process and increase the surface hardness. The hardened depth is generally increased with higher laser power and/or laser power density. Compared with other types of lasers, fiber laser is a competitive tool in hardening of medium-carbon steels.

Keywords: fiber laser, hardening, carbon steel, power density, pearlite and ferrite, tempered martensite.

Ф. Киу, И. Куянпаа

ИЗМЕНЕНИЕ ТВЕРДОСТИ ПОВЕРХНОСТИ СРЕДНЕУГЛЕРОДИСТЫХ СТАЛЕЙ ПРИ ПОМОЩИ ВОЛОКОННЫХ ЛАЗЕРОВ: ВЛИЯНИЕ ПЛОТНОСТИ МОЩНОСТИ ЛАЗЕРА

Р е з ю м е

В статье рассматривается влияние плотности мощности волоконного лазера на изменение твердости поверхности двух среднеуглеродистых сталей. Расфокусированый луч лазера, полученный при помощи системы волоконных лазеров, использован для облучения поверхности образца. Для экспериментов использованы две среднеуглеродистые стали с разными исходными микроструктурами: сталь Х15 с ферито-перлитной и сталь АС16 с отпущенного мартенсита структурами. Исследования стали Х15 показали, что для лазера любой мощности существует оптимальная плотность мощности, обеспечивающая максимальную твердость. При повышении мощности лазера оптимальная плотность мощности как на твердость поверхности, так на глубину упрочнения уменьшается. Определено, что для стали АС16 максимальная твердость не зависит от плотности мощности лазера. Легирующие элементы могут увеличить глубину упрочнения. Наплавка поверхности может облегчить процесс упрочнения и повысить твердость поверхности. Глубина упрочнения чаще всего увеличивается при повышении мощности лазера и/или плотности мощности лазера. По сравнению с другими типами лазеров, волоконный лазер является равноценным инструментом для упрочнения среднеуглеродистых сталей.

Received December 09, 2010
Accepted May 19, 2011

PUBLICATION 2

Qiu, F., Uusitalo, J. and Kujanpää, V. (2012)

LASER TRANSFORMATION HARDENING OF CARBON STEEL: THE MICROHARDNESS ANALYSIS ON MICROSTRUCTURAL PHASES

The paper has been published in
Surface Engineering, available online
DOI: 10.1179/1743294412Y.0000000049
InPress

Laser transformation hardening of carbon steel: microhardness analysis on microstructural phases

F. Qiu*[1], J. Uusitalo[2] and V. Kujanpää[1,3]

This study investigates the microhardness and microstructure of different steels hardened by a fibre laser. Rolled steel, quenched and tempered steel, annealed alloyed steel and conventionally through hardened steel were tested. Microhardness (HV0·01) was measured in martensite, pearlite, ferrite and cementite structures at different depths below the laser irradiated surface. The microhardness results were compared with the conventional macrohardness (HV5) results. The grain size of rolled ferritic–pearlitic steels had distinct effect on microhardness. The macrohardness of quenched and tempered steel might be markedly influenced by the homogeneity of alloy contents. In high carbon steel, cementite is ~150 HV harder than pearlite. Annealed alloyed steels achieved high surface hardness but poor hardened depth. Dispersed granular pearlite did not affect the microhardness of soft annealed steel. The macrohardness of the base material was close to the microhardness of the softer phase structure. The measured microhardness was about 100–250 HV higher than the macrohardness.

Keywords: Steel, Fibre laser, Hardening, Microhardness, Grain size, Microstructure

Introduction

Laser transformation hardening is a well known process of producing hard, wear resistant areas on the workpiece while retaining the bulk material unaffected. A defocused laser beam is usually used to heat up the material surface above its austenisation temperature, allowing formation of austenite. The base material surrounding the laser irradiated area acts as a heat sink, causing quick self-quenching and phase transformation to martensite.[1–4] Surface hardening of steel has been mostly studied with conventional hardness measurement, which typically uses a load of several kilograms. However, metallographic analysis of specific phases and microstructures frequently demands local hardness measurement within a small scale such as tens of micrometres. Unfortunately, such investigations on phase transformation and microstructural transition of laser surface hardened steel are not much available. A microhardness test device uses a very small load (down to a few grams) and is capable to produce indentations within a few micrometres in diameter, making precise local and even in grain hardness measurement possible.[5–7] Microhardness measurement also provides a basis for quality control of thin metallic material and small parts of precision instruments.

[1]Laser Processing Laboratory, LUT Metal, Lappeenranta University of Technology, Lappeenranta, Finland
[2]Materials Engineering Laboratory, Department of Mechanical Engineering, University of Oulu, Oulu, Finland
[3]VTT Research Centre

*Corresponding author, email feng.qiu@lut.fi

Published by Maney on behalf of the Institute
Received 27 March 2012; accepted 30 July 2012
DOI 10.1179/1743294412Y.0000000049

In recent years, diode pumped fibre laser systems have been quickly developed for industrial applications.[8–11] Fibre lasers are expected to be suitable for surface treatment of carbon steels, as the wavelength of radiation produced by laser diodes can be efficiently absorbed by iron based materials.[12–14]

This study investigated the microhardness of martensite, pearlite, ferrite and cementite on various laser irradiated carbon steel samples. Microhardness was measured at the irradiated surface at different depths of the heat affected zone (HAZ) and in the base material. Macrohardness measurement was performed for comparison regarding carbon and alloy content and grain size. Quenched and tempered steels were compared with other materials on the microhardness and homogeneity with respect to the initial microstructures.

Experimental

The experiment was performed in a work cell consisting of a CNC XY table and a YLR-5000-S fibre laser equipment that produces a laser beam with a wavelength of 1070–1080 nm and a maximum nominal output power of 5 kW. The experiment used a focusing lens with a focal length of 150 mm and an output fibre core diameter of 200 μm. All the tests were performed with a constant laser power of 1875 W and a distance off the focus of 80 mm, producing a laser power density of 12 735 W cm^{-2}. A constant traverse rate of 8·0 mm s^{-1} was used. The angle between the optical axis and the surface of the sample was 90°. No shielding gas was used. The samples were air cooled after the treatment.

The hardening tests were performed on low, medium and high carbon steel samples with various alloy contents, grain sizes and initial microstructures as given in Table 1. Sample 1 (case hardening steel) and sample 3 (as rolled high silicon steel) contained ferrite and pearlite with distinct grain boundary. Sample 4 (ball and roller bearing steel) consists of pearlite and cementite grains. Sample 2 (alloyed steel) and sample 5 (vacuum degassed Cr–Ni–Mo alloyed mould steel) were composed of tempered martensite structures. Sample 6 (alloyed tool steel) and sample 7 (hot work die steel) contained ferrite and fine granular pearlite.[15] The ASTM grain size number was measured in samples 1, 3 and 4 via the mean grain diameter method.[16] As samples 2, 5, 6 and 7 did not contain distinct grain boundaries in their microstructures, their grain sizes were not available. The surface roughness of all samples R_a was $\sim$2·5 μm.

The macrohardness (HV5) of the samples was measured with a conventional Vickers hardness tester using a 5 kg load. A CSM microhardness tester with a 10 g load was used for microhardness (HV0·01) measurement. Five random measurements were performed at each of the measured depths in each appropriate phase structure. Besides measurement of martensite, in grain microhardness measurement was performed in pearlitic and ferritic grains of samples 1 and 3 and pearlitic and cement grains of sample 4. For samples 2, 5, 6 and 7, the microhardness was measured according to the depth only. The average value was used as the macro- and microhardness at this depth. Hardened depth in this study was defined as the depth where measured macrohardness was >500 HV below the centre of the laser irradiated track. Besides, carbon and alloy content were measured on samples 2 and 5 with energy dispersive spectroscopy method (EDS) combined with a scanning electron microscope.

Results and discussion

Figures 1–3 contain the measured hardness profiles along the depth below the laser treated surface of the materials. The micro- and macrohardness of various phase structures at different depths are compared. The microscopic views of the microstructures at the surface, in the HAZ and in the base material are shown in Figs. 4–6.

Hardness and microstructure of rolled medium carbon steel and through hardened high carbon steel

Figure 1 describes the micro- and macrohardness of rolled medium carbon steels (samples 1 and 3) and the through hardened high carbon steel (sample 4). The corresponding microstructure in different depths of the samples is seen in Fig. 4. The surface microstructure of samples 1, 3 and 4 is fully martensitic as can be noticed in Fig. 4*a*, *d* and *g*. As expected, the surface macrohardness is fully dependent on the carbon content. The macrohardness of samples 1, 3 and 4 is 505, 704 and 812 HV with 0·20, 0·36 and 0·95% C respectively (Fig. 1*a*). However, interestingly, the microhardness of martensite grains in the same structures is not much different. The microhardness on the surface of samples 1, 3 and 4 are 945, 938 and 1051 HV respectively. The difference in the behaviour between micro- and macrohardness is discussed in more detail in the section on 'Microhardness (HV0·01) versus macrohardness (HV5)'. Deeper from the surface, the ferritic–pearlitic structures in samples 1 and 3 can be distinguished, and in sample 4, pearlite and cementite grains can be seen (Fig. 4*c*, *f* and *i*).

As Fig. 1*a* shows, the microhardness of samples 1, 3 and 4 starts to dramatically decrease between 0·6 and 0·8 mm deep, which can be presumed to be the depth of fully martensitic layer. For samples 1 and 3, partially martensitic structure may be present between 0·6 and 1·6 mm, causing gradually reduced microhardness. In sample 1, pearlite at 0·8 mm deep (HAZ) shows higher microhardness (761 HV) than the base material (252 HV). This is possibly caused by homogenisation with decreased grain size and can be noticed by comparing Fig. 4*b* and *c*. Similarly, in sample 3, at the depth of 0·8 mm, pearlite gives markedly high microhardness of $\sim$796 HV compared with the base material (490 HV). Comparison of grain size can be seen in Fig. 4*e* and *f*. Different from samples 1 and 3, sample 4 shows respectively constant microhardness of cementite and pearlite at 0·8 mm deep and beneath. Because of the high carbon content and the presence of ferrite only in the pearlite grains, carbon diffusion may have been largely restrained, and the original grain size is not much changed. As the in grain indentation shows, the microhardness of cementite ($\sim$559 HV) is distinctly higher than pearlite ($\sim$413 HV) because cementite consists of pure iron carbide.

As seen in Fig. 1*b*, the microhardness of ferrite of samples 1 and 3 at 0·8 mm deep is respectively 376 and 315 HV, which is considerably higher than in the base material (216 HV at 2 mm deep). As exhibited in Fig. 4*b*, this is likely due to the reduced grain size of ferrite caused by recrystallisation. In deeper structures, microstructural grains remain larger since less grain boundaries are formed inside the original ferrite grains

Table 1 Samples used in test*

Sample no.	Grade	Grain size (ASTM)	Delivered condition	Compositions/wt-%						
				C	Si	V	Cr	Mn	Ni	Mo
1	AISI 4820	10	Hot rolled	0·203	0·194	0·009	1·142	1·201	0·210	0·060
2	AISI 4340	NA	Q&T	0·347	0·331	0·007	1·397	0·697	1·355	0·169
3	Imatra Imamic	8·5	As rolled	0·362	1·264	0·117	0·202	1·082	0·139	0·032
4	AISI 5210	7	Through hardened	0·951	0·246	0·005	1·432	0·385	0·137	0·022
5	AISI P20 mod.	NA	Q&T	0·373	0·366	0·006	1·86	1·470	1·172	0·201
6	AISI H13	NA	Soft annealed	0·389	0·971	0·922	4·95	0·342	0·237	1·255
7	AISI H10 mod.	NA	Soft annealed	0·400	0·380	0·834	2·800	0·73	0·100	2·170

*Composition was given by the steel manufacturer.

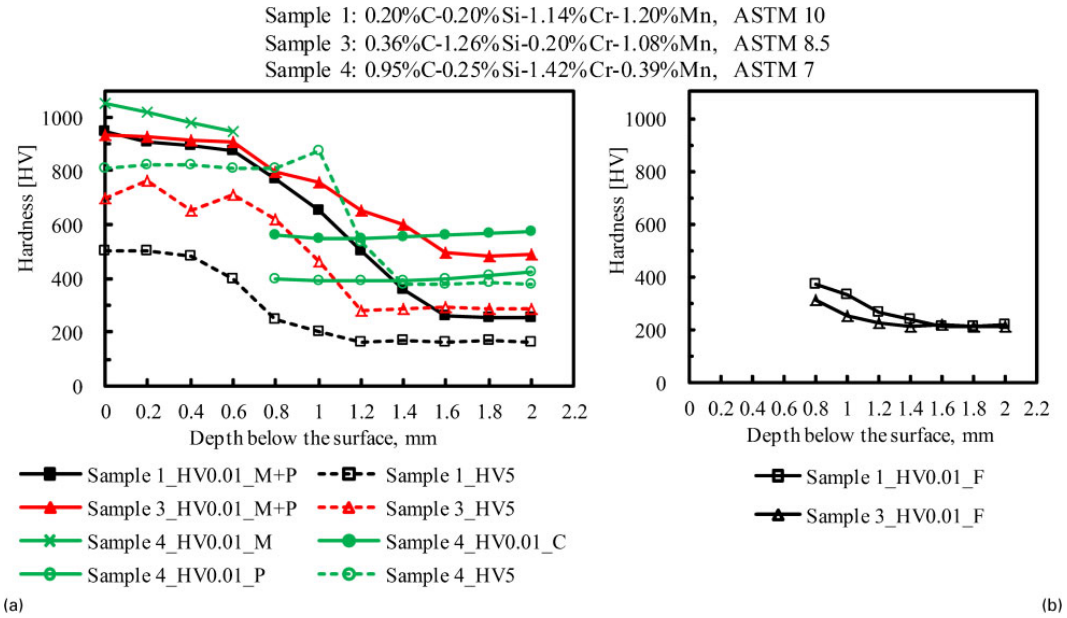

a microhardness of non-ferritic structures and macrohardness; *b* microhardness of ferritic structures. M: martensite, P: pearlite, C: cementite and F: ferrite (microhardness: HV0·01; macrohardness: HV5)

1 Hardness profiles along depth of samples 1, 3 and 4

(Fig. 4*c* and *f*). At the depth of 0·8 to 1·6 mm, sample 1 shows higher microhardness of ferrite than sample 3, although sample 3 contains much higher Si content that aids to increase the hardness of ferrite.[16] This is likely due to the markedly larger ferritic grain size of sample 3 compared with sample 1, as seen in Fig. 4*b* and *e*. See the explanations of microhardness measurement in the section on 'Microhardness (HV0·01) versus macrohardness (HV5)'.

Figure 1 also indicates that the macrohardness of the base material is close to the microhardness of the softer phase structure. For samples 1 and 3, the microhardness of ferrite is close to the macrohardness. For sample 4, the macrohardness is approximately equal to the microhardness of pearlite. An explanation is the plastic deformation of different structures as macrohardness indentation is performed. A load of several kilograms used in Vickers hardness test drives the diamond indenter into the material, causing plastic deformation of a number of micrograins nearby the produced marker. In ferritic–pearlitic structure, ferrite contains almost pure α-iron, and pearlite includes 88% ferrite and 12% cementite. Owing to the body centred cubic crystal lattice structure of α-iron, ferrite grain is thought to have lower yield point than cementite (Fe_3C) that features orthorhombic structure.[17] Thus, ferrite grains could be more plastically deformed than pearlite grains, and this might significantly affect the measured macrohardness value.

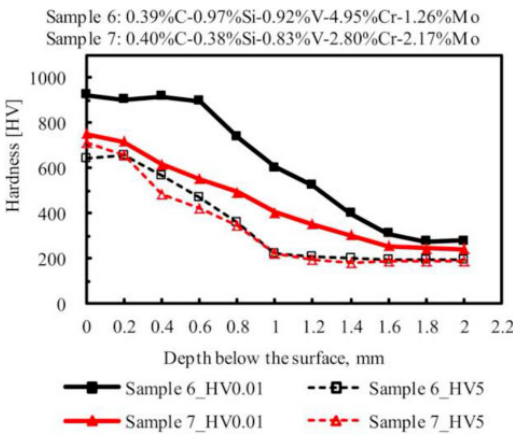

2 Hardness profiles of samples 6 and 7 along depth of material (microhardness: HV0·01; macrohardness: HV5)

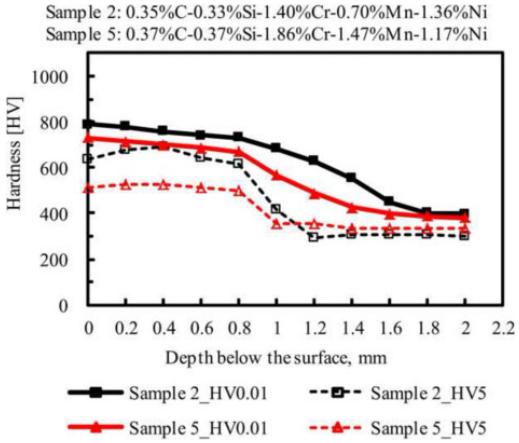

3 Hardness profiles of samples 2 and 5 along depth of material (microhardness: HV0·01; macrohardness: HV5)

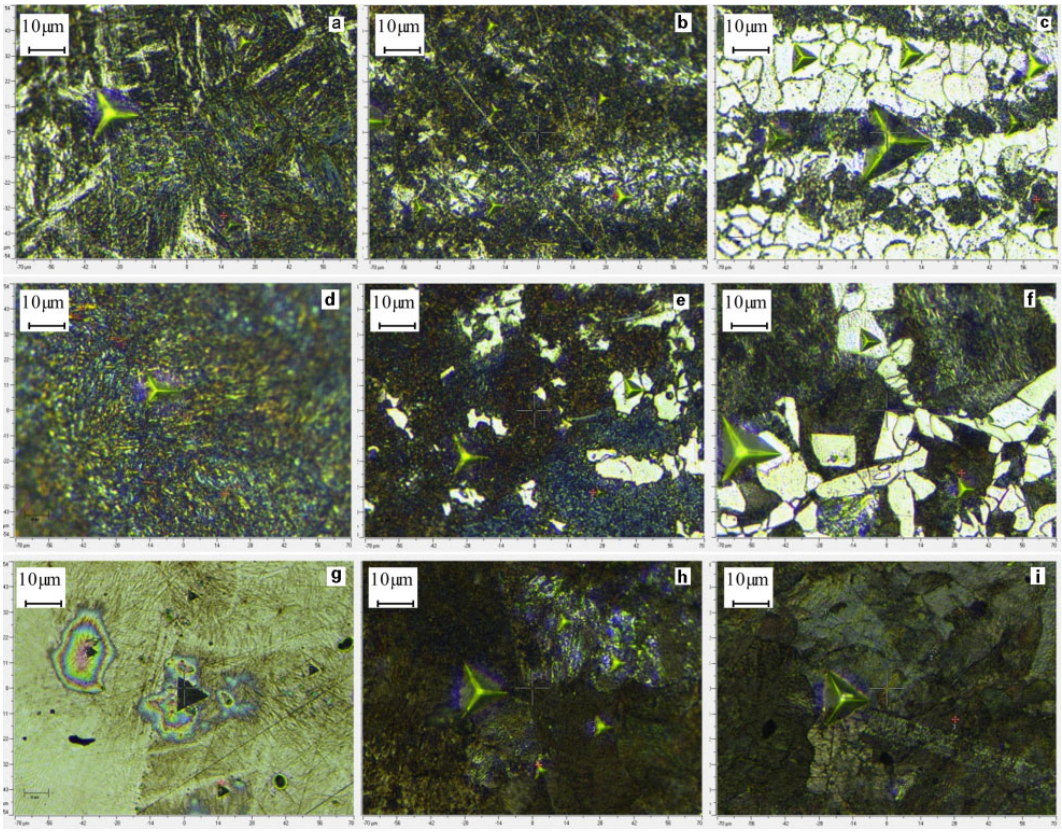

a sample 1, surface; *b* sample 1, 0·8 mm deep; *c* sample 1, 2 mm deep (base material); *d* sample 3, surface; *e* sample 3, 0·8 mm deep; *f* sample 3, 2 mm deep (base material); *g* sample 4, surface; *h* sample 4, 1 mm deep; *i* sample 4, 2 mm deep (base material)

4 Microstructures of samples 1, 3 and 4 at various depths (etched by 5% nital)

Hardness and microstructure of soft annealed alloyed steel

In Fig. 2 the micro- and macrohardness of the soft annealed samples 6 and 7 are shown. The corresponding microstructure in different depth of the samples can be seen in Fig. 5. Sample 7 shows a bit higher macrohardness on the surface than sample 6 (Fig. 2). The macrohardness values are 647 and 716 HV for samples 6 and 7 respectively. Yet, sample 6 exhibits drastically higher microhardness than sample 7 on the surface and until 1·6 mm deep. Consistent microhardness of >850 HV between the surface and 0·6 mm deep is noticed. These are believed to be caused by the high Cr (4·95%) and Si (0·97%) contents in sample 6. Figure 5 shows the microstructures of samples 6 and 7 at the treated surface, at 0·6 mm deep and in the base material. Owing to the soft annealing treatment in the manufacturing process, samples 6 and 7 consist of ultra fine granular pearlite structure, which is dispersed in the ferrite grains, and therefore grain boundary is hardly distinguishable. Grain growth can be noticed on the treated surface of both materials, showing visible ferrite boundaries among the formed martensite areas. The transitional layer at the depth of 0·6 mm indicates that carbon diffuses from the fine granular pearlite to the surroundings and causes local homogenisation. A similar HAZ to the depth of ~1·8 mm is produced in both samples.

Hardness and microstructure of quenched and tempered steel

Figure 3 gives the micro- and macrohardness of quenched and tempered steel (samples 2 and 5). The corresponding microstructure in different depths of the samples can be seen in Fig. 6. As compared in Fig. 3, sample 2 shows higher micro- and macrohardness and larger hardened depth, although sample 5 contains similar carbon and higher alloy contents. In order to find an explanation for this discrepancy, EDS was used. The results of EDS element content analysis are shown in Fig. 7. In the base material of samples 2 and 5, 15 circular areas of 5 μm in diameter were randomly selected, and the weight percentages of C, Cr and Mn were measured. The variation of the mass percentage indicates that Cr and Mn are markedly more homogeneous in sample 2, which is likely due to the process of production by the manufacturer. Figure 6*a* and *d* also shows visible difference on the samples' irradiated surfaces. It is suspected that the inhomogeneity might have caused the formation of retained austenite in

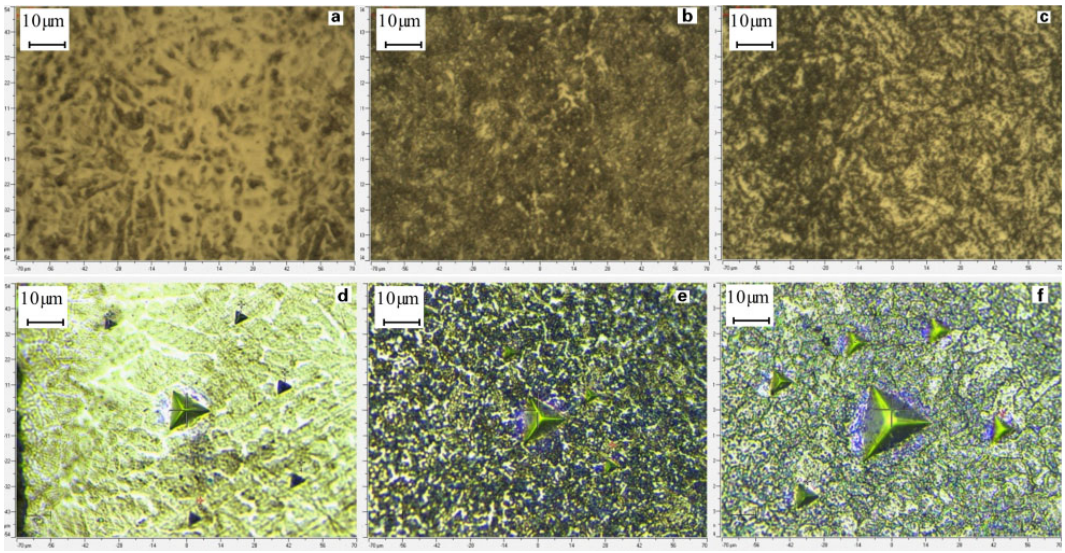

a sample 6, surface; *b* sample 6, 0·6 mm deep; *c* sample 6, 2 mm deep (base material); *d* sample 7, surface; *e* sample 7, 0·6 mm deep; *f* sample 7, 2 mm deep (base material)

5 Microstructural comparison of sample 6 (etched by 20% nital) and sample 7 (etched by 10% nital) at various depths

sample 5. Yet, this is not conclusive before X-ray diffraction test of the microstructures is performed. The macrohardness profiles exhibit a heat affected depth of ~1 mm on both samples.

Comparison among sample 2 (quenched and tempered steel), sample 3 (rolled steel) and sample 7 (soft annealed alloyed steel)

Samples 2, 3 and 7 are compared based on Figs. 1–3. Samples 3 and 7 give similar surface macrohardness of 704 and 718 HV respectively, while sample 2 shows markedly lower surface macrohardness (635 HV). Despite high alloy content, sample 7 shows a smaller hardened depth of ~0·4 mm than samples 3 and 2 (both ~0·9 mm). With similar carbon content, sample 3 shows the highest surface microhardness. Compared in Figs. 4*d* and 5*d*, sample 7 shows some bright grain boundaries on the surface, which are suspected to be ferrite. This means large grain size in contrast to sample 3 that has apparently more homogeneous martensite. The microhardness in the base material of sample 7 is nearly equivalent to the in grain microhardness of ferrite in sample 3, showing that the dispersed granular pearlite has little effect on the microhardness.

Microhardness (HV0·01) versus macrohardness (HV5)

The microhardness (HV0·01) results are compared with macrohardness (HV5) of the tested samples in Figs. 1–3. Comparisons show that measured microhardness values are around 100–250 HV higher than macrohardness. An earlier developed model revealed the influence of indentation size on the measured hardness of crystal materials, as shown in equation (1).[18] This model was later used as a base for microhardness simulations.[19] Comparing indentations using a very small load (e.g. 10 g) and a conventional one (5 kg), H_d can represent the microhardness and H_0 the macrohardness. Equation (1) indicates that the microhardness is constantly higher than macrohardness

$$\frac{H_d}{H_0} = \left(1 + \frac{h^*}{h_i}\right)^{1/2} \tag{1}$$

where H_d is the hardness for a given depth of indentation; H_0 is the hardness in the limit of infinite depth; h^* is a characteristic length depending on the indenter shape, shear modulus and H_0; and h_i is the depth of indentation.

The dislocation theory also provides a qualitative explanation for this phenomenon. It is summarised in generally known Petch–Hall relationship, as given in equation (2)

$$R_e = R_i + K d_g^{-1/2} \tag{2}$$

where R_e is the yield point, R_i is the stress required to make the dislocations move in the grains, K is a constant and d_g is the grain diameter.

Compared with microhardness test, macrohardness indentation produces a deeper and wider mark that crosses a number of grains. Plastic deformation initiates at some of the sliding dislocations while new dislocations are created as well.[20] Differently, microhardness indentation generates a much smaller marker, and thus, fewer grains are affected, meaning that fewer slidable dislocations are present as plastic deformation occurs. Therefore, R_i for microhardness indentation is expected to be higher, and R_e is accordingly higher than that for macrohardness. In in grain microhardness measurement, since the indentation marker is smaller than the grain size, d can be regarded as infinitely large, and thus, in equation (2), R_e is approximately equal to R_i. This means that the yield point for in grain indentation is basically determined by the properties of the in grain

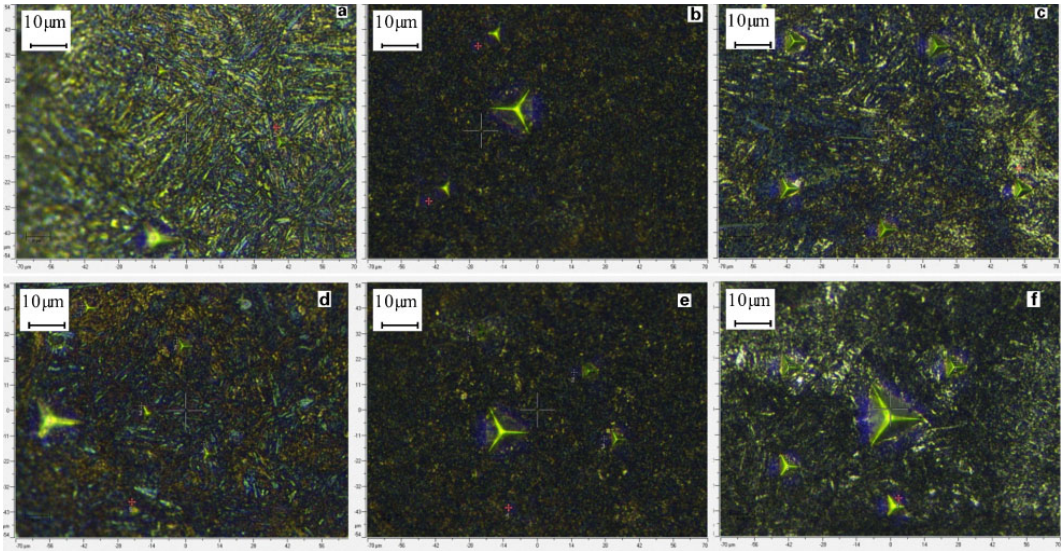

a sample 2, surface; *b* sample 2, 0·9 mm deep; *c* sample 2, 2 mm deep (base material); *d* sample 5, surface; *e* sample 5, 0·9 mm deep; *f* sample 5, 2 mm deep (base material)

6 Microstructural comparison of samples 2 and 5 at various depths (etched by 5% nital)

material. Equation (2) also indicates that a fine grained material with a smaller d may exhibit higher yield point and hardness than a coarse grained one.

Conclusions

This study investigated the microhardness of laser hardened medium carbon rolled steels, annealed alloyed steels, quenched and tempered steels and a high carbon through hardened steel. Microhardness was measured in martensite, pearlite and ferrite structures at different depths below the irradiated material surface. The micro- and macrohardness profiles of the samples were compared. Five random measurements of microhardness were performed at each of the measured depths in each appropriate phase structure. The average value was used as the result for discussion.

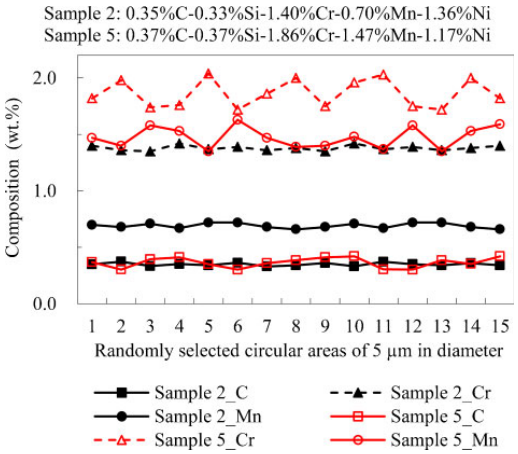

7 Element analysis (SEM) of C, Cr and Mn on samples 2 and 5

For rolled ferritic–pearlitic steels, grain size distinctly affected the homogeneity of martensite and the microhardness. Ferrite in the HAZ exhibited higher microhardness due to smaller grain size caused by carbon diffusion. By in grain indentation, the microhardness of ferrite (~216 HV), pearlite (~413 HV) and cementite (~559 HV) were obtained. In ferritic–pearlitic and pearlitic–cement steels, the macrohardness of the base material was close to the microhardness of the softer phase structure. The homogeneity of Cr and Mn contents might have significant effect on the macrohardness of tempered martensitic steel.

Rolled steel, quenched and tempered steel and soft annealed alloyed steel of the same carbon content were compared. Rolled steel could achieve higher microhardness of martensite on the surface. Quenched and tempered steel showed similar hardened depth to rolled steel but lower macrohardness on the surface. The micro- and macrohardness of soft annealed alloyed steel were relatively high on the surface but markedly decreased along the depth, producing a relatively small hardened depth. The microhardness of the base material was similar to ferrite, indicating that dispersed granular pearlite had little effect on the microhardness.

In this study, the measured microhardness values were about 100–250 HV higher than macrohardness. This was explained by a model of indentation size effects and the dislocation theory.

Acknowledgements

The author is grateful to Mr A. Anonen of Ovako Oy, who kindly provided the tested materials, and to Mr A. Heikkinen and Mrs P. Hovila for their instructions on

making the measurements. Without their support, this study would not have been possible.

References

1. W. M. Steen: 'Laser material processing', 3rd edn, 408; 2003, London, Springer-Verlag.
2. J. C. Ion: *Surf. Eng.*, 2002, **1**, 14–31.
3. A. Pinkerton: *Surf. Eng.*, 2009, **25**, 177–179.
4. C. E. Albright: in 'LIA handbook of laser materials processing', (ed. D. F. Farson *et al.*), Chap. 7, 223–224; 2001, Pineville, NC, Magnolia Publishing Inc.
5. D. Tabor: in 'Microindentation techniques in materials science and engineering', (ed. P. J. Blau and B. R. Lawn), ASTM STP 889, 129–159; 1986, Philadelphia, PA, American Society for Testing and Materials.
6. M. F. Yan and Z. R. Liu: *Mater. Chem. Phys.*, 2001, **72**, 97–100.
7. D. F. Mo and Z. F. Hu: *J. Iron. Steel Res. Int.*, 2009, **1**, 87–91.
8. J. Limpert, F. Rösera, T. Schreibera, I. Manek-Hönningerb, F. Salinb and A. Tünnermann: *C. R. Phys.*, 2006, **2**, 187–197.
9. P. P. Shukla and J. Lawrence: *Surf. Eng.*, 2011, **27**, 742–748.
10. M. Baumeister, K. Dickmann and T. Hoult: *Appl. Phys. A*, 2006, **85A**, 121–124.
11. Y. Kawahito, T. Terajima, H. Kimura, T. Kuroda, K. Nakata, S. Katayama and A. Inoue: *Mater. Sci. Eng. B*, 2008, **B1–B3**, 105–109.
12. J. F. Ready: 'Industrial application of lasers', 2nd edn, 599; 1997, London, Academic Press.
13. A. Tünnermann: Proc. Topical Meet. LASER'97 on 'Novel lasers, devices, and applications', 93–98; European Physical Society, Munich, Germany, June 1997.
14. F. Röser, A. Liem, S. Höfer, H. Zellmer, S. Nolte, J. Limpert, A. Tünnermann and T. Schreiber: *J. Phys. B: At. Mol. Opt. Phys.*, 2005, **38**, 681.
15. C. W. Wegst: 'The key to steel (Stahschlussel)', 21st edn, 720; 2007, New York, French & European Publications Inc.
16. K.-E. Thelning: 'Steel and its heat treatment', 2nd edn, 678; 1984, Oxford, Butterworth-Heinemann.
17. W. F. Smith and J. Hashemi: 'Foundations of materials science and engineering', 5th edn, 1056; 2009, New York, McGraw-Hill.
18. W. D. Nix and H. Gao: *J. Mech. Phys. Solids*, 1998, **46**, 441–425.
19. H. Yuan and J. Chen: *Comp. Mater. Sci.*, 2002, **25**, 253–263.
20. W. D. Callister: 'Fundamentals of materials science and engineering', 2nd edn, 824; 2004, Brisbane, Wiley & Sons.

PUBLICATION 3

Qiu, F. and Kujanpää, V. (2012)

THERMODYNAMIC MODELLING OF THE SURFACE TREATMENT OF A WIDE THIN STEEL PLATE WITH A GAUSSIAN LASER BEAM

The paper has been accepted for publication in
International Journal of Computational Materials Science and Surface Engineering,
InPress

Thermodynamic modelling of the surface treatment of a wide thin steel plate with a Gaussian laser beam

Feng Qiu* and Veli Kujanpää

Laboratory of Laser Processing,
LUT Metal, Lappeenranta University of Technology,
Tuotantokatu 2, 53850 Lappeenranta, Finland
Fax: +358-5-624-3082
E-mail: feng.qiu@lut.fi
E-mail: veli.kujanpaa@vtt.fi
*Corresponding author

Abstract: This study develops a thermodynamic model to investigate the quasi-steady thermal process of a wide thin steel workpiece irradiated with a moving Gaussian laser beam. Equations are established for temperature distribution, transformation boundaries, homogenisation time of austenite and cooling rate. The equations are numerically solved with an error of less than 10^{-8}. The temperature distributions for various thicknesses are compared with that for infinite thickness at different laser traverse speed. The lag of the peak temperature relative to the centre of laser beam is found to be limited. The conditions to produce full and partial martensite are investigated. The model is verified by comparing the calculated Ac_1 and Ac_3 depths and temperature cycles with the experimental results. For AISI 4340 steel, correction coefficients are applied to the model to produce an empirical equation for temperature cycles above 488.4°C.

Keywords: modelling; hardening; Gaussian laser beam; thermal cycle; temperature distribution; cooling rate; hardened depth.

Reference to this paper should be made as follows: Qiu, F. and Kujanpää, V. (xxxx) 'Thermodynamic modelling of the surface treatment of a wide thin steel plate with a Gaussian laser beam', *Int. J. Computational Materials Science and Surface Engineering*, Vol. X, No. Y, pp.000–000.

Biographical notes: Feng Qiu is a Ph.D. student studying in the Laser Processing Laboratory of LUT Metal, Finland. He is specialised in laser materials processing and currently focuses on laser surface treatment of carbon steels. He obtained his M.Sc. degree in Mechanical Engineering in Lappeenranta University of Technology, Finland, in 2005. He is the author of a few journal articles and conference papers.

Veli Kujanpää has 35 years of experience in welding technology, more than 27 of which also in laser processing. He is currently a Research Professor in Laser Technology Group of VTT in Lappeenranta, Finland. He is leading Laser Forum group of Finnish Welding Society and is a Member of Board of European Laser Institute. He is also a Chairman of Commission I and a national delegate of Commission IV of International Institute of Welding. He has published more than 400 papers, over 200 of which are scientific. In 1983, he was granted McHelm-Award of American Welding Society.

1 Introduction

Laser surface treatment of carbon steel is a process to produce hard, wear-resistant regions on the surface of the workpiece while the bulk material remains unchanged (Steen, 2003). The surface of the workpiece is heated to allow transformation to austenite and in the cooling phase transformed to martensite. With the development of high power laser systems, laser surface treatment of metals and alloys has become one of the widely used industrial laser processes (Babu et al., 2011; Liu et al., 2010). Heat transfer is a fundamental and crucial factor that has significant influence on the intermediate process and the result of laser surface treatment (Tanasawa and Lior, 1992; Rozniakowska and Yevtushenko, 2005; Ma, 2004). To investigate the thermodynamic process, qualitative and quantitative analysis using mathematical methods are thus required.

In practice, a simply defocused Gaussian laser beam is often used as the heat source for surface treatment, although special optics can be installed for desired shape and energy distribution of laser irradiation. The defocused beam profile inherits the Gaussian energy distribution of the raw laser beam (Soskind, 2009; Kim et al., 2009; Cherezova et al., 1998). Some previous studies were attempted to solve the temperature field induced by a moving heat source. One of the earliest work was done by Carslaw and Jaeger (1959) who developed an analytical solution for the temperature distribution in a semi-infinite solid with a rectangular heat source moving on the surface. Cline and Anthony (1977) used the heat-source superimposition method to give a numerical solution for heating a semi-infinite domain with a Gaussian heat source. Manca et al. (1995) solved the temperature distribution induced by a moving Gaussian heat source in a finite domain. Further modelised study is needed to develop equations of the important parameters for laser surface treatment of steel, such as the phase transformation boundary, the heat affected zone (HAZ) and the cooling rate, and provide solutions for them. Influence of laser power, laser traverse speed and depth of the workpiece are also studied.

2 Description and solution of the problem

Figure 1 shows the schematics of the dimensions and the coordinate system. A defocused circular laser beam with the Gaussian energy distribution is used as the laser source. A fixed coordinate system is established, with the origin set in the centre of the laser spot on the surface of the workpiece. The laser beam is parallel to the z-axis and the laser spot moves at a speed v_x along x-axis. In practice, the workpiece used in laser surface treatment may have various geometries along the length and the width while the irradiated surface is mostly parallel to bottom side. Furthermore, the laser irradiated track is generally kept remote to the edges and the corners to avoid overheating. Lolov (1987) indicated that the temperature profile for $l / 2 > 10r_b$ is very close to that produced by an infinite-width solid. Therefore, this process can be considered as heat transfer in a workpiece featuring two parallel planes with finite thickness and infinite length and width. The temperature on the four perpendicular edge planes which are parallel to the z-axis is assumed to remain at the initial temperature.

Figure 1 Dimensions of the solid workpiece and the coordinates

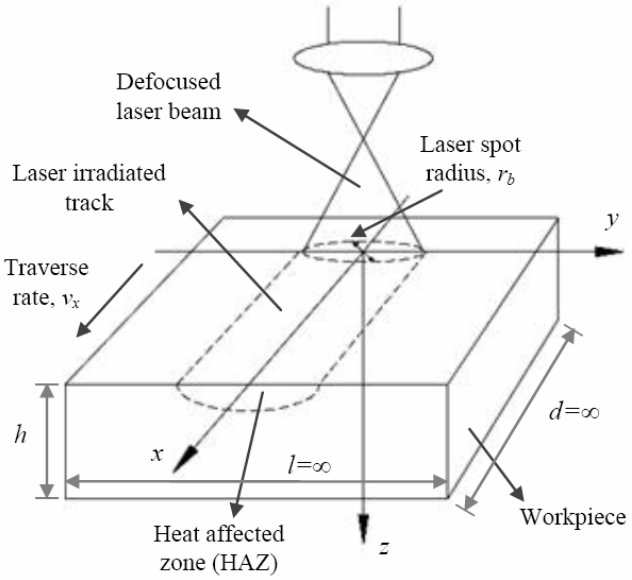

To simplify the establishment of the mathematical model, some assumptions are applied:

- Radiative heat loss from the surface is negligible in comparison to the heat conducted into the base material.
- Absorptivity (β) of laser energy is treated as a constant.
- The length (l) and the width (d) of the specimen along y-axis and x-axis are large enough so that the bulk material at the corresponding surfaces other than the irradiated surface and its opposite surface remains at initial temperature.
- Material is homogeneous with constant physical properties during the thermal cycle. Therefore, thermal conductivity and specific heat are assumed to remain unchanged.
- Heat flow occurs under a quasi-stable state, meaning that the heated material of a constant volume moves together with the heat source at the same velocity.
- Radius of the Gaussian beam is the distance from the beam centre to the position where the power density is $1/e^2$ times of the peak value.
- Melting does not occur, demanding that the surface temperature is sufficiently below the melting point of the material.

According to the heat flow theory, the heat transfer without convection in a three-dimensional isotropic and homogenous solid workpiece can be expressed as (Borgnakke and Sonnta, 2008):

$$\frac{1}{\alpha}\frac{\partial T}{\partial t} - \nabla^2 T_i = \frac{U}{k} \tag{1}$$

where

T is the temperature of the workpiece

T_i is the temperature increase above the initial temperature of the workpiece

t is time

$\alpha = \dfrac{k}{\rho C_p}$ is the thermal diffusivity

k is the thermal conductivity

ρ is the mass density

C_p is the specific heat capacity

U is the heat generated per unit volume.

Equation (1) can be converted to:

$$\frac{U}{\rho C_p} = \frac{\partial T}{\partial t} - \alpha \nabla^2 T_i \tag{2}$$

The whole thermal dynamic effect can be regarded as the superposition of multiple heat sources located at earlier coordinates (x', y', z', t'), which can be treated as unit point sources influencing the temperature at a later position (x, y, z, t).

Define $f(x, y, z, t) = \dfrac{U}{\rho C_p}$, the temperature distribution can thus be expressed as:

$$T_i(x, y, z) = \int_0^t \int_{-\infty}^{+\infty} \int_{-\infty}^{+\infty} \int_0^{+\infty} f(x', y', z', t') \cdot G(x', y', z', t' \mid x, y, z, t) dz' dy' dx' dt' \tag{3}$$

where G is the Green's function for the diffusion equation.

The Green's function for the heat equation in a domain with infinite length (x-axis) and width (y-axis) and with a finite depth (z-axis) can be written as below (Haberman, 2003; Beck et al., 1992):

$$\begin{aligned} G(x, y, z, t \mid x', y', z', t') = & \exp\left[\frac{r^2}{4\alpha(t-t')}\right] \cdot \frac{1}{4\pi\alpha(t-t')h} \\ & \times \left\{1 + 2\sum_{n=1}^{\infty} \exp\left[-\frac{n^2\pi^2\alpha(t-t')}{h^2}\right] \cos\frac{n\pi z}{h} \cos\frac{n\pi z'}{h}\right\} \end{aligned} \tag{4}$$

where $r^2 = (x - x') + (y - y')^2 + (z - z')^2$. On the surface, $z' = 0$.

$$\int_0^{+\infty} f(x', y', z', t') \cdot G(x', y', z', t' \mid x, y, z, t) dz' = I(x', y', t') \cdot (x', y', t' \mid x, y, t) \tag{5}$$

Substituting equation (5) into equation (3) gives:

$$T_i(x, y, z) = \int_0^t \int_{-\infty}^{+\infty} \int_{-\infty}^{+\infty} \frac{I(x', y', t')}{\rho C_p} \cdot G(x', y', t' \mid x, y, t) dx' dy' dt' \tag{6}$$

The power density of an ideal Gaussian laser beam traversing on the surface of a workpiece can be written as (Kogelnik and Li, 1966):

$$I(x, y, t) = \frac{2P_0}{\pi r_b^2} \exp\left[-\frac{2\left[(x - v_x t)^2 + y^2 \right]}{r_b^2} \right] \tag{7}$$

where

P_0 is the absorbed laser power

r_b is the radius of the laser beam

v_x is the traverse speed of the laser beam along x-axis.

The temperature increase can thus be calculated by substituting equation (4) and equation (7) into equation (6):

$$\begin{aligned} T_i(x, y, z) = & \int_{-\infty}^{t} \int_{-\infty}^{+\infty} \int_{-\infty}^{+\infty} \frac{1}{\rho C_p} \cdot \frac{2P_0}{\pi r_b^2} \exp\left[-\frac{2\left[(x' - v_x t')^2 + y'^2 \right]}{r_b^2} \right] \\ & \times \exp\left(-\frac{(x - x')^2 + (y - y')^2}{4\alpha (t - t')^2} \right) \cdot \frac{1}{4\pi\alpha h (t - t')} \\ & \times \left\{ 1 + 2\sum_{n=1}^{\infty} \exp\left[-\frac{n^2 \pi^2 \alpha (t - t')}{h^2} \right] \cos\frac{n\pi z}{h} \right\} dx' dy' dt' \\ = & \frac{P_0}{\rho C_p \pi h} \int_{-\infty}^{t} \frac{1}{8\alpha (t - t') + r_b^2} \cdot \exp\left(-\frac{2\left[(x - v_x t')^2 + y^2 \right]}{8\alpha (t - t') + r_b^2} \right) \\ & \times \left\{ 1 + 2\sum_{n=1}^{\infty} \exp\left[-\frac{n^2 \pi^2 \alpha (t - t')}{h^2} \right] \cos\frac{n\pi z}{h} \right\} dt' \end{aligned} \tag{8}$$

At $t = 0$, equation (8) represents the temperature distribution produced by a Gaussian distribution of the laser beam when it was at a position (x', y') at an earlier time t'. Thus, equation (8) is converted to:

$$\begin{aligned} T_i(x, y, z) = & \frac{P_0}{\rho C_p \pi h} \int_0^{+\infty} \frac{1}{8\alpha t' + r_b^2} \cdot \exp\left(-\frac{2\left[(x + v_x t')^2 + y^2 \right]}{8\alpha t' + r_b^2} \right) \\ & \times \left\{ 1 + 2\sum_{n=1}^{\infty} \exp\left(-\frac{n^2 \pi^2 \alpha t'}{h^2} \right) \cos\frac{n\pi z}{h} \right\} dt' \end{aligned} \tag{9}$$

Equation (9) is the basic equation used to solve the distribution of T_i and also provides an approach for analysing the transformed region, the homogenisation time and the cooling rate. Equation (9) expressed with dimensionless variables gives:

$$\begin{aligned} T_i = & \frac{P_0}{4\rho C_p \pi \alpha r_b} \int_0^{+\infty} \frac{\varepsilon}{(\varepsilon^2 + 1) H} \cdot \exp\left(-\frac{2\left(\left(X + V\varepsilon^2/8 \right)^2 + Y^2 \right)}{\varepsilon^2 + 1} \right) \\ & \times \left(1 + 2\sum_{n=1}^{\infty} \exp\left(-\frac{n^2 \pi^2 \varepsilon^2}{8H^2} \right) \cos\frac{n\pi Z}{H} \right) d\varepsilon \end{aligned} \tag{10}$$

where

$\varepsilon^2 = \dfrac{8\alpha t'}{r_b^2}$ is a dimensionless variable

$V = \dfrac{r_b v_x}{\alpha}$ is dimensionless traverse speed

$H = \dfrac{h}{r_b}$ is dimensionless thickness of the workpiece

$X = \dfrac{x}{r_b}$, $Y = \dfrac{y}{r_b}$ and $Z = \dfrac{z}{r_b}$ are dimensionless x, y, z coordinates.

Define

$$c = \frac{P_0}{4\rho C_p \pi \alpha r_b} \tag{11}$$

$$u = \int_0^{+\infty} \frac{\varepsilon}{(\varepsilon^2+1)H} \cdot \exp\left(-\frac{2\left(\left(X + V\varepsilon^2/8\right)^2 + Y^2\right)}{\varepsilon^2+1}\right) \times \left\{1 + 2\sum_{n=1}^{\infty} \exp\left(-\frac{n^2\pi^2\varepsilon^2}{8H^2}\right)\cos\frac{n\pi Z}{H}\right\} d\varepsilon \tag{12}$$

Thus,

$$T_i = c \cdot u \tag{13}$$

c is a constant determined by the absorbed laser power, laser spot size and the physical properties of the material. u can be regarded as the dimensionless temperature increase. T_i is thus linearly dependent on u. An analytical solution of u may be complicated but u can be numerically evaluated via computational tools.

3 Results and discussion

Equation (12) is the base for all discussions in this study and is directly used to solve the u profile for different dimensionless thickness H and speed V. Formulas are derived from equation (12) to describe and solve the boundary of transformation, the homogenisation time and the cooling rate. The results are numerically solved by a computation tool with an error of less than 10^{-8}.

3.1 The temperature distribution

The u profiles are solved in equation (12), acquired with H in a range of 1–15 and V of 0.5–10. Computed values of u on the workpiece's surface in a 3D mesh grid view is shown in Figure 2, which is solved with H = 10 and V = 3. The u profile represents the distribution of T_i by a scale factor of 1/c as indicated in equation (13).

Figure 2 The distribution of u on the surface of a workpiece produced by a moving Gaussian heat source (see online version for colours)

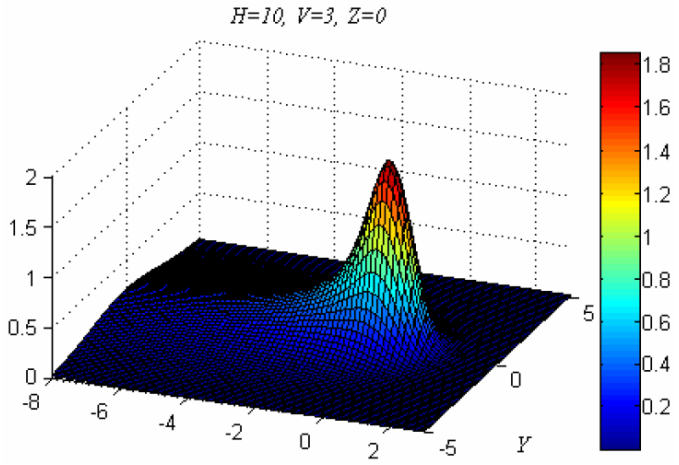

The u profiles for different H and V can be calculated from equation (12) and thus the peak of u, $u_{\max}$, can be as well obtained numerically. The peak temperature, $T_{i_{\max}}$, can be calculated with equation (11) and equation (13):

$$T_{i_{\max}}(H,V)=\frac{P_0}{\rho C_p \alpha r_b}u_{\max}(H,V) \tag{14}$$

As Figure 3(a) shows, the peak values of u for H = 1, 2, 5 and 10 at V = 5 are respectively:

$$u_{\max|H=1,V=5}=2.631;\quad u_{\max|H=2,V=5}=2.209;$$
$$u_{\max|H=5,V=5}=1.685;\quad u_{\max|H=10,V=5}=1.571.$$

Thus, the peak temperatures are:

$$T_{i_{\max}|H=1,V=5}=\frac{0.209P_0}{\rho C_p \alpha r_b};\quad T_{i_{\max}|H=2,V=5}=\frac{0.176P_0}{\rho C_p \alpha r_b};$$
$$T_{i_{\max}|H=5,V=5}=\frac{0.134P_0}{\rho C_p \alpha r_b};\quad T_{i_{\max}|H=5,V=5}=\frac{0.125P_0}{\rho C_p \alpha r_b}.$$

For $H=\infty$ ($h=\infty$), the peak value of u is 1.460 and the peak temperature is:

$$T_{i_{\max}|H=\infty,V=5}=\frac{0.116P_0}{\rho C_p \alpha r_b}.$$

Similarly, the peak values of u at different V for H = 10 are obtainable in Figure 3(b).

Figure 3 The u profile versus dimensionless coordinate X ($Y = Z = 0$), (a) for different H at $V = 5$ (b) at different V for $H = 10$ (see online version for colours)

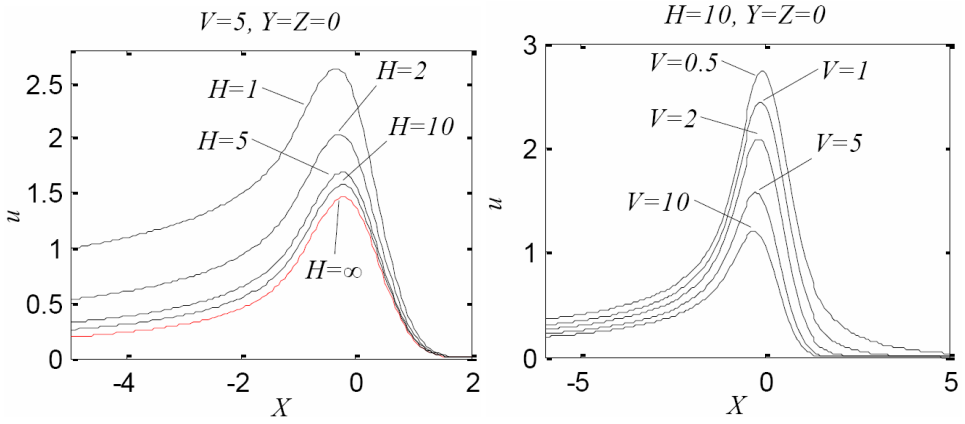

(a) (b)

By letting $X = Y = Z = 0$ in equation (12), H and V are correlated in Figure 4 which shows the u profiles at the centre of the laser irradiated track for different H and V. The u gradient along Z axis is lowered to minimum when V and/or H are sufficiently large, meaning that the surface temperature is close to constant for a thick workpiece. Similarly, the surface temperature changes little with the thickness if the traverse speed is sufficiently high. As Figure 4(b) shows, a large H corresponds to a u profile that is sufficiently close to that with $H = \infty$. The relative difference between a parameter M and to the reference M_{ref}, e_r is defined as:

$$e_r = \frac{M - M_{ref}}{M_{ref}} \cdot 100\% \tag{15}$$

Laser heat treatment allows the surface temperature to rise to above the starting temperature of austenitisation and beneath the melting point of carbon steel, which is constantly below around 1,500°C for both hypo- and hyper-eutectoid steel (Thelning, 1984). The temperature increase can be expressed as:

$$T_i \le T_m - T_0 \tag{16}$$

where

T_m is the melting point of the material

T_0 is the initial temperature of the material.

Thus, a difference equal to 3% of T_i is less than 45°C, which is assumed to be ignorable in this study. Table 1 shows the relative difference of $H = 10$ and $H = 15$ compared with $H = \infty$ at different V. For $H = 15$ at $V \ge 2.5$, e_r is lower than 3%. For $H = 10$, e_r at $V = 10$ is 4.58%. As shown in Figure 4, e_r for $H = 15$ at $0 < V < 1$ is larger than 8.95% and thus cannot be simply ignored.

It is noticeable that the maximum value of u for $H = \infty$ is $u_{H=\infty,V=0} = 2.51$ at $V = 0$. Thus, according to equation (10) and equation (12):

$$T_i\big|_{H=\infty,V=0} = \frac{P_0}{4\rho C_p \pi \alpha r_b} \cdot 2.51 \tag{17}$$

Substituting equation (17) into equation (16) gives:

$$P_0 \le \frac{5(T_m - T_0)}{\rho C_p \alpha r_b} \tag{18}$$

Equation (18) can be understood as the maximum of the absorbed laser power that does not cause melting on a very thick workpiece with a non-moving Gaussian laser beam.

Figure 4 The u profiles for different H and V, (a) u versus H at different V (b) u versus V for different H (see online version for colours)

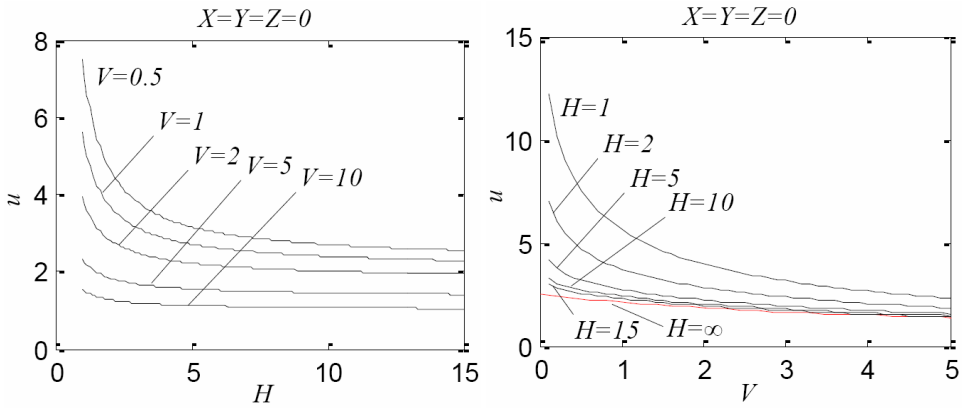

(a) (b)

Table 1 u with $H = 10$ and $H = 15$ compared with $H = \infty$ at different V

V	*1*	*2*	*3*	*5*	*5.2*	*7.5*	*10*
$e_r\|_{H=10}$ (%)	14.91	11.27	9.46	7.54	7.2	5.68	4.58
$e_r\|_{H=15}$ (%)	8.95	6.42	5.10	3.59	2.91	1.91	0.83

Define $X_{t=0}$ as the X coordinate that corresponds to $t = 0$. Thus, X can be expressed as:

$$X = X_{t=0} - \frac{\alpha}{r_b^2} Vt \tag{19}$$

Substituting equation (19) into equation (12) gives:

$$u = \int_0^{+\infty} \frac{\varepsilon}{(\varepsilon^2+1)H} \cdot \exp\left(-\frac{2\left(\left(X_{t=0} - \frac{\alpha}{r_b^2} Vt + V\varepsilon^2/8 \right)^2 \right) + Y^2}{\varepsilon^2+1} \right) \times \left\{ 1 + 2\sum_{n=1}^{\infty} \exp\left(-\frac{n^2\pi^2\varepsilon^2}{8H^2} \right) \cos\frac{n\pi Z}{H} \right\} d\varepsilon \tag{20}$$

The u-X profile is thus converted to a u-t profile.

3.2 Position of the peak temperature

Noticeable in Figure 3, the peak of u is always with a lag behind the centre of the heat source due to moving laser beam. This position $X_{u=\max}$ is dependent on H and/or V as indicated in Figure 5 and Figure 6.

Figure 5 The position of the peak of u versus H at different V

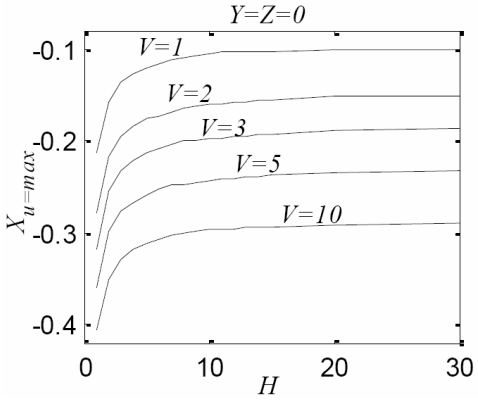

Figure 6 The X coordinate of the peak of u versus V for different H, (a) V in the range of 0.5 to 10 (b) V in the range of 0.5 to 300 (see online version for colours)

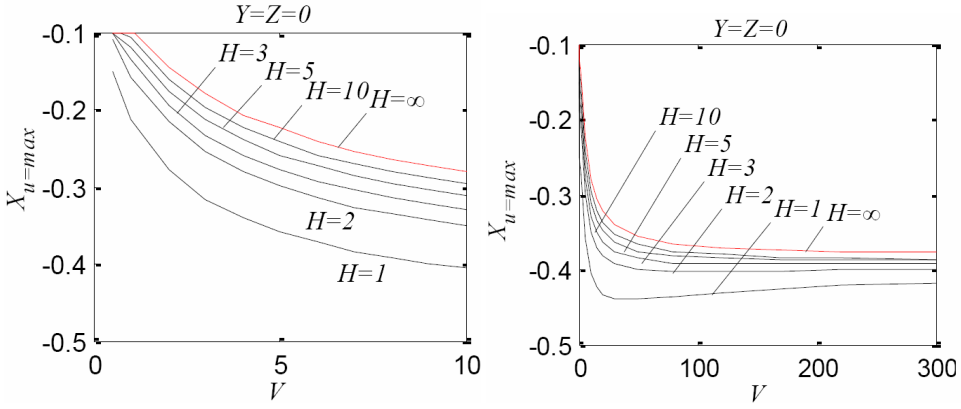

As Figure 5 shows, the lag of the peak of u is decreased as H increases and approaches to a constant limit determined by V when H is sufficiently large. For $H \geq 2$, $X_{u=\max}$ does not appear to change significantly. Figure 6 indicates the influence of V on $X_{u=\max}$ for different H. The lag is increased with V in a limited range depending on H. Shown in Figure 6(b), for each H $X_{u=\max}$ approaches a limit as V is increased to infinite. For $H \geq 2$, $X_{u=\max}$ is basically constant at $V \geq 150$. This means that for surface treatment with significantly high traverse speed, the peak temperature is located at a fixed-like position with respect to centre of the laser beam. For a very thick workpiece ($H >> 10$) irradiated with $V \geq 150$, $X_{u=\max} \approx -0.383$.

3.3 Ac_1 and Ac_3 boundaries

As the surface of the steel workpiece is heated to above Ac_1, the temperature at which austenite begins to form during heating, initial microstructures starts to transform to austenite. This transformation is completed as the surface temperature reaches Ac_3. These conditions can be written as:

$$Ac_1 \le T_{i\max} + T_0 < Ac_3 \tag{21}$$

and

$$Ac_3 \le T_{i\max} + T_0 < T_m \tag{22}$$

where $T_{i\max}$ is the peak value of T_i.

Figure 7 The calculated Ac_1 boundary transformation region with a moving Gaussian heat source (see online version for colours)

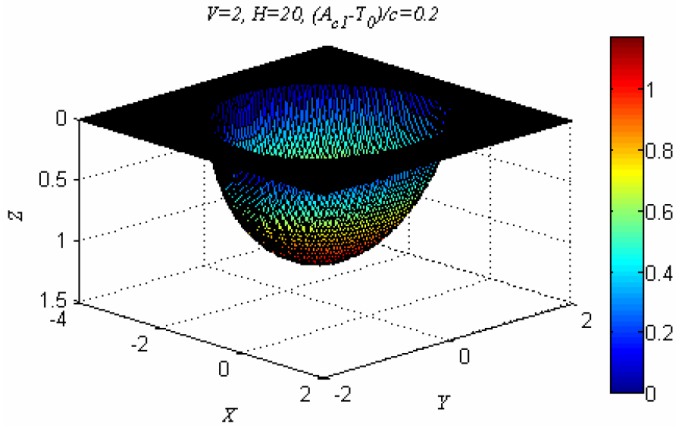

Equation (21) and equation (22) can be converted to:

$$\frac{Ac_1 - T_0}{c} = \int_0^{+\infty} \frac{\varepsilon}{(\varepsilon^2+1)H} \cdot \exp\left(-\frac{2\left(\left(X_{u=\max} + V\varepsilon^2/8\right)\right)^2 + Y_{u=\max}^2}{\varepsilon^2+1}\right) \times \left\{1 + 2\sum_{n=1}^{\infty} \exp\left(-\frac{n^2\pi^2\varepsilon^2}{8h^2}\right)\cos\frac{n\pi Z_{u=\max}}{H}\right\} d\varepsilon \tag{23}$$

and

$$\frac{Ac_3 - T_0}{c} = \int_0^{+\infty} \frac{\varepsilon}{(\varepsilon^2+1)H} \cdot \exp\left(-\frac{2\left(\left(X_{u=\max} + V\varepsilon^2/8\right)^2 + Y_{u=\max}^2\right)}{\varepsilon^2+1}\right) \times \left\{1 + 2\sum_{n=1}^{\infty} \exp\left(-\frac{n^2\pi^2\varepsilon^2}{8H^2}\right)\cos\frac{n\pi Z_{u=\max}}{H}\right\} d\varepsilon \tag{24}$$

where $X_{u=\max}$, $Y_{u=\max}$, $Z_{u=\max}$ are the X, Y, Z coordinates of the peak of u. Equation (24) describes the region that is fully transformed to austenite. Equation (23) indicates the boundary condition of the HAZ which includes the partially transformed region. $X_{u=\max}$, $Y_{u=\max}$ and $Z_{u=\max}$ numerically solved in equation (23) and equation (24) and 3D profiles representing Ac_1 and Ac_3 transformation boundaries are thus generated as shown in Figure 7.

Letting $Y_{u=\max} = 0$ in equation (23) and equation (24), the $X_{u=\max} - Z_{u=\max}$ profiles are obtained to indicate the Ac_1 and Ac_3 boundary at the centre of the laser irradiated track. Similarly, with $Z_{u=\max} = 0$, the Ac_1 and Ac_3 widths on the surface can be acquired.

3.4 The homogenisation time of austenite

The microstructures start to be homogenised as the surface temperature is heated above Ac_1. Increase of the homogenisation time for carbon steel assist in producing more homogenised austenitic microstructure. The effective homogenisation occurs in the condition of $Ac_1 \le T_i + T_0 < T_m$. Letting $T_i = Ac_1 - T_0$ in equation (10) gives:

$$\frac{Ac_1 - T_0}{c} = \int_0^{+\infty} \frac{\varepsilon}{(\varepsilon^2+1)H} \cdot \exp\left(-\frac{2\left((X + V\varepsilon^2/8)^2 + Y^2\right)^2}{\varepsilon^2+1}\right) \times \left\{1 + 2\sum_{n=1}^{\infty} \exp\left(-\frac{n^2\pi^2\varepsilon^2}{8H^2}\right)\cos\frac{n\pi Z}{H}\right\} d\varepsilon \tag{25}$$

X_1 and X_2 are the solutions for equation (25) which can be solved by numerical methods or estimated via the u profile as illustrated in Figure 8.

Figure 8 Estimation of X_1 and X_2 for ($H = 10$, $V = 5$, $Z = 0.5$)

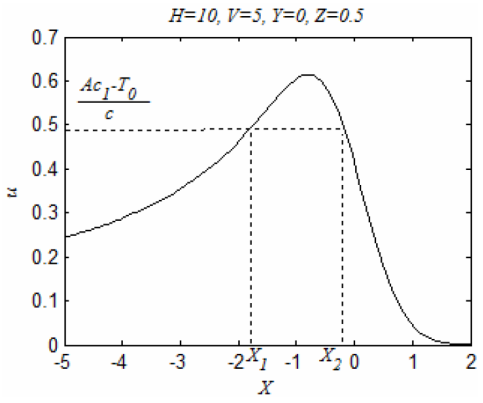

The homogenisation time t_h is thus calculated as:

$$t_h = \frac{|X_1 - X_2| \cdot r_b}{v_x} \quad (Ac_1 - T_0 \le T_{i\max} < T_m - T_0) \tag{26}$$

where $T_{i\max}$ is the peak value of is the peak value of is the peak value of T_i.

3.5 The cooling rate

The cooling rate is the velocity of temperature decrease in the cooling phase of the thermal cycle. It is one of the most important factors that determine the transformation from austenite to martensite.

According to equation (13), the cooling rate is written as:

$$R_c = -\frac{dT_i}{dt} = -v_x \frac{dT_i}{dx} \tag{27}$$

Substituting equation (11) and (13) into equation (27) gives:

$$R_c = \frac{P_0}{4\rho C_p \pi r_b^3} \cdot V \frac{du}{dX} \tag{28}$$

Define $w = V\dfrac{du}{dX}$, and equation (28) is converted to:

$$R_c = \frac{P_0}{4\rho C_p \pi r_b^3} \cdot w \tag{29}$$

R_c is linearly dependent on w, and thus w can be seen as the dimensionless cooling rate. w is derived from equation (12) as:

$$\begin{aligned} w = \int_0^{+\infty} & -\frac{V\varepsilon\left(4X + V\varepsilon^2/2\right)}{\left(\varepsilon^2+1\right)^2 H} \cdot \exp\left(-\frac{2\left(\left(X + V\varepsilon^2/8\right) + Y^2\right)}{\varepsilon^2+1}\right) \\ & \times\left\{1 + 2\sum_{n=1}^{\infty} \exp\left(-\frac{n^2\pi^2\varepsilon^2}{8H^2}\right)\cos\frac{n\pi Z}{H}\right\} d\varepsilon \end{aligned} \tag{30}$$

Figure 9 The distribution of w on the surface of a workpiece produced by a moving Gaussian heat source (see online version for colours)

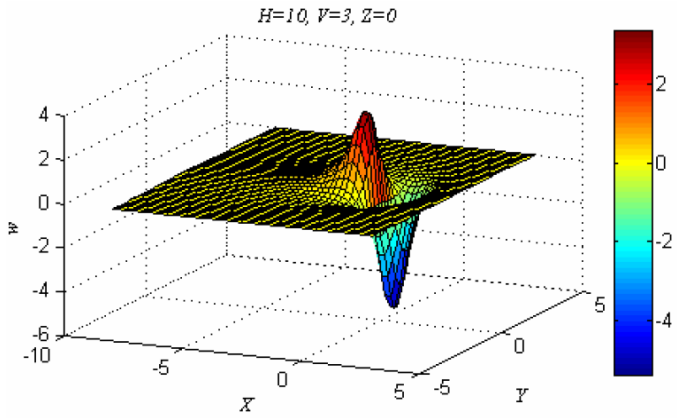

Figure 9 shows a distribution of w in 3D mesh grid generated from equation (30) using parameters of $H = 10$, $V = 3$ and $Z = 0$. Due to the linear dependence of $-\frac{dT_i}{dt}$ on w, the profile of w can be used to characterise the distribution of the cooling rate.

The w profile is generated from equation (29) and the peak value of w is acquired. Figure 10 shows the w profiles for different H at $V = 5$ and at different V for $H = 10$. Figure 11 is derived from equation (29) to show the influence of H and V on w at $X - 1$ in the middle of the irradiated track.

Figure 10 Profiles of w versus dimensionless coordinate X ($Y = Z = 0$), (a) for different H at $V = 5$ (b) at different V with $H = 10$ (see online version for colours)

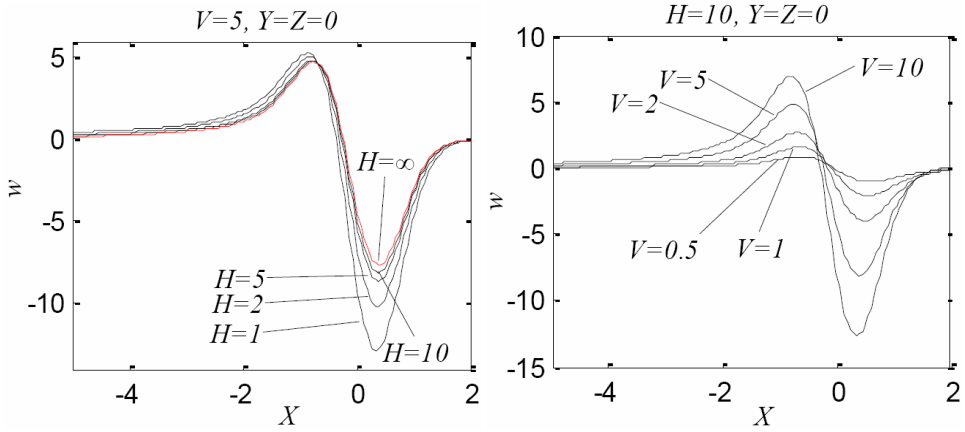

(a) (b)

Figure 11 The w profiles for different H and V, (a) w versus H at different V (b) w versus V for different H (see online version for colours)

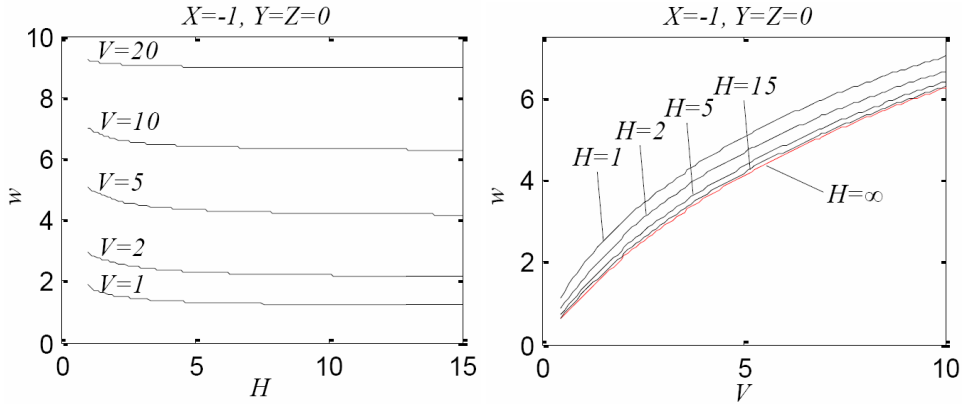

(a) (b)

Figure 11(a) shows that increase of H results in lower w but the influence is limited. As H increases to infinite, w is declined to a constant. It can be noticed that at higher V the effect of H on w is reduced. Increasing V causes markedly higher w as shown in Figure 11(b). w for $H = 10$ and $H = 15$ at different V is compared with $H = \infty$ in Table 2. It shows that e_r for $H = 10$ is less than 5% at $V > 2$. For $H = 15$ at $V \geq 8.0$, e_r is lower than 5%.

Table 2 Relative difference of w for $H = 10$ and $H = 15$ compared with $H = \infty$ at different V

V	*0.5*	*0.8*	*1*	*2*	*3*	*4*	*5*	*10*
$e_r \mid_{H=10}$ (%)	8.70	7.60	6.78	5.01	3.94	3.19	2.64	1.13
$e_r \mid_{H=15}$ (%)	5.74	4.99	4.44	3.25	2.53	2.03	1.65	1.15

Figure 12 CCT diagram for eutectoid carbon steel (see online version for colours)

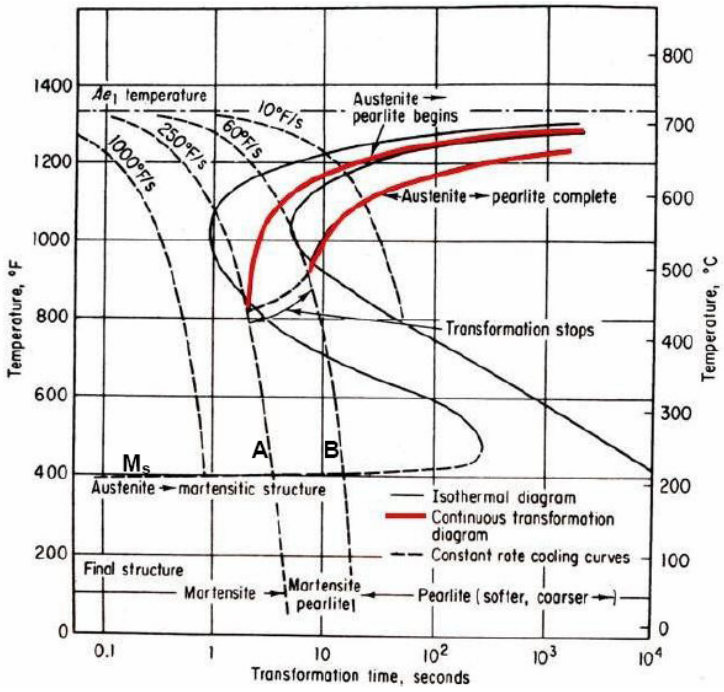

Source: Porter et al. (2009)

As the temperature reaches the martensite start temperature in the cooling phase, the cooling rate is required to exceed the critical cooling rate in order to produce 100% martensite. Figure 12 shows the continuous cooling transformation (CCT) diagram for eutectoid carbon steel. Dashed line A which is tangent to the austenite-pearlite transformation start line represents the cooling curve with exactly the critical cooling rate. Leftward is the region with higher cooling rate which produces pure martensite as well. Dashed line B indicates the highest cooling rate that produces 100% pearlite. Rightward is lower cooling rate that results in pure pearlite. The region between dashed line A and B represents production of a mixture of martensite and pearlite as the final microstructure.

Since martensite is exclusively transformed from austenite, the produced austenite in the heating phase of the thermal cycle determines the maximum amount of martensite that can be formed in the cooling phase. The prerequisite condition for full transformation to austenite is given in equation (22).

Letting $T_i = M_s - T_0$ and $Y = Z = 0$ in equation (10) gives:

$$(M_s - T_0)\cdot\frac{4\rho C_p \pi\alpha r_b}{P_0} = \int_0^{+\infty} \frac{\varepsilon}{(\varepsilon^2+1)H}\cdot\exp\left(-\frac{2\left((X+V\varepsilon^2/8)^2\right)}{\varepsilon^2+1}\right) \times\left\{1+2\sum_{n=1}^{\infty}\exp\left(-\frac{n^2\pi^2\varepsilon^2}{8H^2}\right)\right\}d\varepsilon \tag{31}$$

Equation (31) is numerically solved and $X = X_{M_s}$ is the lower solution which is in the cooling phase. Substituting $X = X_{M_s}$ into equation (30) and equation (29) gives the cooling rate at $T_i = M_s - T_0$ as:

$$R_{c|T_i=M_s-T_0} = \frac{P_0}{4\rho C_p \pi r_b^3}\cdot\int_0^{+\infty} -\frac{V\varepsilon\left(4X_{M_s}+V\varepsilon^2/2\right)}{(\varepsilon^2+1)H} \times\exp\left(-\frac{2\left(X_{M_s}+V\varepsilon^2/8\right)^2}{\varepsilon^2+1}\right)\left\{1+2\sum_{n=1}^{\infty}\exp\left(-\frac{n^2\pi^2\varepsilon^2}{8H^2}\right)\right\}d\varepsilon \tag{32}$$

$R_{c|T_i=M_s-T_0}$ solved with equation (32) is compared with Figure 12 to indicated the condition for producing martensite. The result is given in Table 3. R_{cr} is the critical cooling rate to produce 100% martensite and $R_{cr'}$ is the cooling rate to produce 0% martensite. R_{cr} and $R_{cr'}$ for carbon and alloy steels can be acquired from the corresponding CCT diagrams.

Table 3 Martensitisation under different heating temperature and cooling rate at $T_i = M_s - T_0$

$T_{i\max}$ \ R_c	$R_c \geq R_{cr}$	$R_{c'} < R_c < R_{cr}$	$R_c \leq R_{cr}$
$T_{i\max} < Ac_1 - T_0$	No martensite	No martensite	No martensite
$Ac_1 - T_0 \leq T_{i\max} < Ac_3 - T_0$	Partially martensite	Partially martensite	No martensite
$Ac_3 - T \leq T_{i\max} < T_m - T_0$	100% martensite	Partially martensite	No martensite

Table 4 Compositions of the tested samples

No.	*AISI grade*	*Delivered condition*	*Compositions (wt.%)*					
			C	*Si*	*Cr*	*Mn*	*Ni*	*Mo*
1	4820	Hot rolled	0.20	0.19	1.14	1.20	0.21	0.06
2	4340	Q&T	0.35	0.33	1.40	0.70	1.36	0.17
3	5210	Through hardened	0.95	0.25	1.43	0.39	0.14	0.02
4	P20 mod.	Q&T	0.37	0.37	1.86	1.47	1.17	0.20
5	H13	Soft annealed	0.39	0.97	4.95	0.34	0.24	1.26
6	H10 mod.	Soft annealed	0.40	0.38	2.81	0.73	0.10	2.17

Table 5 Thermal properties of the materials and processing parameters

No.	*Thermal conductivity, k, W/(m·K)**	*Thermal diffusivity, α, mm²/s*	*Ac_1, °C*	*Ac_3 / Ac_m, °C*	*Radius of laser beam, r_b, mm*	*Laser power, P, W*	*Absorptivity, β*	*Traverse speed, v_x, mm/s*
1	42.0	9.11	740	835	2.19	1,875	64%	8.0
2	33.7	8.15	715	770	2.19	1,875	64%	8.0
3	20.0	4.33	755	850	2.19	1,875	64%	8.0
4	29.0	6.30	722	760	2.19	1,875	64%	8.0
5	26.5	6.53	820	915	2.19	1,875	64%	8.0
6	33.0	6.58	790	890	2.19	1,875	64%	8.0
2	33.7	8.15	715	770	1.80	2,988	62%	32.0
					1.80	2,988	61%	34.0
					1.80	2,988	60%	36.0
					1.80	2,988	59%	38.0
					1.80	2,988	58%	40.0
					1.80	2,988	57%	42.0

Note: **k* values are acquired at 600°C.

Source: Wegst (2007)

3.6 Verification of the model

The model was examined by experiments done on low- to high-carbon steel with various alloy content as shown in Table 4. Raw materials were machined into plates with the thickness of 10 mm. The initial temperature of the tested samples, T_0, was 20°C as well as the room temperature. The irradiated surface was clean and the roughness, R_a, was about 2.5 μm. The test used a work cell consisting of a CNC XY table and a YLR-5000-S fibre laser equipment which produces a laser beam with a wavelength of 1,070–1,080 nm.

Table 5 shows the material properties and processing parameters. All the samples were tested with an 1875 W laser beam with the beam radius of 2.19 mm and a traverse speed of 8.0 mm/s. The measured Ac_1 and Ac_3 depths of the tested samples were compared with calculated results acquired from this model. Besides, Sample 2 was tested with a laser beam of 1.80 mm in radius that produces 2,988 W laser power at various moving speeds. A pyrometer was used to measure the temperature cycle during the process and the effective work range is between 488.4°C and around 2,000°C. The recorded temperature-time curves were compared with the calculated temperature profiles. The angle between the optical axis and the surface of the sample was 90 degrees. No shielding gas was used. The thermal diffusivity (α) values were calculated by the equation of definition using the provided thermal conductivity (k) as given in equation (1). The absorptivity (β) was presumed based on a previous study by Pantsar and Kujanpää (2004) who investigated the absorption of laser irradiation by low alloy carbon steel with a high power diode laser that produces radiation at wavelengths of 800 ± 10 nm and 940 ± 10 nm. These wavelengths are comparable to the fibre laser used in this study and therefore the absorptivity on iron-based material is assumed to be similar (Ready, 1997).

3.7 The Ac_1 and Ac_3 depths

The Gaussian laser beam produced an arc-shaped HAZ boundary below the material's surface. At the centre of the irradiated track, the maximum Ac_1 and Ac_3 depths were obtained. The Ac_1 and Ac_3 boundaries were determined by microscopic observation. The results are illustrated in Figure 13.

Let $Y_{u=\max} = 0$ in equation (23) and equation (24), and the Ac_1 and Ac_3 depths can thus be acquired. The calculated values are compared with measured results in Figure 14. For samples 1 and 6, the measured Ac_1 and Ac_3 depths are about 36% to 40% of the calculated values. For samples 2, 3 and 4, the percentage is 27% to 30%. For sample 5, this ratio is 15% to 20%, showing that this model may be less reliable for soft annealed steel with high chromium and silicon contents. Despite the system error and assumed prerequisites that might not accord very well with the practical test conditions, the error might be partially caused by the absorptivity of fibre laser in this study. Presumed on the basis of high power diode laser hardening, the absorptivity of the fibre laser irradiation on steel was possibly overestimated.

Figure 13 The Ac_1 and Ac_3 depths of the tested samples (see online version for colours)

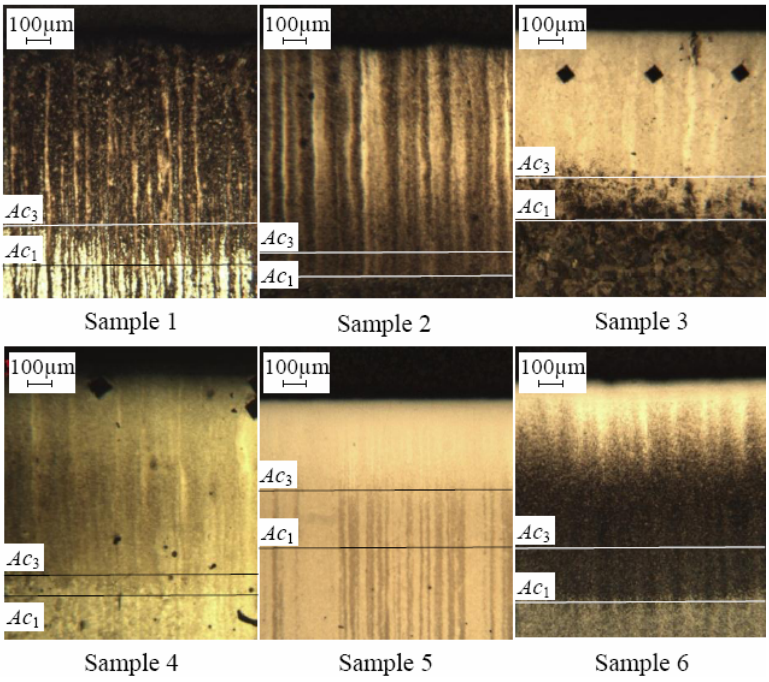

Figure 14 Comparison of calculated Ac_1 and Ac_3 depths with measured results (see online version for colours)

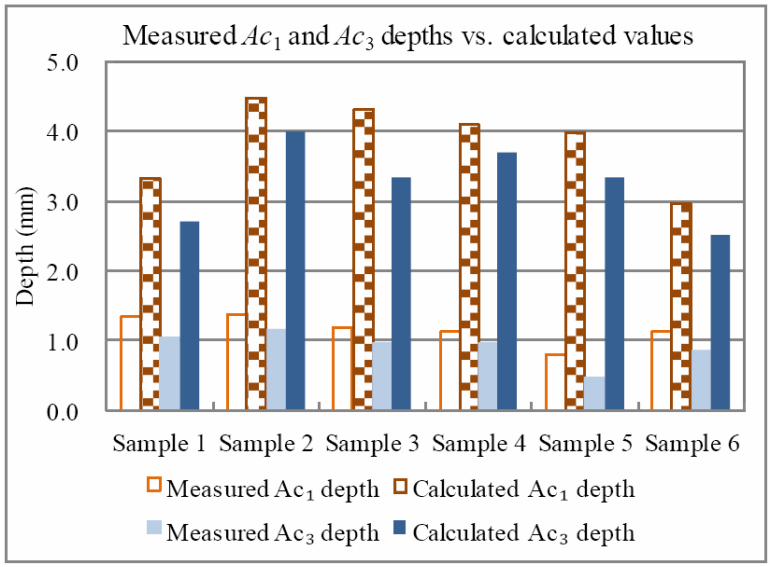

The coefficient of correction is determined and applied to this model. The corrected Ac_1 and Ac_3 depths is expressed as:

$$D_{Ac} = \eta r_b Z_{Ac} \tag{33}$$

where

Z_{Ac} is calculated dimensionless Ac_1 or Ac_3 depth with equation (23) or equation (24),

D_{Ac} is corrected Ac_1 or Ac_3 depth corresponding to Z_{Ac}

η is the coefficient of correction. $\eta = 0.27 \sim 0.4$ for samples 1, 2, 3, 4 and 6. $\eta = 0.15 \sim 2.0$ for sample 5.

3.8 The temperature cycle (T cycle)

Substituting equation (20) into equation (13) with $Y = Z = 0$ gives:

$$T_i = \frac{P_0}{4\rho C_p \pi \alpha r_b} \int_0^{+\infty} \frac{\varepsilon}{(\varepsilon^2+1)H} \cdot \exp\left(-\frac{2\left(X_{t=0} - \frac{\alpha}{r_b^2} Vt + V\varepsilon^2/8 \right)}{\varepsilon^2+1} \right) \times \left\{ 1 + 2\sum_{n=1}^{\infty} \exp\left(-\frac{n^2\pi^2\varepsilon^2}{8H^2} \right) \right\} d\varepsilon \tag{34}$$

$X_{t=0}$ is manually set to allow the calculated curve to intersect with the measured curve on t-axis. The T_i-t profile is calculated by equation (34) and compared with the measured T cycles in Figure 15.

Figure 15 Calculated, measured and corrected T cycles, (a) $v_x = 32$ mm/s (b) $v_x = 34$ mm/s (c) $v_x = 36$ mm/s (d) $v_x = 38$ mm/s (e) $v_x = 40$ mm/s (f) $v_x = 42$ mm/s (see online version for colours)

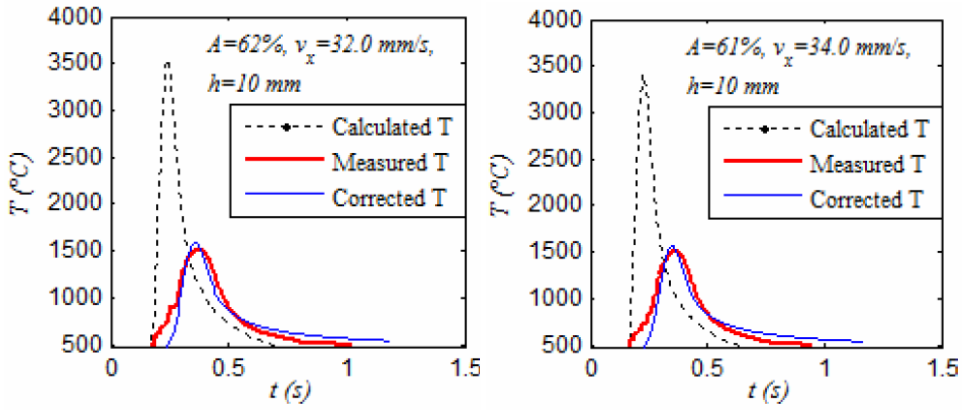

(a) (b)

Figure 15 Calculated, measured and corrected T cycles, (a) v_x = 32 mm/s (b) v_x = 34 mm/s (c) v_x = 36 mm/s (d) v_x = 38 mm/s (e) v_x = 40 mm/s (f) v_x = 42 mm/s (continued) (see online version for colours)

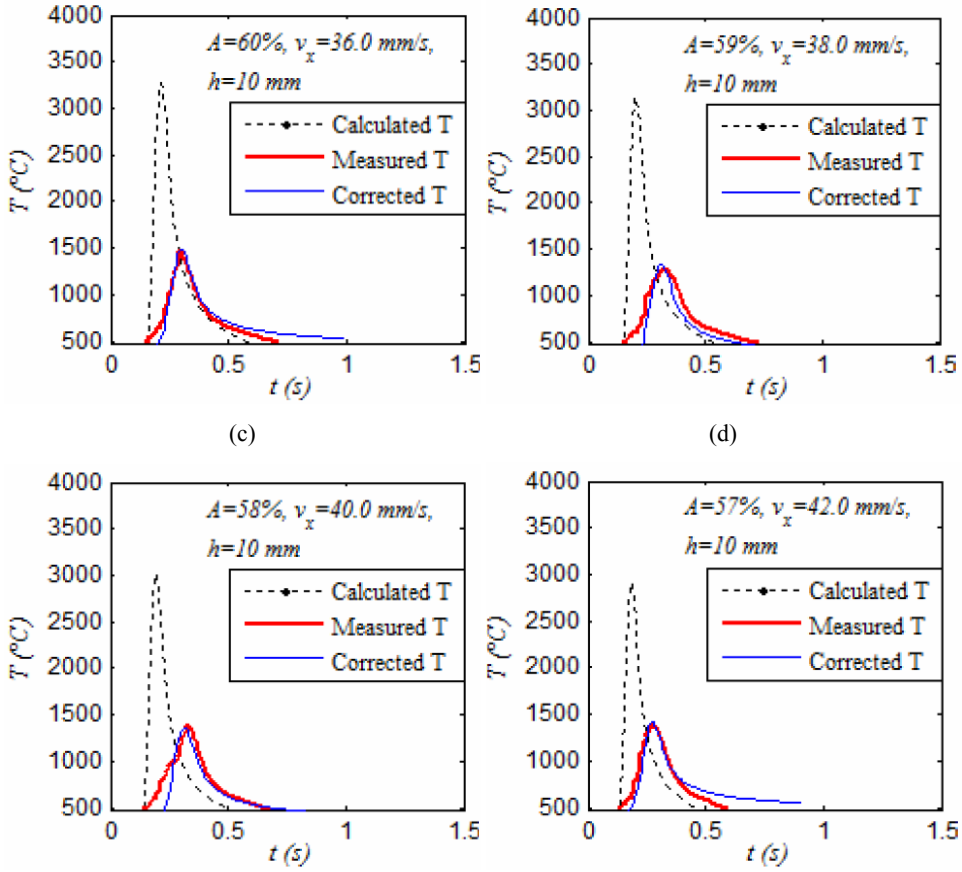

As Figure 15 shows, the measured peak temperature is around 0.286 times of the calculated value. Corrected T cycles above 488.4°C are obtained by curve fitting, which applies several correction coefficients to equation (34). The corrected formula is given as equation (35).

$$T = T_0 + j_T + \frac{j_c P_0}{4\rho C_p \pi \alpha r_b} \int_0^{+\infty} \frac{\varepsilon}{(\varepsilon^2+1)H} \cdot \exp\left(-\frac{2\left(X_{t=0} - j_u \frac{\alpha}{r_b^2} Vt + V\varepsilon^2/8 \right)^2}{\varepsilon^2+1} \right) \times \left\{ 1 + 2\sum_{n=1}^{\infty} \exp\left(-\frac{n^2\pi^2\varepsilon^2}{8H^2} \right) \right\} d\varepsilon \quad (35)$$

where

j_u, j_c, j_T are correction coefficients and are constant for AISI 4340 steel. $j_c = 286.0$, $j_u = 649.0, j_T = 340$°C. $T_0 = 20$°C.

The margin of error is determined as:

$$T_{\max|corr.} = T_{\max|me.}{}^{+72}_{-4} \text{ (°C)} \tag{36}$$

$$-\frac{dT_i}{dt}_{\max|corr.} = -\frac{dT_i}{dt}_{\max|me.} \pm 65 \text{ (°C/s)} \tag{37}$$

where

$T_{\max|corr.}$ is the corrected peak temperature

$T_{\max|me.}$ is the measured peak temperature

$-\frac{dT_i}{dt}_{\max|corr.}$ is the corrected maximum cooling rate

$-\frac{dT_i}{dt}_{\max|me.}$ is the measured maximum cooling rate.

4 Conclusions

A quasi-steady thermodynamic model is developed to describe the surface heating of a wide thin plate irradiated with a Gaussian laser beam. It provides a method to reveal the temperature distribution, the HAZ, the homogenisation time and the cooling rate of the workpiece. Equations are derived to calculate these parameters. The temperature distribution for different thickness is compared with infinite thickness at different laser traverse speed. With increased speed, the influence of sample's thickness on the surface temperature is reduced. At higher laser traverse speed, the lag of the peak temperature relative to the centre of the laser beam is increased but has a constant upper limit. Higher cooling rate is achieved at thicker samples, but the difference is reduced at larger laser traverse speed. The conditions to produce full and partial martensite are concluded.

The model is verified by experiments via comparing the calculated Ac_1 and Ac_3 depths and temperature cycles with measured data. The calculated Ac_1 and Ac_3 depths are 2.5 to 5 times higher than the measured values. The calculated peak temperatures are around 3.5 times of the measured values. This discrepancy is believed to be mainly due to the absorptivity of laser energy, which probably is overestimated. Besides, the measured time to reach the peak temperature is longer than the calculated value. This is probably due to the values of k (Table 5) which are regarded as constants in calculation. In alloys, thermal conductivity actually increases with temperature. This may be an important reason for the discrepancy. Corrected coefficients are determined to produce an empirical formula for AISI 4340 steel in this study.

References

Babu, P.D., Balasubramanian, K.R. and Buvanashekaran, G. (2011) 'Laser surface hardening: a review', *International Journal of Surface Science and Engineering*, Vol. 5, Nos. 2–3, pp.131–151.

Beck, J.V., Cole, K.D., Haji-Sheikh, A. and Litkouhi, B. (1992) *Heat Conduction Using Green's Functions*, Hemisphere, Washington, DC.

Borgnakke, C. and Sonnta, R.E. (2008) *Fundamentals of Thermodynamics*, 7th ed., Wiley, Michigan.

Carslaw, H.S. and Jaeger, J.C. (1959) *Conduction of Heat in Solids*, 2nd ed., Oxford University Press, Oxford.

Cherezova, T.Y., Chesnokov, S.S., Kaptsov, L.N. and Kudryashov, A.V. (1998) 'Super-Gaussian laser intensity output formation by means of adaptive optics', *Optics Communications*, Vol. 155, Nos. 1–3, pp.99–106.

Cline, H.E. and Anthony, T.R. (1977) 'Heat treating and melting material with a scanning laser or electron beam', *J. Appl. Phys*., Vol. 48, No. 9, pp.3895–3900.

Haberman, R. (2003) *Applied Partial Differential Equations, with Fourier Series and Boundary Value Problems*, 4th ed., Prentice Hall, Upper Saddle River.

Kim, J., Lee, M., Lee, S. and Kang, W. (2009) 'Laser transformation hardening on rod-shaped carbon steel by Gaussian beam', *Transactions of Nonferrous Metals Society of China* (English edition), Vol. 19, No. 4, pp.941–945.

Kogelnik, H. and Li, T. (1966) 'Laser beams and resonators', *Applied Optics*, Vol. 5, No. 10, pp.1550–1567.

Liu, Z., Viejo, F., Coy, A., Rahkes, M. and Aburas, Z. (2010) 'Laser surface modification for corrosion protection', Paper presented at *4th Pacific International Conference on Applications of Lasers and Optics (PICALO 2010)*, 23–25 March, Wuhan, China.

Lolov, N. (1987) *Temperature Field with Distributed Moving Heat Source*, Study Group 212, Doc. 212-682-87, International Institute of Welding.

Ma, X.H. (2004) 'A new mechanism for condensation heat transfer enhancement: effect of the surface free energy difference of condensate and solid surface', *Journal of Enhanced Heat Transfer*, Vol. 11, No. 4, pp.257–265.

Manca, O., Morrone, B. and Naso, V. (1995) 'Quasi-steady-state three-dimensional temperature distribution induced by a moving circular Gaussian heat source in a finite depth solid', *International Journal of Heat and Mass Transfer*, Vol. 38, No. 7, pp.1305–1315.

Pantsar, H. and Kujanpää, V. (2004) 'Diode laser beam absorption in laser transformation hardening of low alloy steel', *Journal of Laser Applications*, Vol. 16, No. 3, pp.147–153.

Porter, D.A., Easterling, K.E. and Sherif, M. (2009) *Phase Transformations in Metals and Alloys*, 3rd ed., CRC Press, London.

Ready, J.F. (1997) *Industrial Application of Lasers*, 2nd ed., Academic Press, London.

Rozniakowska, M. and Yevtushenko, A.A. (2005) 'Influence of laser pulse shape both on temperature profile and hardened layer depth', *Heat and Mass Transfer/ Waerme- und Stoffuebertragung*, Vol. 42, No. 1, pp.64–70.

Soskind, Y.G. (2009) 'Diode laser beam shaping and propagation characteristics', Paper presented at *Proceedings of The International Society for Optical Engineering (SPIE)*, 26–28 January, San Jose, USA.

Steen, W.M. (2003) *Laser Material Processing*, 3rd ed., Springer-Verlag, London.

Tanasawa, I. and Lior, N. (Eds.) (1992) *Heat and Mass Transfer in Materials Processing*, Hemisphere, Washington, DC.

Thelning, K-E. (1984) *Steel and its Heat Treatment*, 2nd ed., Butterworth-Heinemann, London.

Wegst, C.W. (2007) *The Key to Steel (Stahschlussel)*, 21st ed., French & European Pubns., New York.

PUBLICATION 4

Qiu, F. and Kujanpää, V. (2012)

SURFACE HARDENING OF AISI 4340 STEEL BY LASER LINEAR OSCILLATION SCANNING

The paper has been published in
Surface Engineering, **28** (8), 569-575
DOI: 10.1179/1743294412Y.0000000034

Surface hardening of AISI 4340 steel by laser linear oscillation scanning

F. Qiu*[1] and V. Kujanpää[2]

This study investigated the surface hardening of AISI 4340 steel by linear oscillation scanning with a fibre laser. Various frequencies and amplitudes of oscillation were used under laser power of 2020 and 3020 W. Microscopic evaluation was done, and the effect of oscillation frequency on the hardened depth was examined. Hardness profiles were measured along the centre of the irradiated track toward the feeding direction of the laser, across the irradiated width and into the depth below the irradiated surface. The homogeneity of hardness and hardened depth with different processing parameters was investigated. The hardness profiles were compared with the results obtained with conventional single track hardening.

Keywords: Surface treatment, Hardening, 4340 steel, Oscillation scanning, Multitrack, Fibre laser

Introduction

Laser surface transformation hardening is a process of producing hard, wear resistant regions on the workpiece while retaining the base material unaffected,[1–3] which typically uses a defocused laser beam with the laser energy density in an order of magnitude of 10^3–10^4 W cm^{-2}.[1,4] A focusing lens can be simply used to produce an out of focus laser beam profile, while the width of the irradiated track is limited by the laser spot size, and the laser energy distribution is mostly inhomogeneous. Multitrack hardening has been investigated for the purpose of large area treatment, but the decrease in hardness in the overlapping zone due to tempering remains to be a problem.[5,6] Various types of special shaping optics have been developed as an advanced solution to produce a desirable shape (e.g. rectangle) and size of the laser spot with relatively homogeneous energy distribution.[7–9] However, such optics are relatively expensive, and their flexibility in use is considered to be limited.

Laser linear oscillation scanning (LLOS) provides an alternative method for generating laser irradiated track with customisable width, as described in Fig. 1. A raw laser beam is converted by the oscillation scanner to a linearly oscillating beam that scans the sample's surface back and forth in the direction of the y axis. As the oscillating laser beam moves along the x axis, a laser irradiated track in a zigzag pattern is produced on the workpiece. This process is, in nature, a continuous multitrack surface irradiation in which the treated region consists of a number of overlapped laser irradiated tracks. Such studies as LLOS are thought to have good potential for practice, yet such studies have been rarely available so far.

In recent years, diode pumped fibre laser systems have been developed and proved to be applicable in the surface treatment of steel.[10–13] Owing to the simplicity and integratability of fibre laser, an oscillation scanning head can be installed easily with an external controller unit connected.[14]

Experimental

Material and methods

The tested material was AISI 4340 steel, which was a quenched and tempered low alloy steel composed of tempered martensite structures.[15] The composition of the material is 0·347C–0·331Si–0·007V–1·397Cr–0·697Mn–1·355Ni–0·169Mo (wt-%). The initial hardness of the base material was 329 HV. The surface roughness of the samples, R_a, was 2·5 μm.

This study used a work cell consisting of a CNC XY work table, a YLR-5000-S multimode fibre laser system and an ILV DC scanner installed as the laser head. The fibre laser produced a laser beam with a wavelength of 1070–1080 nm and a maximum nominal output power of 5 kW. An output fibre core with the diameter of 200 μm was used. The DC scanner, which was primarily designed for laser welding applications, contained a parabolic scanner mirror with focal length of 250 mm and a controller unit connected to it. The distance off the focus was 60 mm, producing a laser spot of 2·1 mm in diameter. The oscillation speed was affected by the oscillation frequency and followed the sine waveform. The parameters are given as tests A1–A6 in Table 1. For comparison, a conventional single track scanning test was done, shown as tests B1 and B2 in Table 1. To produce laser power densities of 15136 and 22629 W cm^{-2}, 2020 and 3020 W laser power with 75 mm off focus distance were used respectively. The feeding speed was constantly 15 mm s^{-1} in the whole test.

Modulation of laser power profile

Figure 2*a* shows the laser energy distribution with oscillation frequency of 100 Hz and amplitude of 6·2

[1]Laser Processing Laboratory, LUT Metal, Lappeenranta University of Technology, Tuotantokatu 2, 53850 Lappeenranta, Finland
[2]VTT Technical Research Centre of Finland, Tuotantokatu 2, 53850 Lappeenranta, Finland

*Corresponding author, email feng.qiu@lut.fi

Published by Maney on behalf of the Institute
Received 24 May 2012; accepted 9 June 2012
DOI 10.1179/1743294412Y.0000000034

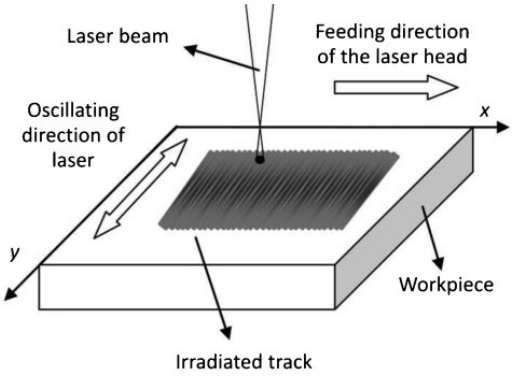

1 Scheme of LLOS process

mm produced by the DC scanner. Since the oscillation speed was reduced to 0 at the edge of oscillation, in order to avoid melting, the output laser power was modulated by programming via the controller unit. As shown in Fig. 3, the output laser power was programmed at 19 positions with equal spacing across the irradiated width, producing an approximated sine wave laser power profile with peak laser power of 2020 and 3020 W respectively and with 300 W laser power at both edges of oscillation. Since the oscillation speed followed the sine waveform as mentioned above, the ratio of oscillation speed to output laser power could be regarded as constant. Figure 2*b* shows a controlled laser beam profile featuring reduced laser power density near the edge of oscillation. The average laser power densities measured were 14 483 and 21 691 W cm^{-2} under 2020 and 3020 W laser power respectively, which were close to those produced by the single track scanning mentioned above.

Calculations

Scanning speed

The scanning speed is the combination of the oscillation speed and the feeding speed of the laser. Since the oscillation speed (v_y) is in sine waveform, it can be written as

$$v_y = 2\pi\mu A \sin\left(\frac{\pi y}{2A}\right) \tag{1}$$

where y is the position of the laser spot. At $y = 0$ and $y = 2A$, the laser spot is at the edges of oscillation.

Moreover

$$v_{y\,\max} = 2\pi\mu A \tag{2}$$

where v_{ymax} is the maximum oscillation speed, which is achieved at the middle of the oscillation.

The scanning speed (v) is therefore

$$v = \left(v_y^2 + v_x^2\right)^{1/2} = \left[4\pi^2\mu^2A^2\sin^2(2\pi\mu t) + v_x^2\right]^{1/2} \tag{3}$$

where v_x is the feeding speed of the laser head. In this study, v_x=15 mm s^{-1}.

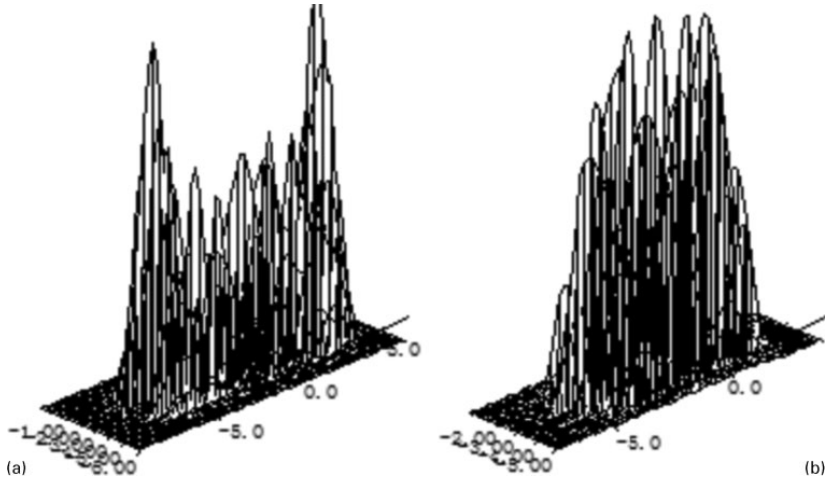

2 Laser energy distribution produced by DC scanner with oscillation frequency of 100 Hz and amplitude of 5·9 mm: *a* without power control; *b* with power control via controller unit

Table 1 Processing parameters

Test	Laser power *P*/W	Oscillation frequency μ/Hz	Amplitude *A*/mm
A1	2020	10	11·0
A2	2020	20	8·5
A3	2020	40	4·5
A4	3020	20	10·0
A5	3020	40	7·4
A6	3020	100	5·9
B1	2020	NA	NA
B2	3020	NA	NA

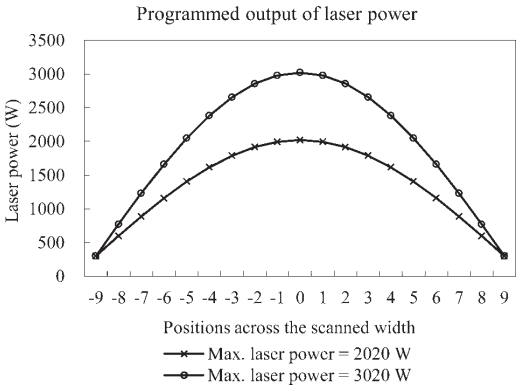

3 Programmed laser power output via controller unit of DC scanner

The average oscillation speed ($\overline{v_y}$) is

$$\overline{v}_y = 4A\mu \tag{4}$$

v_{ymax} and $\overline{v}_y$ are calculated for the parameters of oscillation test in Table 1 using equations (2) and (4). The oscillation speed of the test is described in Fig. 4, obtained on the basis of equation (1). It can be markedly seen that $\overline{v}_y$ is dramatically higher than v_x (15 mm s^{-1}) in this study, and thus, v can be treated as $v=v_y$ in equation (3), although at the edges of oscillation $v_y=0$ and $v=v_x$.

Overlap width of adjacent tracks

Figure 5 schematically describes the overlapped neighboring tracks of LLOS. The laser spot starts from position O_1 and reaches O_2 in one period of oscillation. At the edge of oscillation, the laser spot moves along the feeding direction with a distance, which can be calculated as

$$S_{e0} = \frac{v_x}{\mu} \tag{5}$$

where S_{e0} is the distance at the edge of oscillation between the laser spots of adjacent tracks.

Thus, the overlap width at the edge of oscillation S_{eov} can be expressed as

$$S_{eov} = d_0 - S_{e0} \tag{6}$$

where d_0 is the diameter of the laser spot.

Substituting equation (5) with equation (6) gives

$$S_{eov} = d_0 - \frac{v_x}{\mu} \tag{7}$$

At the centre of the oscillation, the overlap width S_{cov} can be calculated as

$$S_{cov} = d_0 - \frac{S_{e0}}{2} = d_0 - \frac{v_x}{2\mu} \tag{8}$$

Number of scans spot experiences in centre of oscillation

During the oscillation scanning process, a position in the middle of the oscillation width may experience multiple times of laser irradiation. According to Fig. 5, the number of scans N_c is the integral part of the ratio of d_0/S_{e0}, which can be expressed as

$$N_c = 2\left(\frac{2d_0}{S_{e0}}\right) \tag{9}$$

Substituting equation (5) with equation (9) gives

$$N_c = 2\left(\frac{2d_0\mu}{v_x}\right) \tag{10}$$

Based on the test parameters in Table 1, equations (5), (8) and (10), S_{e0}, S_{cov} and N_c can be calculated. The results are shown in Table 2.

Hardness measurement

The hardness measurement was done on a Vickers hardness tester with a load of 100 g. Three series of positions in the tested samples were measured (Fig. 6). Series 1 was along the centre of the irradiated area toward the feeding direction. The starting point was randomly selected. Series 2 was across the whole irradiated width of the cross-section. Series 3 was along the depth below the centre of the irradiated track. Measurements of series 1 and 2 were done at 0·05 mm depth below the surface, which was assumed to have nearly identical hardness to the surface. In this study,

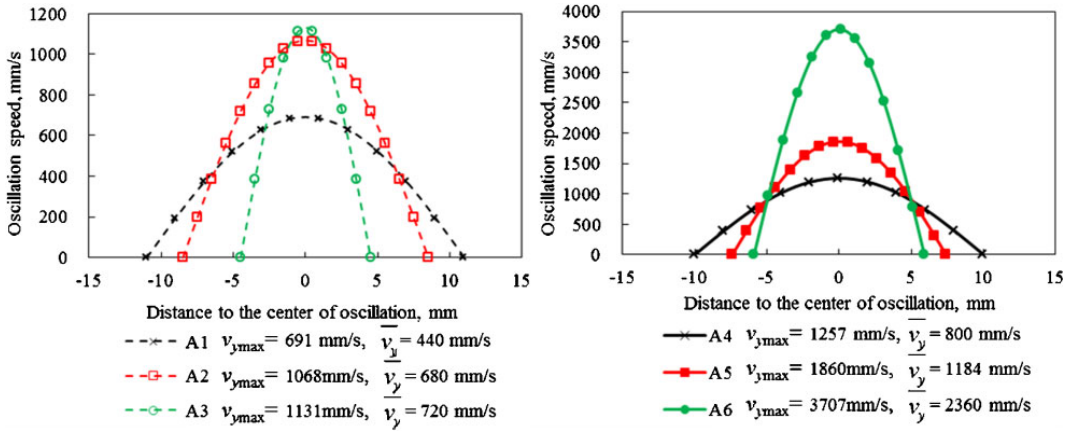

4 Oscillation speed of test

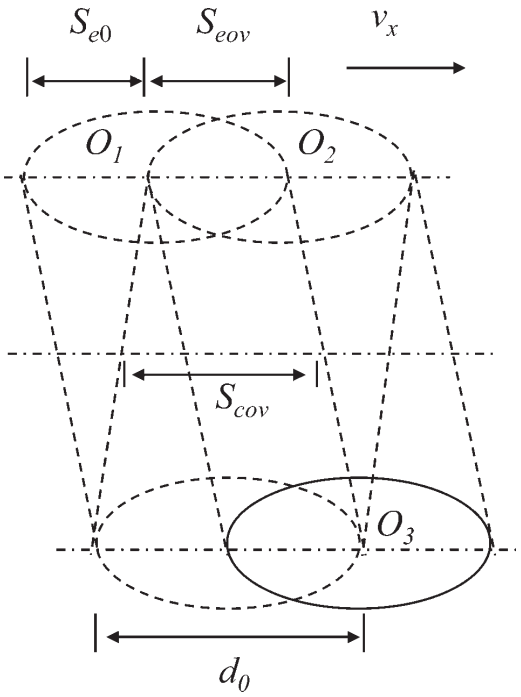

5 Schematic diagram of overlapped adjacent tracks in LLOS

the hardened depth is defined as the depth where the measured hardness decreases to below 400 HV.

Results and discussion

Figures 7–9 show the hardness profiles measured along the centre of the irradiated track, across the irradiated width and into the depth below the surface. Results obtained with various frequencies and amplitudes of oscillation are shown under 2020 and 3020 W laser power respectively. Hardness profiles acquired with single track scanning are included as well for comparison.

Hardness profile along centre of irradiated track

As shown in Fig. 7*a*, tests A1 and A3 produced surface hardness values of 460–703 and 652–831 HV respectively, which were relatively inhomogeneous. Test A2 did not cause hardening of the material. Test B1 resulted in relatively homogeneous surface hardness of ~684 HV, which was close to the average hardness of 717 HV caused by test A3. Figure 7*b* shows that test A4 caused little hardening effect, while individual scans might be distinguished by the variation of hardness. The marked hardness variation caused by A1 and A4 can be explained

Table 2 Calculated S_{cov} and N_c of test

Test	S_{e0}/mm	S_{cov}/mm	N_c
A1	0·75	1·35	4
A2	0·37	1·73	10
A3	0·19	1·91	22
A4	0·37	1·73	10
A5	0·19	1·91	22
A6	0·07	2·03	56

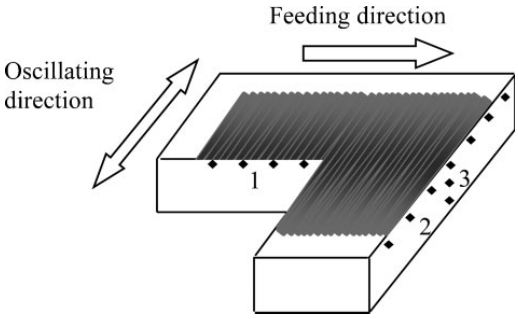

6 Hardness measurement positions of samples

by the tempering effect.[16] According to Table 2, the distances between adjacent tracks of A1 and A4 at the edge of oscillation were 0·75 and 0·37 mm respectively, which were much larger than A6 (0·07 mm). Test A6 with oscillation frequency of 100 Hz produced an overlap width of 2·03 mm, which was 96·7% of the whole laser spot diameter (2·1 mm). This might have resulted in massive tempering covering almost the whole irradiated area and thus resulted in homogeneous surface hardness. Tests A5 and A6 caused respective average hardness of 795 and 777 HV, which were similar to the hardness of 767 HV produced by test B2. As markedly noticed, the hardness variation by test A6 was much smaller than that by test A5, which was caused by the higher scanning frequency of A6 (100 Hz), compared to A5 (40 Hz).

Hardness profile across irradiated width

Figure 8 indicates hardness across the width of the irradiated track. Noticeably, in the results of tests A1, A3, A5 and A6, the highest hardness was not achieved in the centre of the track but millimeters away from it. The maximum hardness values obtained were 764, 790, 909 and 892 HV for tests A1, A3, A5 and A6 respectively. For tests A3, A5 and A6, the maximum hardness was achieved at ~2·5, 4 and 2 mm respectively, considerably higher than the average of the measured hardness along the centre of the track (Fig. 7). According to Fig. 5, this was possibly caused by the tempering effect, which was stronger in the centre of oscillation than elsewhere. According to equation (2), reducing the oscillation frequency and/or the amplitude can decrease the maximum oscillation speed. Compared with test B1 with 2020 W laser power, tests A1 and A3 produced similar hardness in the centre of the track, as shown in Fig. 8*a*. However, test A1 generated a much larger irradiated width, and test A3 markedly produced higher average hardness across the track. Similarly, as denoted in Fig. 8*b*, tests A5 and A6 both produced wider hardened tracks with higher average hardness than test B2. Figure 8*a* shows that test A2 did not cause hardening at all but retained the hardness values of the base material. Figure 8*b* denotes that test A4 caused very slight hardening, indicating that a small amount of martensite might have formed on the surface.

Hardness profile along depth below irradiated track

Figure 9 compares the hardness profiles along the depth beneath the irradiated track. As seen in Fig. 9*a*, test A2 did not cause hardening. Tests A1 and A4 produced very

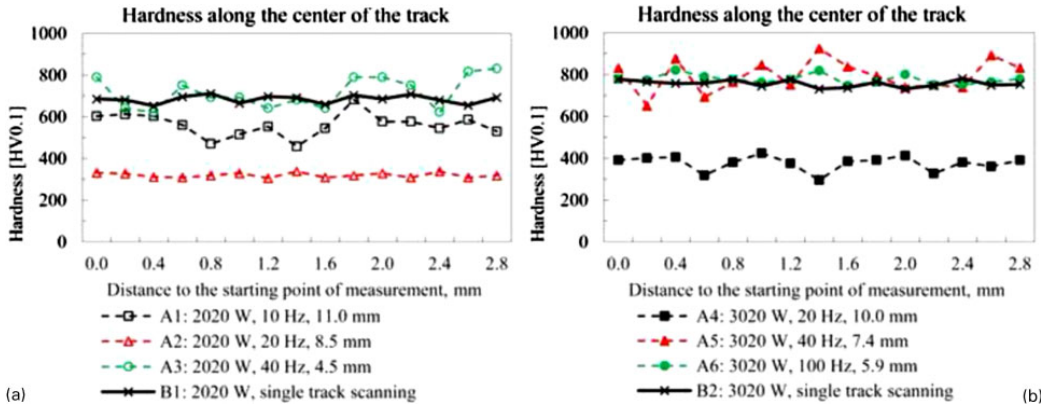

7 Hardness profile along centre of irradiated track with laser power of *a* 2020 W and *b* 3020 W

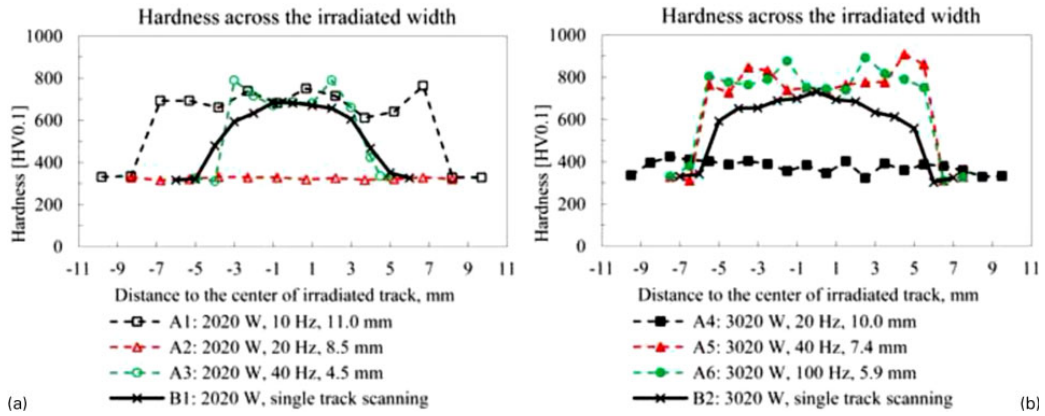

8 Hardness profile across irradiated track with laser power of *a* 2020 W and *b* 3020 W

small hardened depth of <~0·1 mm. As compared in Fig. 9*a*, tests A3 and B1 produced hardened depth of ~0·55 and 0·9 mm respectively. However, between the surface and 0·5 mm depth, test A3 generated fairly consistent hardness of 682–751 HV, markedly higher than single track scanning test B1 that caused 524–683 HV. Similar phenomena were noticed in Fig. 9*b*. Regarding the hardness from the surface to 0·4 mm deep, tests A5 and A6 generated 641–803 and 693–831 HV respectively, which were higher than the hardness of 593–753 HV acquired by test B2. Tests A5 and A6 produced hardened depth of 0·4 and 0·5 mm respectively, which were much smaller than the 1·5 mm hardened layer by test B2. This is believed to

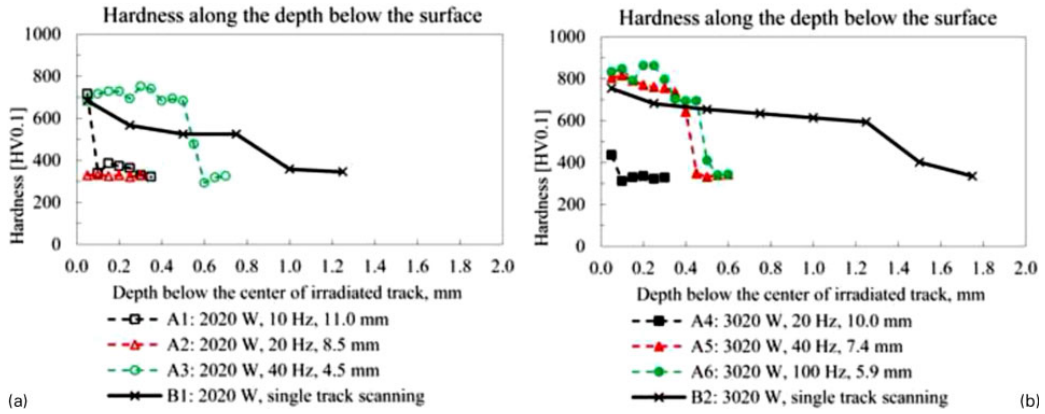

9 Hardness profile along depth below irradiated track with laser power of *a* 2020 W and *b* 3020 W

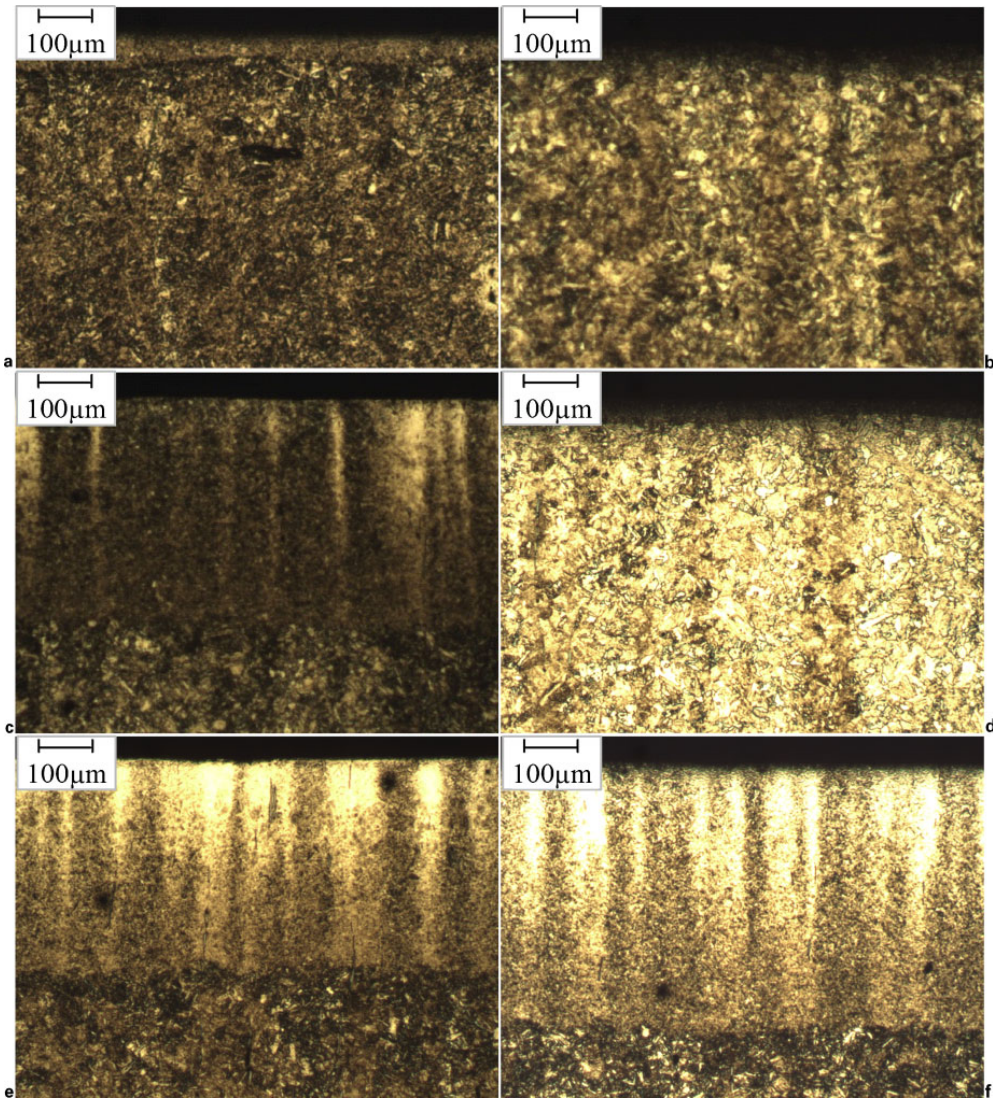

10 Microscopic view below centre of irradiated surface of samples tested with different laser power, frequency and amplitude of oscillation respectively: samples were etched with 5% nital: *a* A1: 2020 W, 10 Hz, 11·0 mm; *b*A2: 2020 W, 20 Hz, 8·5 mm; *c* A3: 2020 W, 40 Hz, 4·5 mm; *d* A4: 3020 W, 20 Hz, 10·0 mm; *e* A5: 3020 W, 40 Hz, 7·4 mm; *f* A6: 3020 W, 100 Hz, 5·9 mm

be due to the high scanning speed in the middle of oscillation, which did not allow sufficient heating in a large depth of the material.

Microscopic evaluation

Microscopic observation on the microstructure of the tested samples provided a direct and qualitative way to visually evaluate the experimental effect. Samples tested with different laser power, frequency and amplitude of oscillation are compared in Fig. 10, which shows the microscopic view below the centre of the irradiated area toward the feeding direction of the laser beam.

As measured in Fig. 10, the depths of the heat affected zone (HAZ) produced by tests A1–A6 were respectively ~0·05, 0, 0·45, 0·05, 3·8 and 4·5 mm, which were well in accordance to the hardened depth indicated in Fig. 9. Figure 10*c*, *e* and *f* shows that HAZ acquired with 40 and 100 Hz were much deeper. No HAZ was observed in Fig. 10*b*, meaning that phase transformation did not occur on the sample. According to equation (2), the oscillation speed produced with 20 Hz and 8·5 mm amplitude might be too high to allow sufficient absorption of laser energy. Tests A2 and A3 were done with both 2020 W laser power and, according to equation (2), with very close oscillation speed. However, the depths of HAZ were dramatically different by comparing Fig. 10*b* and *c*. A possible explanation is that with higher oscillation frequency, the scanned surface experienced more cycles of

irradiation, which meant more absorption of laser power. Figure 10*a* and *d* with 10 and 20 Hz respectively shows very small and inhomogeneous HAZ depths, which might be caused by the distinguishable adjacent tracks. Differently, the individual scans could not be distinguished with 40 and 100 Hz in Fig. 10*c*, *e* and *f*. As shown in Table 2, this can be explained by the large overlap width and large number of overlapped scans under the frequencies of 40 and 100 Hz.

Conclusion

The LLOS test was done on AISI 4340 steel with different frequencies and amplitudes of oscillation. The results were investigated and compared with single track hardening process. A local position in the centre of oscillation might receive up to tens of times of scanning, depending on the laser spot size, oscillation frequency and feeding speed of the laser head. The hardened depth could be increased by applying higher oscillation frequency of scanning. Under the feeding speed of 15 mm s^{-1}, individual scans could be distinguished with 10 and 20 Hz. Along the centre of the irradiated track, the hardness profile with oscillation frequency of 100 Hz was more homogeneous than with 10, 20 and 40 Hz and was close to single track scanning. With LLOS, the maximum hardness might be acquired at millimeters away from the centre of the track. A higher overall hardness on the laser irradiated surface was produced with LLS than with single track hardening, and LLOS with the oscillation frequencies of 40 and 100 Hz caused higher hardness in the hardened layer. Furthermore, LLOS was proved to be suitable for surface hardening in a relatively large rectangular area with considerable depth of hardening. Within the hardened depth of 0·6 mm, LLOS at 40 and 100 Hz produced higher hardness than single track hardening. However, the maximum achievable hardened depth produced by LLOS was notably limited in comparison to conventional single track scanning.

Acknowledgement

The authors are very much grateful to Mr A. Anonen of Ovako Oy who kindly provided the tested materials, Mr I. Poutiainen and Mr P. Kokko of LUT who arranged the experiment and Mr E. Lappalainen of LUT who gave instruction on making the measurements. Without their support, this study would not have been completed.

References

1. J. C. Ion: *Surf. Eng.*, 2002, **18**, 14–31.
2. A. Pinkerton: *Surf. Eng.*, 2009, **25**, 177–179.
3. W. M. Steen and J. Mazumder: 'Laser material processing', 4th edn, 576; 2010, London, Springer-Verlag.
4. J. Grum: in 'Steel heat treatment: equipment and process design', (ed. G. E. Totten), 2nd edn, Ch. 6, 437–438; 2006, Boca Raton, FL, CRC Press.
5. C. W. Yao, J. Huang, P. L. Zhang, Y. X. Wu and B. S. Xu: *Trans. Mater. Heat Treat.*, 2009, **30**, 131–135.
6. G. Campana, A. Ascari and G. Tani: Proc. ASME 2009 Int. Conf. on 'Manufacturing science and engineering', West Lafayette, IN, USA, October 2009, Manufacturing Engineering Division, ASME, Paper 95.
7. S. Bonss, J. Hannweber, U. Karsunke, S. Kuehn, M. Seifert and E. Beyer: Proc. SPIE on 'High power laser materials processing: lasers, beam delivery, diagnostics, and applications', San Francisco, CA, USA, January 2012, The Society of Photo-Optical Instrumentation Engineers (SPIE), Paper 82390I.
8. M. Baumann, V. Krause, G. Bergweiler, M. Flaischerowitz and J. Banik: Proc. SPIE on 'High power laser materials processing: lasers, beam delivery, diagnostics, and applications', San Francisco, CA, USA, January 2012, The Society of Photo-Optical Instrumentation Engineers (SPIE), Paper 82390J.
9. A. Laskin and V. Laskin: Proc. SPIE on 'Laser resonators and beam control XIII', San Francisco, CA, USA, January 2012, The Society of Photo-Optical Instrumentation Engineers (SPIE), Paper 79130J.
10. P. P. Shukla and J. Lawrence: *Surf. Eng.*, 2011, **27**, 742–748.
11. M. S. F. de Lima, F. A. Gioia, R. Riva and A. M. E. Santo: *Mater. Res.*, 2007, **10**, 461–467.
12. F. A. Gioia and M. S. F. de Lima: *J. ASTM Int.*, 2011, **8**, 488–496.
13. F. Qiu and V. Kujanpää: *Mechanika*, 2011, **17**, 318–323.
14. J. Canning: *Opt. Lasers Eng.*, 2006, **44**, 647–676.
15. C. W. Wegst: 'The key to steel (Stahschlussel)', 22nd edn, 720; 2010, Marbach, Verlag Stahlschlüssel.
16. H. J. Hegge, H. De Beurs, J. Noordhuis and J. Th. M. De Hosson: *Metall. Mater. Trans. A*, 1990, **21A**, 987–995.

ACTA UNIVERSITATIS LAPPEENRANTAENSIS

465. VASAVA, PARITOSH. Application of computational fluid dynamics in modelling blood flow in human thoracic aorta. 2011. Diss.

466. PURO, LIISA. Identification of extractives and polysaccharides as foulants in membrane filtration of pulp and paper mill effluents. 2011. Diss.

467. LAPPALAINEN, PIA. Socially Competent Leadership – predictors, impacts and skilling in engineering. 2012. Diss.

468. PLAMTHOTTATHIL, ANSHY OONNITTAN. Application of electrokinetic Fenton process for the remediation of soil contaminated with HCB. 2012. Diss.

469. EBRAHIMI, FATEMEH. Synthesis of percarboxylic acids in microreactor. 2012. Diss.

470. JANTUNEN, SAMI. Making sense of software product requirements. 2012. Diss.

471. VILKO, JYRI. Approaches to supply chain risk management: identification, analysis and control. 2012. Diss.

472. TANSKANEN, VESA. CFD modelling of direct contact condensation in suppression pools by applying condensation models of separated flow. 2012. Diss.

473. HUHTANEN MIKKO. Software for design of experiments and response modelling of cake filtration applications. 2012. Diss.

474. PARJANEN, SATU. Creating possibilities for collective creativity
Brokerage functions in practice-based innovation. 2012. Diss.

475. KUKKONEN, SAKU. Generalized differential evolution for global multi-objective optimization with constraints. 2012. Diss.

476. LAAKSONEN, JONNA. Tactile-proprioceptive robotic grasping. 2012. Diss.

477. KALLIO, ANNE. Enhancing absorptive capacity in a non-research and development context
An action research approach to converting individual observations into organizational awareness. 2012. Diss.

478. LÄTTILÄ, LAURI. Improving transportation and warehousing efficiency with simulation based decision support systems. 2012. Diss.

479. OYOMNO, WERE. Usable privacy preservation in mobile electronic personality. 2012. Diss.

480. LINNALA, MIKKO. Simulation and optimization tools in paper machine concept design. 2012. Diss.

481. KORPIJÄRVI, JUHA. Aging based maintenance and reinvestment scheduling of electric distribution network. 2012. Diss.

482. KORHONEN, JUHAMATTI. Active inverter output filtering methods. 2012. Diss.

483. KLODOWSKI, ADAM. Flexible multibody approach in bone strain estimation during physical activity: quantifying osteogenic potential. 2012. Diss.

484. VUORENMAA, MARKKU. Osaamisen johtaminen pk-yrityksen kansainvälisen kasvun elinkaarella. 2012. Diss.

485. RAUTIAINEN, MARITA. Dynamic ownership in family business systems – a portfolio business approach. 2012. Diss.

486. LILIUS, REIJO. THE FINNISH IT INDUSTRIES IN TRANSITION Defining and measuring the Finnish software product and IT services industries by applying theoretical frameworks . 2012. Diss.

487. TUOMINEN, PASI. The purpose of consumer co-operation: implications for the management and governance of co-operatives. 2012. Diss.

488. SAARI, ESA. Suurnopeus-turbokoneroottoreiden termodynaaminen ja mekaaninen mallinnus sekä rakenneanalyysi. 2012. Diss.

489. PAANANEN, MIKKO. On innovative search: the use of internal and external sources of innovation among Finnish innovators. 2012. Diss.

490. BELOVA, POLINA. Quasiclassical approach to the vortex state in iron-based superconductors. 2012. Diss.

491. HIETANEN, IIRO. Design and characterization of large area position sensitive radiation detectors. 2012. Diss.

492. PÄSSILÄ, ANNE. A reflexive model of research-based theatre Processing innovation of the cross-road of theatre, reflection and practice-based innovation activities. 2012. Diss.

493. RIIPINEN, TOMI. Modeling and control of the power conversion unit in a solid oxide fuel cell environment. 2012. Diss.

494. RANTALAINEN, TUOMAS. Simulation of structural stress history based on dynamic analysis. 2012. Diss.

495. SALMIMIES, RIINA. Acidic dissolution of iron oxides and regeneration of a ceramic filter medium. 2012. Diss.

496. VAUTERIN, JOHANNA JULIA. The demand for global student talent: Capitalizing on the value of university-industry collaboration. 2012. Diss.

497. RILLA, MARKO. Design of salient pole PM synchronous machines for a vehicle traction application. 2012. Diss.

498. FEDOROVA, ELENA. Interdependence of emerging Eastern European stock markets. 2012. Diss.

499. SHAH, SRUJAL. Analysis and validation of space averaged drag model for numerical simulations of gas-solid flows in fluidized beds. 2012. Diss.

500. WANG, YONGBO. Novel methods for error modeling and parameter identification of redundant hybrid serial-parallel robot. 2012. Diss.

501. MAXIMOV, ALEXANDER. Theoretical analysis and numerical simulation of spectral radiative properties of combustion gases in oxy/air-fired combustion systems. 2012. Diss.

502. KUTVONEN, ANTERO. Strategic external deployment of intellectual assets. 2012. Diss.

503. VÄISÄNEN, VESA. Performance and scalability of isolated DC-DC converter topologies in low voltage, high current applications. 2012. Diss.

504. IKONEN, MIKA. Power cycling lifetime estimation of IGBT power modules based on chip temperature modeling. 2012. Diss.

505. LEIVO, TIMO. Pricing anomalies in the Finnish stock market. 2012. Diss.

506. NISKANEN, ANTTI. Landfill gas management as engineered landfills – Estimation and mitigation of environmental aspects. 2012. Diss.